

Atomic-Scale Numerical Simulations of Radiation-Induced Damage in Semiconductors

PARIZE Julien

**Thesis Supervisors: HEMERYCK Anne, RICHARD Nicolas & JARRIN
Thomas**

**GEETS
Université de Toulouse**

Contents

1	Radiation Impacts on Electronic Devices	10
1.1	Introduction	12
1.2	Understanding Radiation: Environments and Effects	12
1.2.1	Radiations	12
1.2.2	Radiation environments	13
1.2.2.1	Artificial environments	13
1.2.2.2	Terrestrial environments	14
1.2.2.3	Spatial environments	14
1.3	Particle-matter interactions and basic microelectronics	18
1.3.1	Effects of radiation particle	19
1.3.1.1	Charged particles	19
1.3.1.2	Photons	19
1.3.1.3	Neutrons	20
1.3.2	Microelectronics basics	20
1.3.2.1	Metal-Oxide Semiconductor	21
1.3.2.2	Complementary Metal-Oxide Semiconductor	22
1.3.2.3	High-Electron-Mobility Transistor	23
1.3.3	Radiation effects and degradation mechanisms	25
1.3.3.1	Definitions of Key Terms	25
1.3.3.2	Dose rate	26
1.3.3.3	Single event effect	27
1.3.3.4	Ionizing dose	29
1.3.3.5	Displacement damage dose	30
1.3.3.6	Displacement damage degradation mechanisms and their impact on larger scale	31
1.4	State of the art: Gallium nitride	34
1.4.1	Gallium Nitride	34
1.4.1.1	History of gallium nitride	34
1.4.1.2	GaN radiation resistance	38
1.5	Conclusion	40
2	Simulation Methodology	47
2.1	Introduction	49
2.2	Multi-model numerical simulation approach	50

2.3	Monte-Carlo	52
2.3.1	Binary Collision Approximation	53
2.3.2	SRIM & TRIM	57
2.3.3	The case of Displacement Damage	59
2.4	Molecular Dynamics	59
2.4.1	Generalities	59
2.4.2	Integration algorithms	60
2.4.2.1	Position-Verlet	60
2.4.2.2	Velocity-Verlet	61
2.4.2.3	Thermodynamical conditions	61
2.4.3	The Case of Displacement Damage	62
2.4.3.1	Timestep	62
2.4.3.2	Interatomic potentials	63
2.4.3.3	Tersoff/ZBL potential	63
2.4.4	Available tool	67
2.4.5	Advantages and limitations	67
2.4.6	Threshold Displacement Energy	67
2.5	<i>Ab initio</i> Methods	71
2.5.1	<i>Ab initio</i> Molecular Dynamics	71
2.5.2	Density Functional Theory	71
2.5.2.1	Schrödinger equation, Born-Oppenheimer and electron density	71
2.5.2.2	Hohenberg-Kohn theorems	74
2.5.2.3	Kohn and Sham equations	75
2.5.2.4	DFT cycle	75
2.5.2.5	Approximations	77
2.5.2.6	Plane wave formalism	77
2.5.2.7	Advantages and limitations	78
2.5.2.8	Available tools	78
2.5.2.9	The case of Threshold Displacement Energy	78
2.6	Conclusion	81
3	Displacement damage in GaN and comparaison with Si and Ge	85
3.1	Introduction	86
3.2	State of the Art on Collision Cascades in GaN and Other Semiconductors	86
3.3	Preliminary Analysis and Neutron-Displacement Damage Cross Section of Gallium Nitride (GaN)	88
3.3.1	Introductory Investigations	88
3.3.2	Neutron Displacement Damage Cross Section in Gallium Nitride (GaN)	89
3.3.2.1	Lindhard–Robinson Method	90
3.3.2.2	Threshold Displacement Energy Method	90
3.3.2.3	Stopping and Range of Ions in Matter (SRIM)/Transport of Ions in Matter (TRIM) Method	91
3.3.2.4	Non-Ionising Energy Loss	91

3.3.2.5	Primary Knock-On Atom (PKA) distributions to Displacement damage (DD)	92
3.4	Collisions cascade and resulting displacement damage in GaN, Si and Ge	95
3.4.1	Computational details	95
3.4.2	Methodological Insights	97
3.4.2.1	Defect Quantification Using Wigner-Seitz Method	97
3.4.2.2	Understanding Maximum Penetration Depth	98
3.4.3	Results & Discussion	99
3.4.3.1	State of damage at the end of the simulations	99
3.4.3.2	Collision cascade dynamics and clustering	103
3.4.3.3	Morphology of Cascades and Interstitials Atom Displacements	107
3.4.3.4	Concluding Remarks	110
3.5	Conclusion	112
4	Quantifying Threshold Displacement Energy in GaN	117
4.1	Introduction	118
4.2	State of the Art	120
4.3	Simulation Parameters and Configuration	122
4.3.1	AIMD Computational details	122
4.3.2	MD Computational details	123
4.4	Exploration of TDE in GaN	124
4.4.1	Threshold Displacement Energy Values for 5 Directions in AIMD and MD at 0 K and 300 K	125
4.4.2	Defect Configuration	129
4.5	Large-Scale study of TDE in GaN	131
4.5.1	Raw TDE Data Section	131
4.5.2	Spatial Distribution of Directions Based on TDE	135
4.5.3	Temperature Effect on TDE in GaN	139
4.6	Discussion	141
4.7	Conclusion	143
	Conclusion	147
	Appendices	151

Acronyms

2DEG	two-dimensional electron gas
AIMD	<i>Ab Initio</i> Molecular Dynamics
BCA	Binary Collision Approximation
CMOS	Complementary Metal-Oxide-Semiconductor
DDD	Displacement Damage Dose
DD	Displacement damage
DFT	Density Functional Theory
FET	Field-Effect Transistor
HEMT	High-Electron-Mobility transistor
HVPE	Hybrid Vapor Phase Epitaxy
IEL	Ionizing Energy Loss
MC	Monte-Carlo
MD	Molecular Dynamics
MESFET	Metal-Semiconductor Field-Effect Transistor
MOSFET	Metal-Oxide-Semiconductor Field-Effect Transistor
MOS	Metal-Oxide-Semiconductor
NIEL	Non-Ionizing Energy Loss
PKA	Primary Knock-On Atom
SRIM	Stopping and Range of Ions in Matter
TDE	Threshold Displacement Energy
TID	Total-Ionizing Dose

TRIM Transport of Ions in Matter

AlGaN Aluminum Gallium Nitride

GaAs Gallium Arsenide

GaN Gallium Nitride

InGaN Indium Gallium Nitride

kART Kinetic Activation-Relaxation technique

SiC Silicon Carbide

Introduction

The 21st century has been marked by a series of technological advances, particularly in the field of space exploration, which has experienced a resurgence of interest since the late 2010s. The rise of private companies, with reusable launch systems and ever-growing ambitions, has democratized access to space and paved the way for numerous ambitious projects. However, space remains an extremely hostile environment for technology, particularly due to galactic cosmic rays, composed of high-energy particles, and solar flares, which release vast quantities of charged particles, posing a danger to astronauts and a constant threat to electronic systems and onboard equipment. The radiations can penetrate materials and interact with electronic components, causing parasitic currents or permanent damage to circuits. In this context, hardening microelectronic technologies, *i.e.* making them more resistant to radiation effects, has become an absolute necessity to ensure the success of space missions and the safety of equipment in this extreme environment. While various approaches to radiation hardening have been explored over the past decades, the increasing complexity of modern electronic systems and the growing demands of space exploration call for more sophisticated solutions. Previous research has primarily focused on traditional semiconductor materials such as silicon, but emerging wide-bandgap semiconductors offer promising alternatives. Among semiconductor materials, gallium nitride (GaN) has attracted significant attention in recent years due to its unique and advantageous properties. GaN is characterized by a wide bandgap, high electron mobility, and excellent thermal conductivity, making it an ideal candidate for high-power and high-frequency applications.

Martian rovers, such as Curiosity and Perseverance, illustrate the challenges posed by radiation on Mars. Exposed to extreme levels of cosmic radiation due to the absence of a dense atmosphere and a protective magnetic field on Mars, their onboard systems are designed to be "hardened," meaning they are reinforced with specific materials and architectures capable of tolerating partial failures. One example is the RAD750 processor, used in the Curiosity rover as well as in the James Webb Space Telescope^{1, 2}. Aboard the International Space Station (ISS), which orbits about 400 km above Earth, radiation exposure is also a major concern. The electronic components of scientific instruments and onboard cameras are directly exposed to streams of energetic particles from the Sun and galactic cosmic rays. One observable effect is the presence of "dead pixels" or "artifacts"

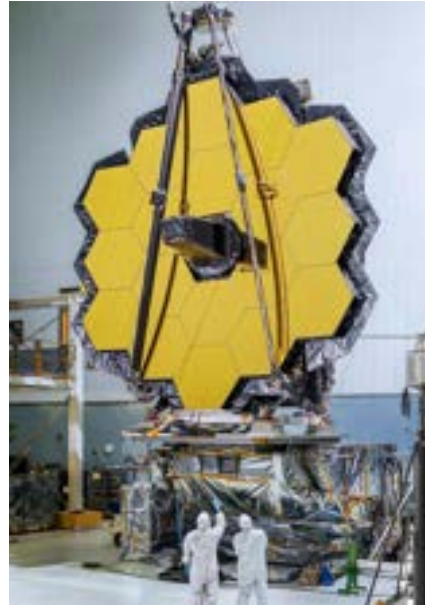
¹D.McComas "Lessons from 30 years of flight software", Nasa, 2022, <https://ntrs.nasa.gov/api/citations/20150019915>

²Nasa website, consulted on december 2024, <https://ntrs.nasa.gov/api/citations/20220015103>

that appear in videos and images captured from the ISS, resulting from the alteration of digital sensors by radiation as shown in Figure 1a. These degradations not only impose constraints on scientific operations but also highlight the need to improve the resilience of onboard technologies.



(a) Dead pixels in an ISS video.



(b) James Webb space telescope.

Figure 1: (a) Dead pixels (circled in red) visible in ISS videos due to radiation effects, and (b) Engineers at Goddard Space Flight Center inspect the 6.5-meter diameter JWST primary mirror after installation of the 18 hexagonal mirror segments. Credit: NASA.

These challenges are not limited to space. On Earth, environments such as nuclear power plants are also high-radiation zones where the reliability of electronic equipment is crucial. Control, safety, and automation systems must operate flawlessly, even under the influence of ionizing radiation. Thus, whether for exploring distant planets, maintaining a human presence in space, or ensuring the safety of critical infrastructure on Earth, hardening microelectronic technologies against radiation is a strategic priority. The increasing complexity and miniaturization of electronic components create new vulnerabilities, making it essential to understand radiation-electronics interactions at the atomic scale to ensure the longevity and performance of these systems in extreme environments.

In this context, this thesis addresses fundamental challenges in radiation hardening research: (1) the need for a comprehensive understanding of radiation effects across multiple time and length scales, (2) the accurate determination of key material parameters for radiation damage modeling, with the goal of improving the prediction capabilities for radiation effects in emerging semiconductor materials.

Radiation can be classified into two main categories: ionizing and non-ionizing. Ion-

izing radiation removes electrons from atoms, causing direct ionization. In contrast, non-ionizing radiation has significant effects on materials by displacing atoms from their equilibrium sites. In the context of electronic systems and exposed environments, it is this non-ionizing radiation that draws our focus, particularly the collision cascades it generates. Collision cascades occur when an incoming particle with non-zero mass interacts with a material's crystalline lattice. As the energetic particle penetrates the material, it transfers energy to lattice atoms, creating primary knock-on atoms (PKAs) - atoms displaced from their equilibrium positions. These atoms will collide with other atoms in the material, displacing them. These displaced atoms are referred to as secondary knock-on atoms (SKAs), and so on, until the energy is no longer sufficient to displace atoms through collisions. These displacements create crystalline defects, which significantly impact electronic device performance. For instance, in imaging sensors, they increase dark current - a parasitic current that creates "hot pixels", see figure 1a, rendering affected pixels unable to respond correctly.

Understanding these effects at the atomic scale becomes crucial for developing more resilient technologies. The motion of atoms and electrons involved in these interactions occurs on extremely short timescales. While experimental studies provide valuable insights, they are often limited by the extremely short timescales of radiation-matter interactions and the difficulty of in-situ observation of defect formation. Previous research has attempted to address these challenges through simulation, but often focusing on single-scale methods that cannot capture the full complexity of radiation-matter interactions.

To address these challenges, we use a range of numerical simulation tools, each carefully chosen to analyze specific phenomena. These tools provide specialized approaches that simulate distinct aspects of the radiation interaction process. Combining these methods enables a comprehensive and precise understanding of the impact of radiation on materials and electronic devices. Nevertheless, it remains essential to refer to experimental results whenever possible to ensure scientific rigor and validate the simulations effectively. This thesis investigates the radiation resistance of gallium nitride through a multiscale simulation approach, including quantum mechanical approaches that was neglected in previous research. A crucial parameter in assessing a material's radiation resistance is defect formation, which hinges on determining the threshold displacement energy (TDE)—the minimum energy required to permanently displace an atom from its equilibrium position. The TDE is an important parameter often used as input in simulations, such as those employing the Monte Carlo method, to study particle-matter interactions.

To explore collision cascades and determine TDE values in GaN, our methodology combines three primary simulation techniques:

- Monte Carlo simulations for initial particle-matter interactions which offers valuable insights into the initial stage of the process.
- Molecular dynamics for detailed analysis of collision cascades and defect formation.
- Ab initio molecular dynamics for precise quantum-mechanical modeling of atomic

interactions and TDE estimation.

Chapter 1 presents the context of the study, beginning with an overview of radiative environments and radiation fundamentals. It then presents the basic functioning of micro-electronics, the particle-matter interaction, and concludes with a discussion on gallium nitride (GaN) and its unique properties.

Chapter 2 describes our methodological approach and details the numerical simulation methods used throughout this study.

Chapter 3 examines collision cascades, applying the concepts introduced in previous chapters. This chapter employs both Monte Carlo simulations, which provide a statistical approach to the initial interaction between radiation particles and the material, and molecular dynamics simulations, which offer a detailed atomistic perspective of the ballistic phase and defect formation. By combining these methods, a comprehensive view of the cascade dynamics is developed, shedding light on how radiation impacts the atomic structure of GaN at the energies and time scales studied.

Expanding on the insights from the collision cascade analysis, the 4th chapter focuses on the threshold displacement energy (TDE), a key parameter that determines the material's resistance to radiation-induced defects. This chapter presents molecular dynamics (MD) while *ab initio* molecular dynamics (AIMD) methods are applied for a more precise quantum-mechanical understanding of the atomic interactions. By combining these approaches, the chapter provides a detailed evaluation of the TDE, contributing to a deeper understanding of GaN's behaviour to radiation.

Chapter 1:

Radiation Impacts on Electronic Devices

Contents

1.1	Introduction	12
1.2	Understanding Radiation: Environments and Effects	12
1.2.1	Radiations	12
1.2.2	Radiation environments	13
1.2.2.1	Artificial environments	13
1.2.2.2	Terrestrial environments	14
1.2.2.3	Spatial environments	14
1.3	Particle-matter interactions and basic microelectronics	18
1.3.1	Effects of radiation particle	19
1.3.1.1	Charged particles	19
1.3.1.2	Photons	19
1.3.1.3	Neutrons	20
1.3.2	Microelectronics basics	20
1.3.2.1	Metal-Oxide Semiconductor	21
1.3.2.2	Complementary Metal-Oxide Semiconductor	22
1.3.2.3	High-Electron-Mobility Transistor	23
1.3.3	Radiation effects and degradation mechanisms	25
1.3.3.1	Definitions of Key Terms	25
1.3.3.2	Dose rate	26
1.3.3.3	Single event effect	27
1.3.3.4	Ionizing dose	29
1.3.3.5	Displacement damage dose	30
1.3.3.6	Displacement damage degradation mechanisms and their impact on larger scale	31
1.4	State of the art: Gallium nitride	34

1.4.1	Gallium Nitride	34
1.4.1.1	History of gallium nitride	34
1.4.1.2	GaN radiation resistance	38
1.5	Conclusion	40

1.1 Introduction

Microelectronics are essential to many fields taking place in radiation environments such as nuclear power plants, large physics instruments and space missions.

However microelectronics exposed to such hostile environment can be damaged permanently or temporarily, thus compromising the success of the mission for which they are used. These effects on microelectronic components at the macroscopic scale come from different physical phenomena occurring at the atomic scale. The nature of these interactions is different and depends mainly on the essence of the radiative environment and the response of the components on a lot of parameters. To mitigate these effects, radiation-resistant materials can help harden electronic components. Since 2010s, gallium nitride GaN, a semiconductor with promising radiation-resistant properties, is back into the spotlight for several applications and is the subject of our study.

It is important to have a good knowledge of the radiation environment as well as particles and microelectronics in order to better understand what happens when everything is put together. For this reason, Section 1.2 presents the radiation environments as well as radiations, Section 1.3 will present particle-matter interaction and the basic operation of electronic components. Finally, the interesting GaN semiconductor is presented in the state of the art Section 1.4.

1.2 Understanding Radiation: Environments and Effects

From space radiation that has traveled millions of light-years and carries very high energies, to the radiation emitted by our sun at approximately 3.26 A.U., and including radiation artificially produced by nuclear reactors, this section aims at addressing the various natural and artificial radiation environments. To achieve this, it is necessary to define: what is radiations.

1.2.1 Radiations

The first radiation was observed, in November 1895, when Wilhelm Conrad Röntgen came across X-rays in his laboratory at the University of Würzburg. (X for unknown, which of course, they no longer are [1]).

A year later, a French physicist named Henri Becquerel made a fundamental discovery in atomic physics. On a cloudy day, Becquerel could not expose his phosphorescent uranium salts to sunlight. He then proceeded to store them in a drawer where he had already placed an unused photographic plate, protected by black paper. After a few days, this plate showed traces of radiation even though the salts had been kept away from light. Becquerel then realized that this radiation, which he called "uranic rays," was emitted by several uranium salts, whether phosphorescent or not. He thus discovered radioactivity. A few years later, the studies of Pierre and Marie Curie led to the discovery of two radioactive elements, polonium and radium. In 1912, Victor Hess and two of his assistants discovered



Figure 1.1: The famous X-ray picture of the hand of Albert von Kolliker [1].

radiations coming from beyond our atmosphere at very high altitude: cosmic rays [2].

Finally, major advances emerged in the 20th century, with the discovery of neutrons (1932) by James Chadwick, and nuclear fission (1938) by Lise Meitner and Otto Hahn.

To illustrate what radiation is, we can use these historical discoveries as support. Radiation is a process of energy transfer that occurs either in the form of electromagnetic waves, such as X-rays (which consist of photons), or as other particles, such as neutrons.

1.2.2 Radiation environments

What do the International Space Station (ISS), a nuclear reactor, the LHS' detectors, an airplane, and the Voyager 2 probe have in common? Each one contains electronic equipment subjected to a radiation environment. In order to better understand the potential effects of radiation on electronics in each of these environments, we will detail the nature of the different radiation environments that can be encountered.

1.2.2.1 Artificial environments

The first thing that comes to mind when we mention the word 'radiation' is 'nuclear'. Those words can evoke a negative connotation but can also indicate technical prowess, especially in artificial radiation environments such as nuclear power plants, medical instruments or particle accelerators.

The fuel used in nuclear power plants is uranium-235 (^{235}U). The uranium atoms in

the fuel pellets absorb slow (thermal) neutrons. When a ^{235}U atom captures a neutron, it becomes unstable and splits into two lighter nuclei, releasing a large amount of energy in the form of heat, as well as several additional neutrons to continue the fission and gamma rays. Electronics is used to measure the reactivity of the reactor core (a parameter defining the core's deviation from criticality), as well as for the storage and handling of radioactive waste. Therefore, it is mandatory to have hardened electronics in this environment.

For particle accelerators, the pressure to have hardened electronics is less significant because thick shielding protects them. However, this is different with the Large Hadron Collider (LHC) and the upcoming Future Circular Collider (FCC), recently presented by CERN, which will be three times larger than its predecessor. The very high energy (13.6 TeV) and the frequency of collisions achieved in the LHC indeed require in situ event pre-processing; the electronics of the particle detectors must necessarily be radiation-hardened.

It is impossible not to mention the Laser Mégajoule (LMJ) at CESTA, constructed thanks to the CEA's Simulation Program, which combines simulation and experimentation, where the electronics is hardened. In the same way, there is the International Thermonuclear Experimental Reactor (ITER) project, which will also require radiation-hardened electronics to counteract the high energy particle created inside the plasma.

1.2.2.2 Terrestrial environments

Cosmic-rays traveling through space can be stopped and trapped by the magnetosphere and the Van Allen belts, whose description will be detailed in Section 1.2.2.3. However, if these particles manage to pass through these two regions, they can reach the Earth's atmospheric layer and interact with it. The radiation particle is slowed down by interacting with atmospheric nitrogen and oxygen, forming a cascade of secondary particles, called shower shown Figure 1.2, primarily neutrons that can reach up to hundreds of MeV (but also protons, electrons, neutrons, heavy ions, muons, and pions in smaller quantities)[3].

These atmospheric neutrons can induce heavy ions through nuclear reactions and are thus indirectly responsible for errors in electronic components [4].

In addition to these cosmic-origin induced particles, there are also particles produced by the radioactive decay of heavy atoms like uranium and thorium, which are present in the form of traces in all terrestrial matter. These include alpha particles such as helium nuclei, from terrestrial activity, particularly found in the materials used for ceramic packages and solder wires.

1.2.2.3 Spatial environments

Space is another example of a radiation environment given here. It can be described in several sub-sections, such as solar flares, the Van Allen belts or the galactic cosmic rays.

A majority of the particles emitted by our sun or traveling through space toward Earth is stopped by the magnetosphere, which is the region where physical phenomena are

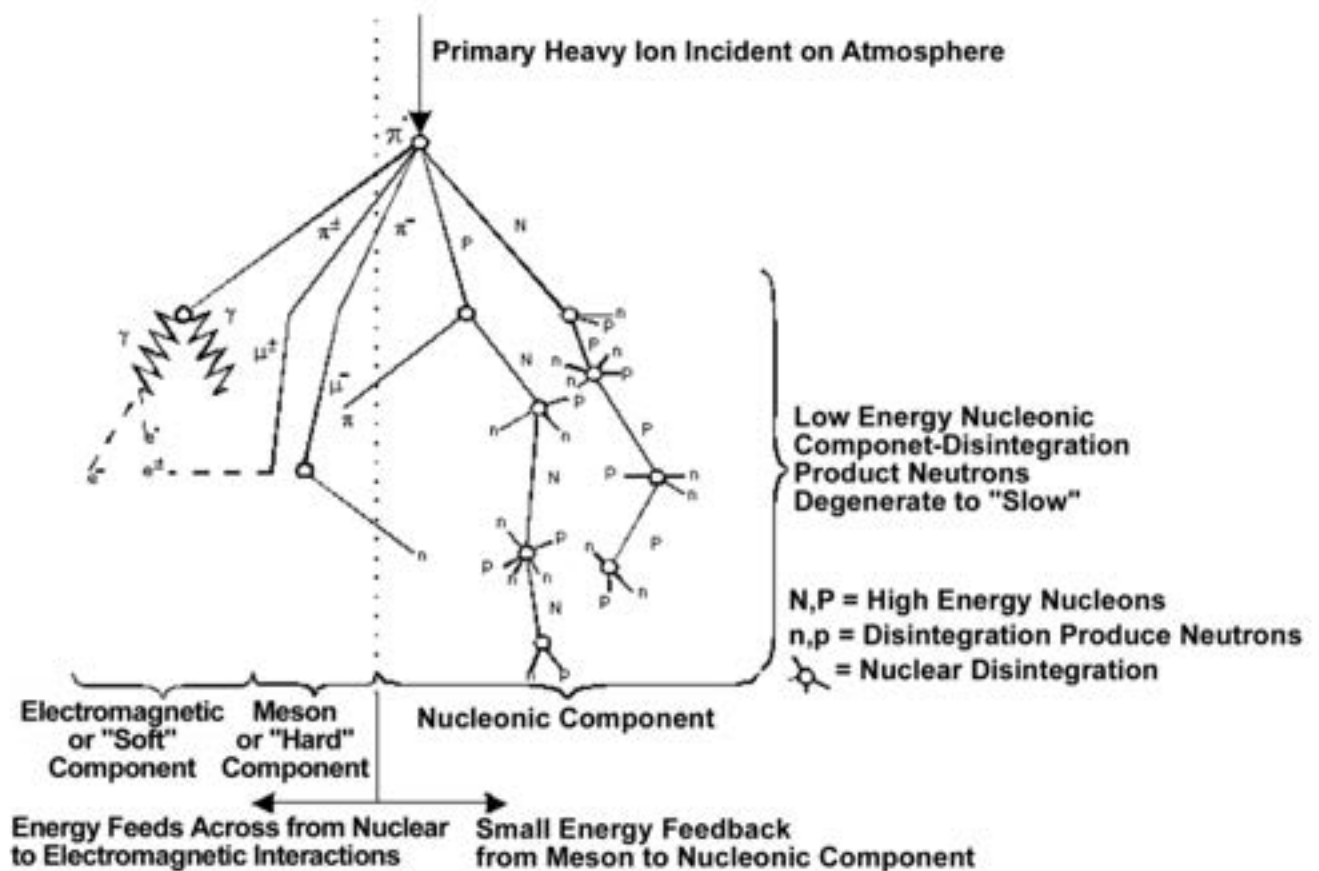


Figure 1.2: Cosmic rays hit the top of the atmosphere and disintegrate into neutrons, pions, muons [3].

dominated or organized by Earth's magnetic field. However, some of the particles are trapped in two toroidal zones surrounding Earth, commonly known as the Van Allen radiation belts.

The "inner" belt is located between 1,000 km and 10,000 km in altitude, while the outer belt is located between 13,000 km and 65,000 km in altitude see Figure 1.3. These belts are composed of electrons, protons, and heavy ions. The trapped electrons have energies up to 7 MeV, while the energies of trapped protons and heavy ions go up to hundreds of MeV/nucleon. In these belts, the abundance of heavy ions with enough energy to penetrate satellite shielding is, however, too low for them to be a dominant factor in the sensitivity of onboard electronic components.

Once we exit the magnetosphere, we are exposed to solar events and galactic cosmic rays. Solar events can be divided into two categories: solar winds and solar flares.

Solar winds are continuous events consisting of the emission of a flux of particles with energies ranging from a few keV to about ten keV. This continuous emission creates a

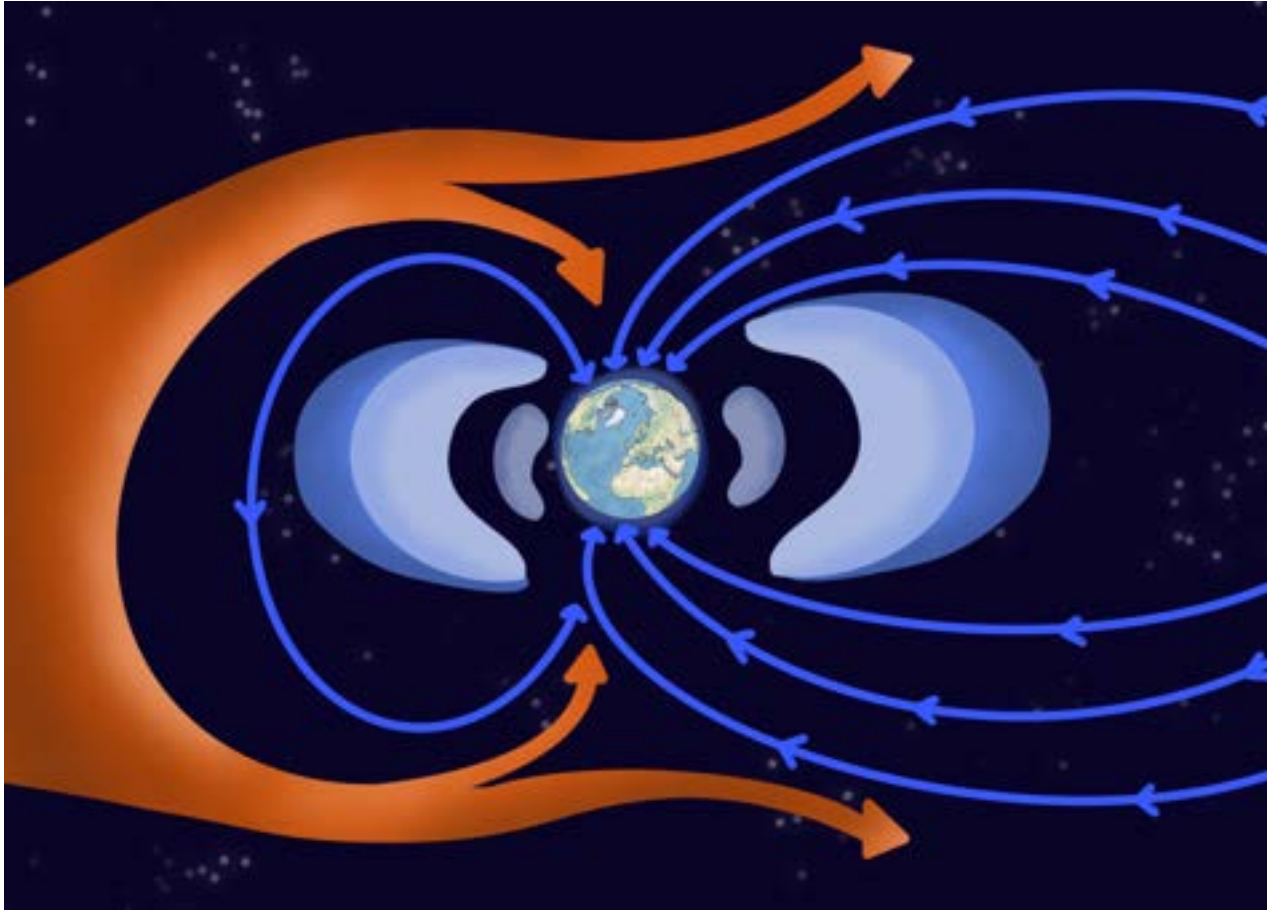


Figure 1.3: The Van Allen radiation belts (light blue) [5].

plasma throughout the solar system called the heliosphere. The flux is approximately 10^9 particles/cm²/second, and a thin layer of material provides protection against it.

On the other hand, solar flares are periodic events, that depend on solar activity, which can be traced by the number of sunspots visible on its surface, as shown in Figure 1.4. There are two types of solar flare: protonic flares, which last from a few hours to a few days, and occur about ten times a year. The protons emitted can reach energies of the order of a hundred MeV. Finally, there are heavy ion flares, where the composition of the ion emission varies depending on the characteristics of the eruption, and the ions can also reach a hundred MeV.

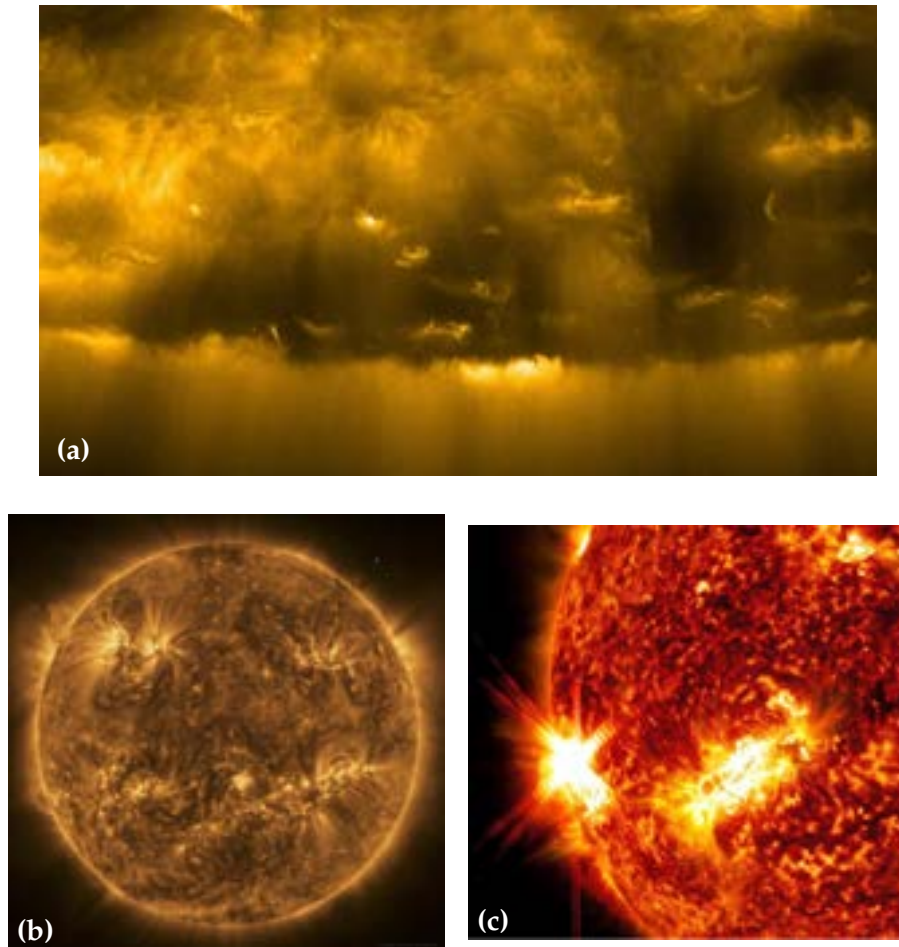


Figure 1.4: (a) South Pole of the Sun. (b) Gases in the Sun's atmosphere that reach a temperature of around 1 million degrees Celsius. (c) Shot of one of the most intense solar flares ever observed, on 9 January 2023. Sequence of UV images captured by the Solar Orbiter probe as it approached the Sun in 2022. Photographs a) and b) credit: ESA & NASA/ Solar Orbiter team/ EUI. Photograph c) credit: NASA Solar Dynamics Observatory.

Finally, there is galactic cosmic radiation, whose emissions result from events occurring beyond our solar system, even beyond our galaxy. These events eject particles at speeds close to that of light, giving them very high energy. Galactic cosmic radiation is mainly composed of protons, followed by alpha particles, electrons, and heavy ions.

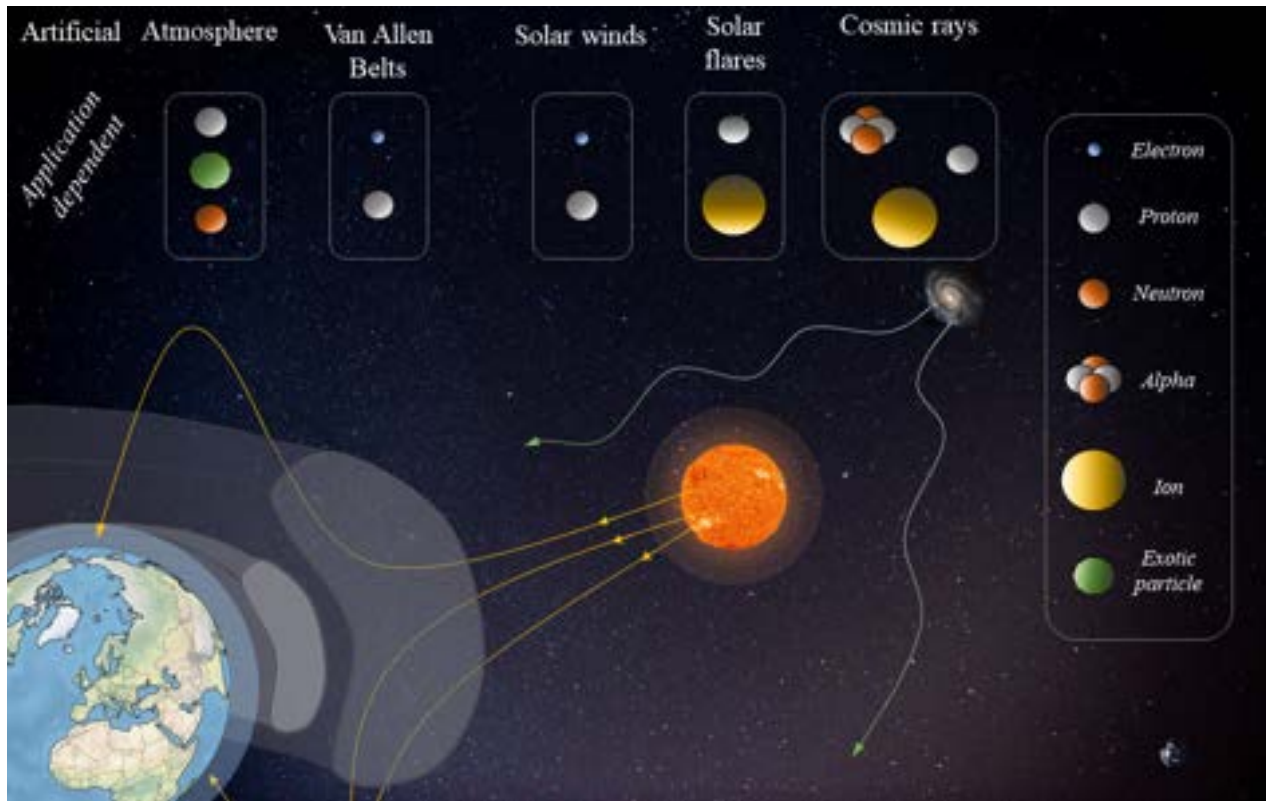


Figure 1.5: Schematic overview of the different radiation environments and the particles that constitute them.

Figure 1.5 shows a summary of the different radiation environments presented previously. Not all particles are present in every environment. The energy of the same type of particle varies depending on the environment. A proton originating from the galactic cosmic background can reach up to 1 TeV/nucleon, while a proton in the Van Allen belt will have an energy of around a hundred MeV. Heavy ions are found in cosmic radiation as well as in solar flares. Electrons trapped in the radiation belts will be more energetic (<7 MeV) than electrons coming from solar winds (a few keV).

1.3 Particle-matter interactions and basic microelectronics

In these radiation environments, microelectronic components can be exposed to significant fluxes of energetic particles. These particles transfer their kinetic energy to the atoms and/or electrons of the material constituting the microelectronic components, resulting in the displacement of atoms from their equilibrium sites and/or the excitation of electrons through ionization.

In a semiconductor component, this results in four different electrical effects that can alter the behavior of electronic circuits and hinder their proper functioning. This section will first present the different interactions depending on the type of particle composing the radiation and the four effects, with a focus on atomic displacement, which is the main consequence of radiation studied in this work. Then, after a brief overview of the structure

of Metal-Oxide-Semiconductor (MOS), Metal-Oxide-Semiconductor Field-Effect Transistor (MOSFET) and High-Electron-Mobility transistor (HEMT) components, Section 1.3.1 will presents the degradation mechanisms on transistors and the materials comprising them. Finally, the last part will focus on the impact of these degradations on a larger scale.

1.3.1 Effects of radiation particle

The numerous particles that can constitute radiation differ in their characteristics and their interaction with matter. Heavy ions, emitted by galactic cosmic radiation, for example, possess mass and charge, and thus can interact with materials in various ways. A neutron, on the other hand, has mass but no charge, so it will tend to interact mainly through collisions with atoms. Photons have no charge and generally contribute to ionization, although photo-nuclear reactions are possible at very high energies. Electrons, having very little mass, predominantly create electron-hole pairs or parasitic currents and cause a small amount of displacement damage.

1.3.1.1 Charged particles

When a heavy ion, an electron, or a proton penetrates matter, it interacts with the electrons of the material's atoms under the influence of Coulomb forces (inelastically), and more rarely with the atomic nuclei. For example, the ion transfers its energy to the electrons, which in turn transfer their energy to other electrons, resulting in a cascade of secondary electrons that lose their energy through ionization. This interaction is the cornerstone of electronic stopping power. The purpose of electronic stopping power is to quantify the energy lost per unit distance traveled by a charged particle (interacting via Coulomb forces with the electrons of the material).

If a charged particle penetrates the electrons cloud and interacts with the nuclei without touching it, it can still be deflected by Coulomb interactions with the nuclei. If this does not happen, the collision occurs, and the particle may displace the atomic nucleus from its original position through nuclear Coulomb (elastic) interactions. If the particle's energy is very high, it may trigger a nuclear spallation reaction.

1.3.1.2 Photons

Photons primarily interact with the electrons of the atoms in the material through three classical effects: the photoelectric effect, the Compton scattering and pair production. The relative probability of one mechanism occurring over another depends on the energy of the incident photon as well as the mass of the atoms in the target material.

- The photoelectric effect: An atom absorbs the energy of an incident photon and releases an electron. The photon's energy is entirely absorbed and must be greater than the binding energy U_i of the electron [6].

- Compton scattering: An atom absorbs part of the energy of an incident photon and releases an electron. Only a portion of the photon's energy is transferred, the photon is deflected, and it can continue on its way [7].
- Pair production: An atom absorbs the energy of an incident photon, resulting in the production of an electron-positron pair. The incident energy must be greater than 1.022 MeV for the creation to occur (which is the rest mass energy of an electron and a positron, 2×511 keV).

There is also the coherent scattering (or Rayleigh scattering), where an atom absorbs a negligible amount of energy from an incident photon, which is then only deflected.

Finally, photons can interact with atomic nuclei through excitation or a nuclear reaction (known as photo-nuclear reactions), but this occurs at very high energies (typically beyond several MeV), with the threshold depending on the atoms of the target material [8] [9].

1.3.1.3 Neutrons

As mentioned previously, the neutron is an uncharged particle, so it cannot interact coulombically with the electrons and nuclei of atoms of the matter. The chances of a neutron colliding with an electron are very low and will not be addressed here [10]. However, an incident neutron can interact with a nuclei in two different ways.

- Through elastic collision: In this interaction, the neutron transfers its kinetic energy to the nuclei, displacing it from its equilibrium site,
- Through inelastic collision: In this case, the impacted nuclei is excited and can de-excite by emitting particles such as deuterium or helium nuclei, γ -rays, or neutrons. In the case of a collision with a heavy nuclei, it is possible for the neutron to cause the nuclei to fission (nuclear reaction) into two intermediate-mass fragments and a few particles.

The section presents the atomic-scale interactions between radiation particles and the particles that make up matter. The next section will take a broader perspective and examine the mechanisms on a larger scale.

1.3.2 Microelectronics basics

It is necessary to introduce basic components such as MOSFET and HEMT. Therefore, this section is organized as follows: First, we provide a brief introduction to basic electronic components and their operation. We will then focus on the four effects of radiation in electronics, but before doing so, key terms must be defined. The four effects are: the single event effect, dose rate, ionizing dose, and non-ionizing dose effects.

1.3.2.1 Metal-Oxide Semiconductor

Electronics are widely present in radiation environments shown in Section 1.2.2, often to control settings and devices through sensors, cameras, or screens. Radiation can have severe consequences on these devices. To better understand the impact on microelectronics, it is then important to understand the functioning of basic components.

When we mention electronics, many picture a phone or the familiar green and gold circuit board. These macroscopic components are all created from the basic building block of most electronic devices: the transistor.

To begin with, a MOS transistor is a type of field-effect transistor (FET). Typically, it includes three terminals: the Gate (G), Source (S), and Drain (D). The key components of a MOS transistor are a semiconductor channel, a metal gate, an insulating oxide layer and the terminals as shown on Figure 1.6.

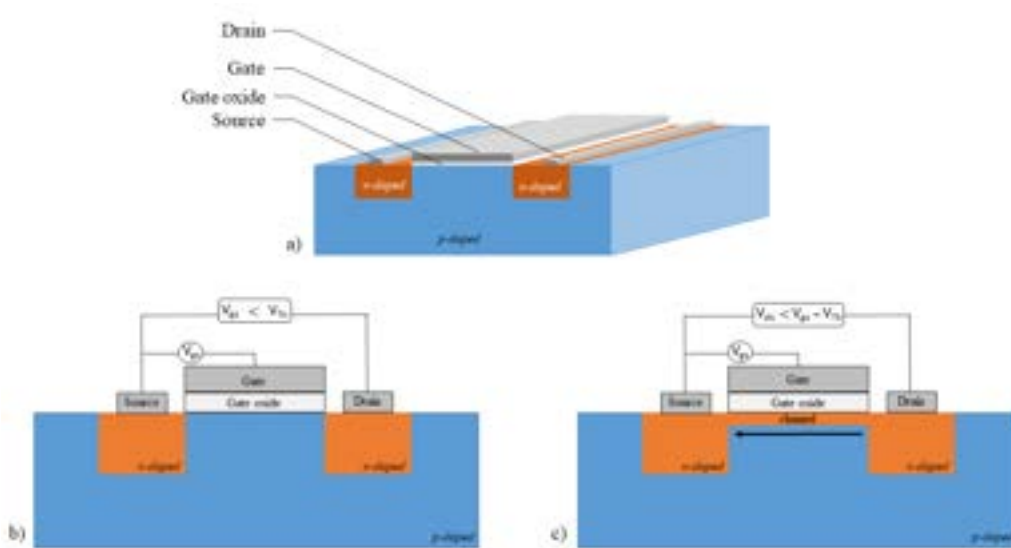


Figure 1.6: Schematic cross section view of a n-MOSFET. With a) the description of the layers, b) Closed (No current created between the N-doped regions) c) Open (The current channel is created).

A MOS transistor operates as a voltage-controlled device, meaning that the control of its operation or the current passing through the semiconductor channel is achieved by altering the voltage applied to the gate (gate voltage). The gate is composed of metal and is isolated from the semiconductor channel by a silicon dioxide insulating layer. This setup enables the gate voltage to establish an electric field within the semiconductor channel, thereby controlling its electrical conductivity and, consequently the current.

How is this current generated? Here is a more detailed explanation. As shown in Figure 1.6, the drain and source are n-doped, and the bulk (the semiconductor channel

part separating the source and drain) is p-doped. An n-doped material will have an excess of electrons, whereas a p-doped material will have a deficit of electrons, and will have what is known as an excess of holes (positive charge carriers). It is due to the different characteristics of these regions and the use of the gate that the current is formed. The source acts as the entry point for the current, the semiconductor channel acts as a bridge between the source and the drain, the gate controls the current flow through this bridge and finally the drain serves as an exit for the current.

A MOSFET can function in both depletion mode and enhancement mode:

- Enhancement mode: the transistor is off by default (no current flows without gate voltage) and requires a gate voltage to be turned on. More precisely and for N-MOS (p-doped drain and source, n-doped semiconductor channel), when the gate-to-source voltage (V_{GS}) is above a certain threshold (V_{Th}), an n-type channel is formed, allowing current to flow between source to drain. If V_{GS} is less than V_{Th} , the MOSFET is 'off' (no current flows). For P-MOS (p-doped drain and source, n-doped semiconductor channel), the polarity is reversed.
- Depletion mode: The transistor is turned on by default (current flows without gate voltage) and requires a gate voltage to be turned off or to reduce the current.

1.3.2.2 Complementary Metal-Oxide Semiconductor

A CMOS is a specific type of MOS, using a complementary arrangement, as the name implies, of an N-MOS and a P-MOS. The contact between the two MOS devices forms a junction called a P-N junction. The functioning of this junction is fundamental to CMOS technology.

In a P-N junction, the P region (doped with acceptors) is rich in holes (majority carriers) and poor in electrons (minority carriers), while the N region (doped with donors) is rich in electrons (majority carriers) and poor in holes (minority carriers). When the junction is formed, electrons from the N side and holes from the P side diffuse across the junction. At the interface, between the two MOS (at the junction), the holes and electrons recombine. This area will be depleted of charge carriers and it is called the depletion region. In this region, only the negatively charged dopant ions on the P side and the positively charged dopant ions on the N side will remain. The P side of the region is negatively charged, and the N side is positively charged, as shown in Figure 1.7. This creates an internal electric field (junction voltage), which counteracts the diffusion of charge carriers and stabilizes the junction.

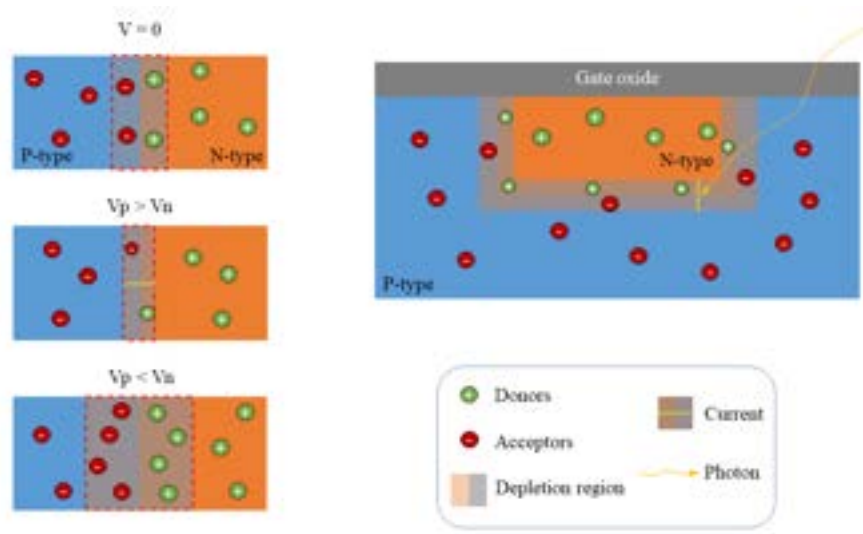


Figure 1.7: Schematic cross section view of a P-N junction (left) and a Complementary Metal-Oxide-Semiconductor (CMOS) (right). On the left, the different states of the depletion region at the P-N junction depending on the current applied. On the right, a Complementary Metal-Oxide-Semiconductor (CMOS) Charge-coupled Device (Charged-Coupled Device) with the capture of a photon producing current at the P-N junction.

It is now possible to control the flow of charge carriers by applying a voltage between the two MOS devices. In direct bias ($V_p > V_n$), the potential barrier will decrease (reducing the depletion region), allowing the carriers to cross the junction. Conversely, when a reverse bias is applied ($V_p < V_n$), the potential barrier increases (expanding the depletion region) and prevents the charge carriers from crossing the junction, as shown in Figure 1.7.

A widely used device that operates based on these mechanisms is the Complementary Metal-Oxide-Semiconductor (CMOS) photodiode. As a component of image sensors, the CMOS photodiode detects the passage of a photon through the depletion region, creating an electron-hole pair. The pair is separated by the junction voltage, with electrons being attracted to the N region and holes to the P region, generating a current (see Figure 1.7). This current can then be converted into voltage and further processed.

1.3.2.3 High-Electron-Mobility Transistor

Among the Field-Effect Transistor (FET), HEMT are transistors operating on the principle of creating a conductive channel in the form of a two-dimensional electron gas (2DEG), which enables higher performance to be achieved than with conventional transistors. The most promising heterostructure for HEMTs is the AlGaIn/GaN one.

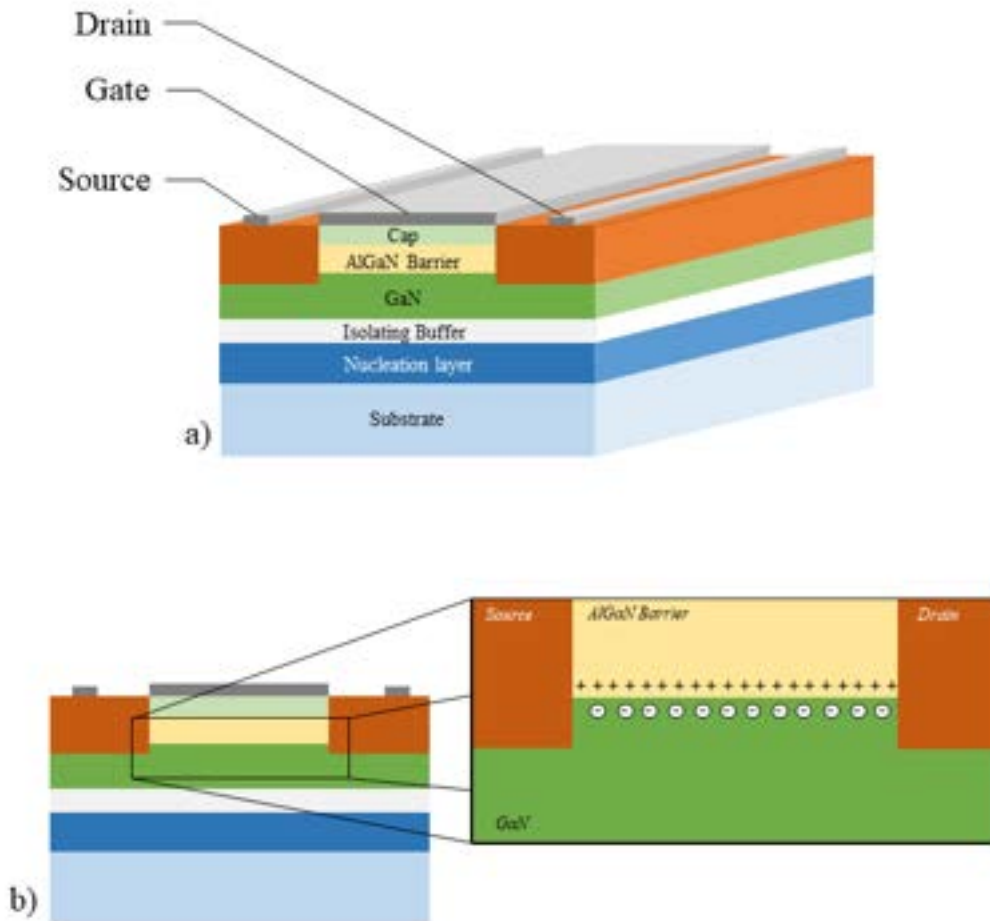


Figure 1.8: Schematic cross section view of an HEMT AlGaIn/GaN. With a) the description of the different layers and b) the two-dimensional electron gas.

The structure of a HEMT has similarities with that of a MOS transistor; however, it is more complex in its layer stacking, as illustrated in Figure 1.8.

From bottom to top, the first layer is the substrate layer, which serves as a support layer, forming the base on which all other layers are deposited. Next, the buffer layer is introduced, which improves the crystalline quality of the layers deposited above it. This is essential for the proper functioning of the device, as it helps to reduce dislocations and crystalline defects that could arise due to differences between the substrate and the other layers.

The insulating layer contains the 2DEG with very high electron mobility. Finally, the doping layer is added to increase the concentration of electrons in the channel, thereby improving the device's conductivity.

The cornerstone of the AlGaIn/GaN HEMT relies on the 2DEG channel created in the semiconductor layer. The juxtaposition of the AlGaIn/GaN layers (heterostructure) induces a local modification of the conduction bands of the materials. At this interface,

a potential well is created, trapping the electrons and confining them within a channel between the source and the drain, as shown in Figure 1.8. It is called "two-dimensional" because it is confined perpendicularly between the source and the drain but free to move within a very small space at the interface between the two semiconductors. Being in a confined area, thus far from material imperfections, the electrons exhibit a very high mobility. Just like in an NMOS, these electrons move between the source and the drain, and the current can be modified by applying a voltage to the gate.

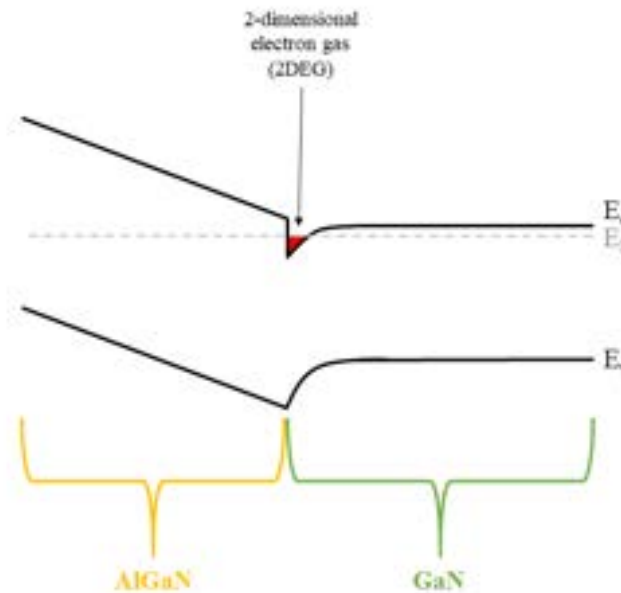


Figure 1.9: 2DEG electron channel.

Thanks to the 2DEG, HEMTs exhibit very interesting characteristics, enabling for increased efficiency, faster switching times, and reduced energy loss. HEMTs can also operate at very high frequencies (GHz) and at very high temperatures. In short, HEMTs are interesting devices, and we will have the opportunity to revisit them in Section 1.4.1.1.

Now, we turn on to the four effects of radiation on microelectronic devices. These effects are categorized into two groups:

- transient effects, which are characterized by a brief pulse of multiple particles, such as Single Event Effects and dose rate,
- cumulative effects, such as total ionizing dose and total non-ionizing dose.

1.3.3 Radiation effects and degradation mechanisms

1.3.3.1 Definitions of Key Terms

In the previous section, we discussed how particles from various radiation environments interact differently with matter. The main mechanism is as follows: when an

energetic particle passes through matter, it loses (or transmits) its energy according to two classes of energy loss: Ionizing Energy Loss (IEL) and Non-Ionizing Energy Loss (NIEL). The IEL class (Ionizing Energy Loss) indicates that the energy of the incident particle is lost due to interactions with the electrons of the target material. In the NIEL class (Non-Ionizing Energy Loss), the energy is lost due to the interactions with the nuclei of the target material.

Let's consider an ion as an example. When it penetrates matter, it first loses energy and slows down by interacting with the electron cloud of the material. The ion loses energy through these Coulombic interactions with the electrons and is known as IEL. This allows us to define the term "Electronic Stopping Force" (also known as Electronic stopping power). This new term defines the amount of energy lost per unit of distance as the charged particle in Coulomb interactions with the electrons of the target material, and it can also be written as the following nomenclature:

$$\left(\frac{dE}{dx}\right)_{\text{electronic}} \quad (1.1)$$

If the ion continues its trajectory within the material, it may interact with a nucleus if it manages to pass through the electron cloud. In such cases, a collision will occur, causing the ion to be deflected and lose some energy through (NIEL). If the energy is sufficient, the nucleus may be displaced from its equilibrium site via elastic Coulomb interactions. So the incident ion lost some energy via coulomb interactions with a nuclei, which can be define as the nuclear stopping force. It's the amount of energy lost per distance unit by a charged particle due to the nuclear coulomb interactions. It can also be written as the following nomenclature:

$$\left(\frac{dE}{dx}\right)_{\text{nuclear}} \quad (1.2)$$

The displacement of nuclei from their equilibrium position is called atomic displacement, and the accumulation of these displacements leads to deterioration of the crystalline structure. This accumulation of displacements is called displacement damage.

With the definition of stopping forces, it is possible to define the total force lost per unit distance due to electronic and nuclear Coulombic interactions:

$$\left(\frac{dE}{dx}\right) = \left(\frac{dE}{dx}\right)_{\text{electronic}} + \left(\frac{dE}{dx}\right)_{\text{nuclear}} \quad (1.3)$$

This term is frequently used in studies on particle matter interactions.

1.3.3.2 Dose rate

Dose rate refers to the rapid passage of multiple particles or radiation, such as photons or electrons. However, dose rate can also refer to the amount of radiation absorbed by a

material per unit of time, usually expressed in rads per second (rad/s).

The pulsed phenomenon is associated with a charge deposition in the material that ionizes it. An accumulation of free charges within the material can cause irreparable damage.

In electronic components, the consequences can include an overload leading to a short circuit, or latch-up, which is an overconsumption in a transistor. This phenomenon is often due to a high dose rate. There may also be disruptions in logic gates due to the sudden energy deposition, such as bit flips or errors during signal processing. This effect can extend to multiple components.

1.3.3.3 Single event effect

A Single Event Effect (SEE) can be a functional anomaly or a destructive effect in an electronic component, related to the interaction of a single particle with the material.

For example, consider a heavy ion; as it travels through the material, it will ionize it, meaning it will eject electrons from their positions. The excitation of these electrons will create electron-hole pairs (direct ionization), which will then settle in certain active areas of the semiconductor. Additionally, the heavy ion will also collide with the atoms of the material, potentially causing nuclear reactions or atomic displacement, leading to the creation of electron-hole pairs through ionization. Indirect ionization is rarely the origin of an SEE, except in the case of proton radiation, where ionization is the preferred mechanism, and neutron radiation, where it is the sole cause.

The electron-hole pairs created by ionization along the ion's path will be transported according to the drift and diffusion mechanisms. The charges are then collected at the terminals of the component, inducing a parasitic transient current. The characteristics of this transient depend on the type of irradiated component and the ion's impact point relative to the sensitive area of the transistor.

PN junctions reverse-biased present a wide depletion region and a region of significant electric field; they are the most likely to collect the charge. The electron-hole pairs are separated by the electric field at the junction in the depletion zone and then collected at the electrode of the irradiated component. Particles generated in the neutral zone may also diffuse toward the junction and be collected there.

We can distinguish three phases (see Figure 1.10):

1. Electron-hole pairs are generated along the path of an ionizing particle in the material.
2. A funnel is created by the distortion of the electric field lines and the drift of the carriers.
3. The carriers diffuse.

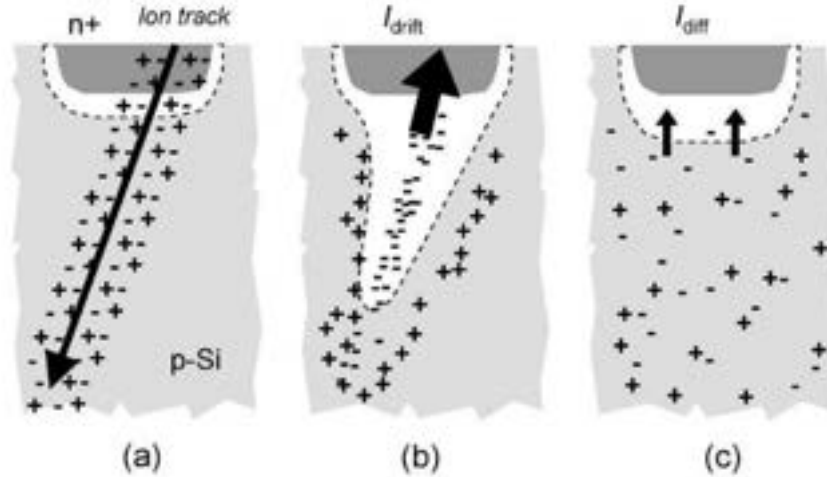


Figure 1.10: Charge Collection Mechanism in a Reverse-Biased PN Junction : (a) generation of electron-hole pairs as the ion passes through, (b) creation of a tunnel due to distortion of the electric field lines and carrier drift, (c) carrier diffusion [11] [12].

The charge collection by drift and diffusion typically results in an elementary transistor as a parasitic transient current (Figure 1.11) with an initial fast response (drift, "funneling" phenomenon), followed by a slower current (diffusion).

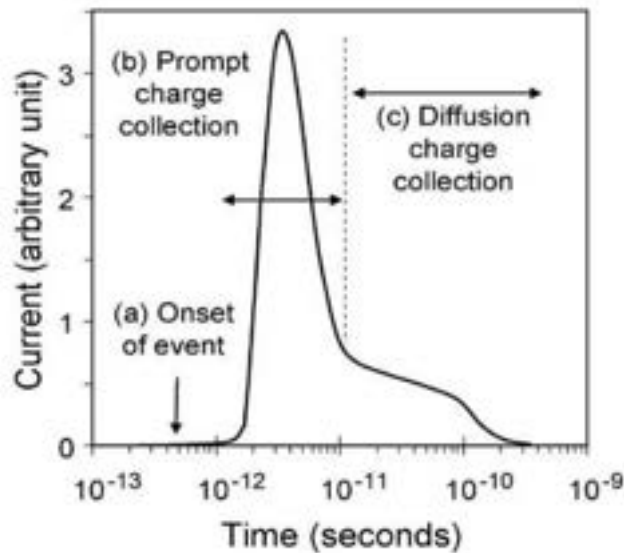


Figure 1.11: Example of transient current induced by charge collection in a reverse-biased PN junction [11, 12].

We refer to a non-destructive SEE when it temporarily alters the component's state or permanently alters it without affecting the component's functionality. A destructive SEE, on the other hand, permanently damages the component's capabilities or even destroys it. Depending on the damage's impact and location, several nomenclatures can classify

SEEs. For example, if there is a rupture of the oxide composing the gate (Single-Event Gate Rupture, SEGR) or if a parasitic signal appears (Single-Event Transient, SET).

1.3.3.4 Ionizing dose

The Total-Ionizing Dose (TID) is caused by the ionization of the material due to the cumulative effect of incident or secondary charged particles, such as electrons, protons, or heavy ions. TID describes the amount of energy per unit mass of matter absorbed by photonic absorption and by electronic stopping power and can be expressed as follows:

$$TID = IEL \times \phi(E) \quad (1.4)$$

with:

$$IEL = \frac{1}{\rho} \times \left(\frac{dE}{dx} \right)_{\text{electronic}} \quad (1.5)$$

$\phi(E)$ is the fluence (m^{-2}) of particle of energy E , ρ the density of the material and $\left(\frac{dE}{dx} \right)_{\text{electronic}}$ the electronic stopping power (MeV.cm^{-2}).

This allows us to quantify the cumulative ionisation dose in the material, *i.e.* the number of electron-hole pairs expressed according to:

$$N = \frac{TID \times \rho}{E_p} \quad (1.6)$$

with E_p the minimum energy necessary to create an electron-hole pair in a material (3.69 eV for Si and 2.62 eV for Ge [13][14]).

For electronics, particularly in MOSFET, this effect occurs in oxide-based dielectric materials that serve as insulators. Electron-hole pairs can be produced in insulators. Since the electrons have a higher mobility, most of them leave the insulator. But holes can be trapped, and migrate to the insulator-semiconductor interface as shown in Figure 1.12. Charges trapped at this interface degrade the operating parameters of a device by changing the threshold voltage which is the minimum gate-source voltage (V_{th}) required to create a conductive path between the source and drain terminals, for example. More precisely, holes gather at deep level sites produced by the lattice mismatch between SiO_2 and Si, and by the defects generated during the manufacturing process. The diffusion of holes to the interface via hopping between discret energy level states and deform the lattice that can favor the release of hydrogen impurity ions. Released ions diffuse to the interface and create interface traps. That is these traps that will produce the threshold voltage shift.

Pairs can also recombine due to the influence of temperature but if the component is active, the electric field reduces the probability of recombination by separating electrons from holes, leading to the trapping of the latter in the oxide and at the interface. Electron-hole pairs can also be created in Ge substrates, but these only induce transient parasitic

currents. As the trapped holes are positively charged, offset tends to be more of a problem in N-MOS than P-MOS.

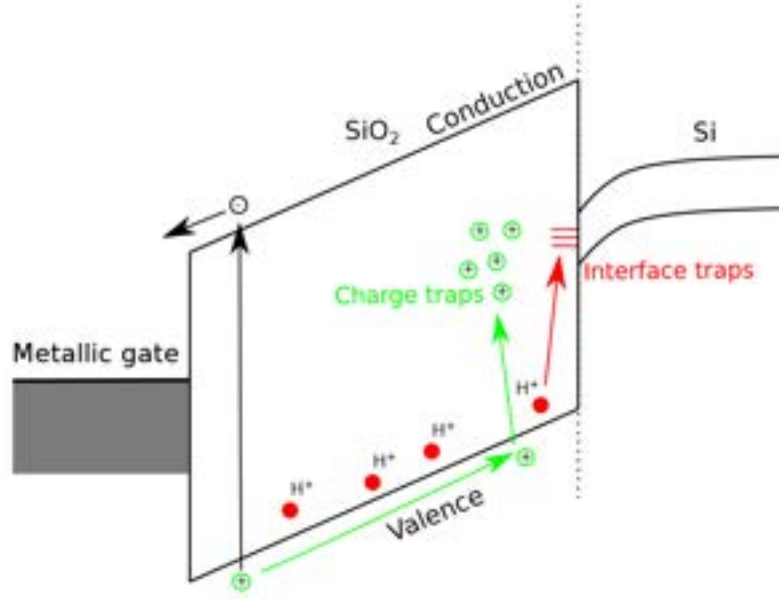


Figure 1.12: Schematic representation of the basic mechanisms of ionizing degradation in the band gap of a bulk MOS [14–16].

1.3.3.5 Displacement damage dose

The Displacement Damage Dose (DDD) correspond to the displacement of atoms from their crystalline sites due to the impact of particles such as neutrons, protons, or heavy ions. DDD quantifies the amount of energy per unit of mass of matter that is absorbed in the form of non-ionizing events. More simply, it quantifies the total damage caused to the crystal lattice by energetic particles. It can be expressed by the following equation:

$$DDD = \int_{E_{min}}^{E_{max}} NIEL(E) \times \frac{d\phi(E)}{dE} dE \quad (1.7)$$

with E_{min} and E_{max} respectively the minimum and maximum of the particle energy and as mentioned in Section 1.3.3.1, NIEL is the amount of energy lost by a single particle in a certain type of material (in MeV.cm²/g).

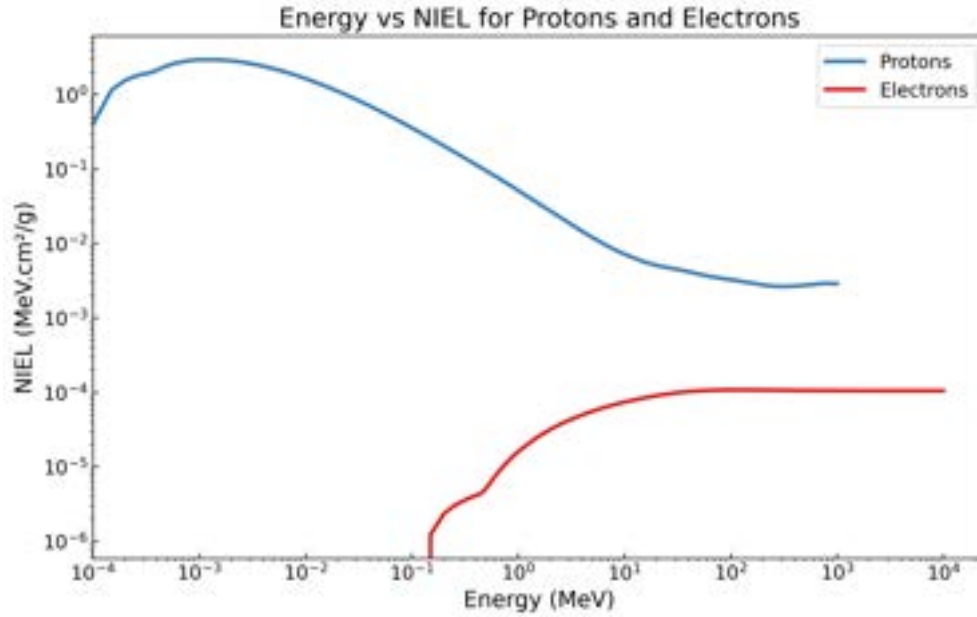


Figure 1.13: NIEL as a function of the energy for protons (blue) and electrons (red) in GaN. Obtained with SR-NIEL online calculator [17].

Figure 1.13 shows the NIEL as a function of the energy of an incident proton or electron. The energy deposited per surface unit in GaN is greater for protons than for electrons *i.e.* NIEL is greater for protons. However, the higher the energy of the proton, the lower the NIEL, since at very high energies the nuclear interaction cross section of protons decreases. For electrons, the NIEL increases with the energy of the electron and then remains constant above 100 MeV. The mass of electrons is much lower than that of protons, which explains why the NIEL of electrons is lower.

Although DDD has a greater impact on diodes or bipolar transistors, mechanisms in MOS transistors have been identified as originating from DDD: the increase in positive charge density in the SiO₂ layer, the increase in bulk resistivity, and the decrease in carrier mobility in the channel. In MOSFET, the most sensitive area is the electron channel in the semiconductor. In most devices, the dominant DDD degradation mechanism is an increase in positive charge density, the most obvious effect of which is an increase in switching voltage [18]. For HEMT, the main degradation mechanism is a reduction in the mobility of charge carriers [19].

A more detailed explanation of the creation of a fault as a result of displacement damage is given in the next section. An inventory of the effects of degradation on a larger scale is also provided to give a more concrete idea of the impact of defects at the atomic scale on components/devices at the macroscopic scale.

1.3.3.6 Displacement damage degradation mechanisms and their impact on larger scale

When a particle penetrates the material, if it is charged, it interacts with electrons of the said material. However, as explained in Section 1.3.3.5, they can also interact in

a non-ionizing manner, like neutrons. This non-ionizing interaction involves collisions through Coulomb forces (elastic) or strong forces (inelastic). For collisions involving strong forces (nuclear reactions), *i.e.* at very high energy, the incident particle will strike a first atom in the crystal that makes up the material. From this collision, the incident particle will exchange a significant amount of energy with the inert atom and split it into several high-energy secondary particles. For collisions via Coulomb forces, the incident particle will strike a first atom in the crystal called the primary knock-on atom (PKA), and energy will be transferred from the incident particle to the inert atom. This latter atom will then be displaced and will collide with other atoms in the crystal, which will then be called secondary knock-on atoms (SKA), and in turn, these will collide with other atoms, and so on. This succession of collisions is called a collision cascade, a key concept in this research work. The collision cascade ends when the transmitted energy is no longer sufficient to displace an atom.

During a collision cascade, the displaced atoms leave behind empty crystallographic sites, which are referred to as vacancies. The atoms can then lodge themselves in certain locations in the crystal that are not equilibrium sites, *i.e.* in the interstitial space between equilibrium sites of still-present atoms. These are called interstitial atoms. A vacancy and an interstitial form what is known as a Frenkel pair, and each is considered a defect, as is the pair. These defects destabilize the ordered structure of the crystal and create issues; they can act as traps for charge carriers or even cause mechanical problems if present in large numbers (like dislocations).

In compounds consisting of multiple elements, another defect can be created as a result of a collision cascade. For example, in a binary compound made up of type 1 and type 2 atoms, a type 1 atom can be displaced and occupy the equilibrium site of a type 2 atom, creating what is known as an antisite defect. This destabilizes the crystal lattice by corrupting the material's crystalline properties, impacting its chemistry.

The local grouping of defects is called a cluster. These clusters have a greater influence on the material's parameters. In the case of a MOS, CMOS, or HEMT, this large-scale disorder will alter the electrical characteristics.

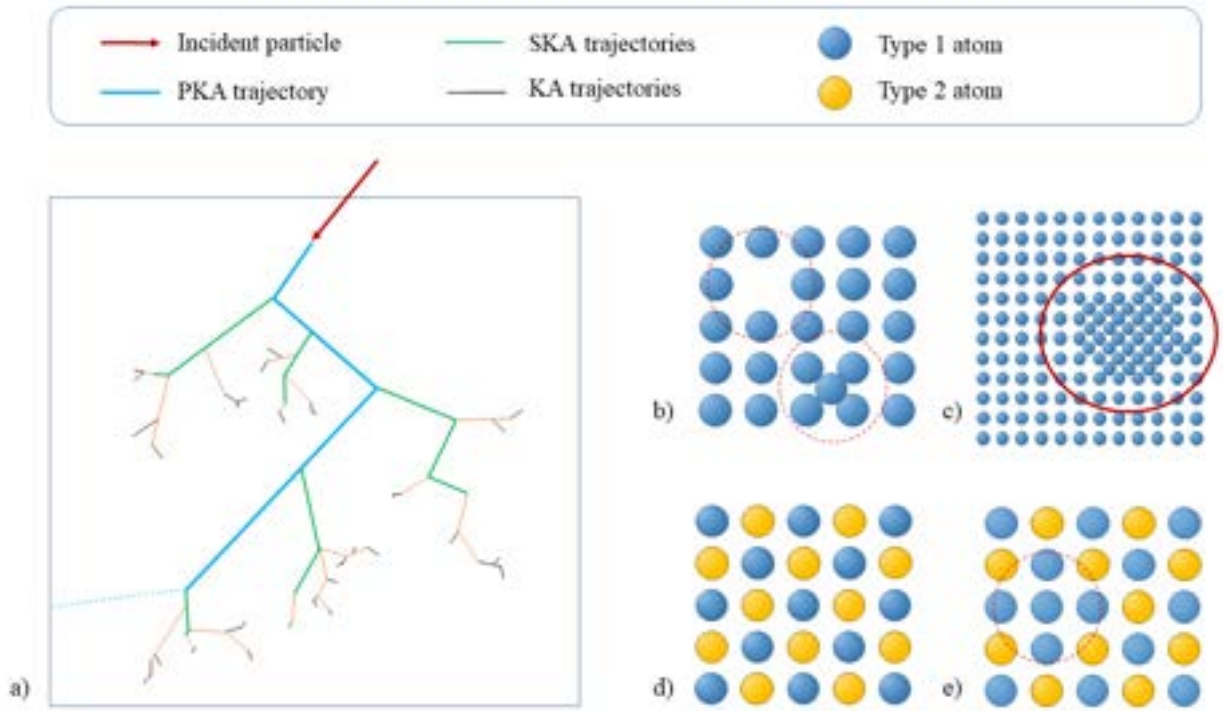


Figure 1.14: Schematic overview of a collision cascade and defects. With a) the topology of a collision cascade, b) a vacancy defect and an interstitial defect, c) interstitials cluster, d) a perfect crystalline structure of a binary compound, e) the same crystalline structure with an antisite defect.

Figure 1.14 schematically shows a collision cascade, vacancy defects, interstitial defects, antisite defects, and a cluster. The various defects previously mentioned disrupt the periodicity of the crystal, leading to localized energy states for electrons. These energy levels will be located between the valence band and the conduction band. When the energy level is created near one of the bands, it is possible for charge carriers to get trapped there, reducing their mobility. Energy levels created near the middle of the band gap can facilitate the recombination of charge carriers, thereby decreasing their concentration. Mid-band gap levels can also increase the concentration of charge carriers in the device through thermal generation.

1.4 State of the art: Gallium nitride

Since the beginning of this chapter, the interactions between particles and a target material have been explained. It would be impossible to gather in a single study all the effects of radiation on every material, and even though this thesis focuses on microelectronics, it would also be very difficult to encompass all semiconductors. That is why this section presents Gallium Nitride (GaN), a semiconductor that is gaining increasing interest.

1.4.1 Gallium Nitride

1.4.1.1 History of gallium nitride

For over fifteen years, GaN has been at the center of numerous research projects in electronics and optoelectronics, yet its early studies did not initially extend to this field.

In 1938, to study the crystal and lattice structures of various materials, V.B. Juza and H. Hahn [20] synthesized gallium nitride for the first time. They produced a powder composed of small needles and flakes of GaN by passing ammonia over liquid gallium, all heated to 1200°C. Twenty years later, to measure the photoluminescence spectrum of GaN, Grimmeiss *et al.* [21] used the same technique as Juza *et al.* to produce small GaN crystals. It was not until the late 1960s that a technique called Hybrid Vapor Phase Epitaxy (HVPE) was developed by H.P. Marusaka and J.J. Tietjen [22] to produce GaN.

However, the produced layers were all n-type (excess charge carriers are electrons). Edward Miller, Jacques Pankove, and Herbert Maruska attempted to produce p-doped GaN, and during their work, they created the first p-doped GaN LEDs, including the magnesium-doped violet LED created by Maruska, see Figure 1.15.

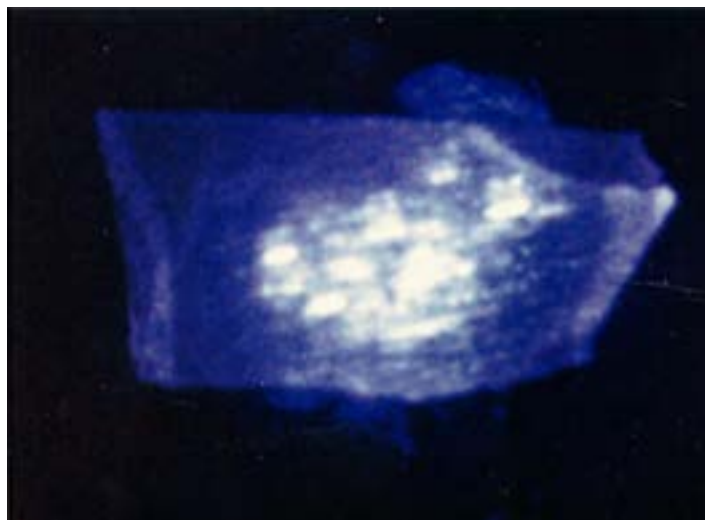


Figure 1.15: GaN blue LED - 1972 [23].

In the early 1990s, p-doped GaN was successfully obtained through the work of Isamu Akasaki, Shuji Nakamura, and Hiroshi Amano. During research on zinc-doped gallium nitride, Amano discovered by chance that when a GaN sample was irradiated by a low-energy electron beam, the luminescence of the doped compound increased[24], but even after this treatment, the GaN was still not p-type conductive. Amano then had the idea to change the dopant from zinc to magnesium, as the latter was more effective for activating acceptors. After low-energy electron beam treatment of GaN samples, some of them exhibited p-type conductivity. The first p-type GaN sample was created. Amano *et al.*'s work on InGaN for blue LEDs was awarded the 2014 Nobel Prize in Physics[25].

Since this discovery, research on gallium nitride has gained momentum, particularly with the development of optoelectronics and electronics. The first gallium nitride transistors date back to the early 1990s with the research of A. Khan *et al.* on GaN Metal-Semiconductor Field-Effect Transistor (MESFET)[26] and GaN/AlGaN HEMT[27, 28].

In 1999, Ambacher *et al.* described the properties of the 2 dimensions electron gas in an AlGaN/GaN heterostructure using a theoretical model and experiments. The understanding of HEMT operation then made significant progress. The same year, the high-power microwave potential of AlGaN/GaN high electron mobility transistors on a SiC substrate was demonstrated by Sheppard *et al.* [29].

A decade later, a significant milestone was reached with the commercialization of devices based on Gate Injection Transistor (GIT) technology, enabling the development of normally-off AlGaN/GaN HEMTs.

More recently, other studies have been pivotal in advancing the understanding of AlGaN/GaN HEMT. In 2012, Tripathy *et al.* epitaxially grew an AlGaN/GaN heterostructure on a 200 mm silicon substrate [30]. In 2013, Shinohara *et al.* highlighted the high-frequency performance of gallium nitride-based HEMTs. Finally, in the second half of the 2010s, several studies demonstrated the ability of GaN structures to withstand high voltages, among others [31–34].

Currently, GaN devices are commercially available, and several products have been offered in two main voltage ranges:

Low/medium voltage devices (less than 200 V) are used in applications such as micro-inverters for solar power, DC-DC power converters, motor control, wireless power transfer, robotics, pulsed power applications, and audio amplifiers.

High-voltage devices (up to 650 V) are used in applications such as telecommunication servers, industrial converters, photovoltaic inverters, servo motor control, lighting applications, power adapters, converters for consumer electronics, amplifiers, and data centers [35]. Currently, no ultra-high voltage (greater than 1 kV) GaN-based transistors are commercially available.

To highlight the interesting characteristics of GaN, one can compare these with the characteristics of the reference semiconductor which is Si.

- The band-gap is the energy gap between the valence band and the conduction band. More directly, it is the energy that an electron must acquire to pass from the valence band to the conduction one. It thus becomes a charge carrier and ensures the conductivity of the material. At equilibrium no electronic state is present in the band-gap. The band-gap size is a key parameter for semiconductor, at ambient temperature, in Si, it is 1.12 eV whereas in GaN it is 3.4 eV. band-gap is referred to as 'conventionnal' and is used as a reference, while that for GaN is referred as 'large'. Large band-gap also means a high energy barrier, which electrons have to overcome to participate to electric conductivity. This large band-gap allows the semiconductor to operate at high temperatures, and electrons are less subject to the problem associated with the thermal generation (see Section 1.3.3.6).
- The mobility of electrons is also a very important characteristic. It measures the response of electrons to an electric field within the material. Under the influence of the electric field, electrons, which previously exhibited random motion due to thermal agitation, acquire an average velocity in the direction of the field. In Si, this value is $1500 \text{ cm}^2/\text{V.s}$, while in GaN, it is $2000 \text{ cm}^2/\text{V.s}$. For example, the higher this value, the better the sensitivity of sensors. In transistors, high electron mobility leads to better high-frequency performance and faster switching times. Some factors can hinder mobility, such as thermal agitation, which slows down electrons, or crystalline defects (see Section 1.3.3.6).
- Thermal conductivity is a physical property that describes a material's ability to dissipate heat. More precisely, it is a measure of a material's potential to transfer heat from a hot region to a cold region. In devices such as power transistors, LEDs, and microprocessors, heat generation is inevitable due to energy losses. High thermal conductivity in the semiconductor material or substrate is crucial for efficiently dissipating this heat, thereby preventing overheating and failures. The value found by M. Meneghini *et al.* [36] for GaN is twice that of silicon, making it more suitable for use in high-temperature ranges. Other studies have concluded with a value lower than that of Si, making gallium nitride less effective in heat dissipation. However, other factors allow GaN to operate at lower temperatures than Si at the same voltage due to its efficiency [37]. Certain factors can degrade thermal conductivity, such as the dimensionality of the devices or temperature, since as the latter increases, conductivity decreases.
- The breakdown electric field is also a very important characteristic. It represents the maximum electric field that a material can withstand before creating an electrical arc and breaking down. Beyond this limit, the material becomes conductive, potentially

causing a short circuit. The higher this value, the more capable the material is of withstanding strong electric fields. For a semiconductor, an excessive field can excite electrons to the point where they cross the band gap, creating a large number of electron-hole pairs that amplify the current, leading to failure. This value for GaN is ten times higher than that of Si, making it attractive for high-voltage applications.

- Finally, an important property is the saturation velocity, which is the maximum speed that charge carriers (electrons or holes) can reach in a semiconductor material when subjected to a strong electric field. Beyond this speed, even if the electric field continues to increase, the speed of the charge carriers no longer increases significantly. The saturation velocity is crucial for high-frequency and high-power applications. Again, this characteristic is higher in GaN than in silicon. This high saturation velocity is a key parameter for power and high-frequency applications.

GaN exhibits interesting and more advantageous characteristics compared to other widely used semiconductors, particularly silicon. Its high charge carrier mobility and high electron saturation velocity allow GaN to be used at very high frequencies and in power applications. Its thermal conductivity, wide bandgap, and high breakdown electric field make it suitable for high-power and high-temperature applications.

Figure 1.16 provides a summary of the comparative characteristics between Si and GaN.

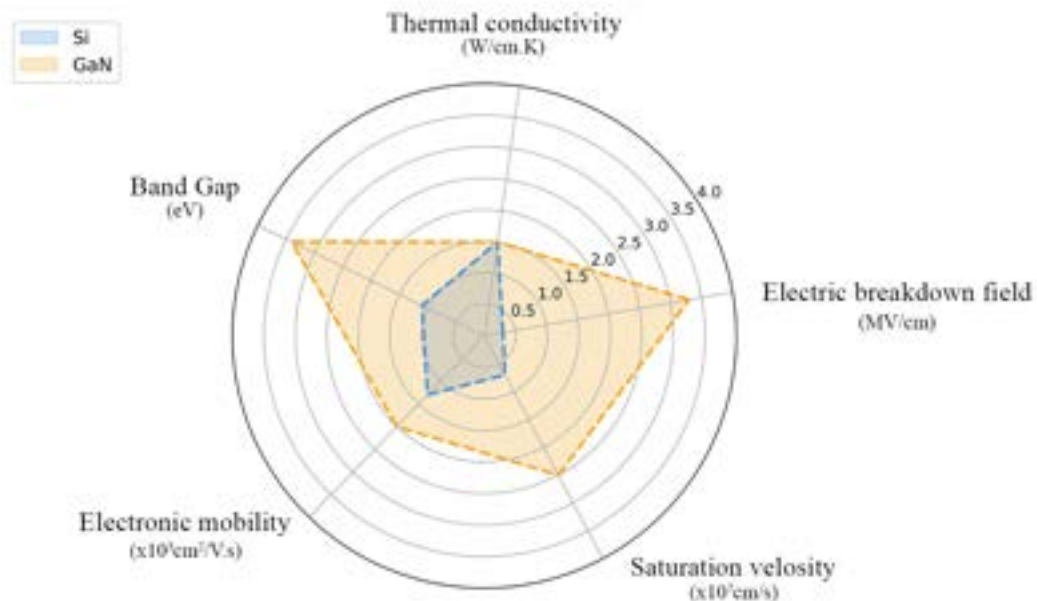


Figure 1.16: Comparative radar chart of the characteristics between Si and GaN.

1.4.1.2 GaN radiation resistance

Due to their advantageous characteristics and very high reliability, GaN-based devices are of interest for a wide range of applications in extreme conditions, such as space applications and those within nuclear environments. To justify the fact that gallium nitride is a viable option, its radiation hardness has been intensively studied in recent years but still needs to be clarified depending on the type of environments and effects. Previous studies on the radiation resistance of gallium nitride agree that it is a highly radiation-resistant material, as durable as SiC and more so than Gallium Arsenide (GaAs).

Indeed, studies have been conducted on the effect of neutron radiation in GaN and in the AlGaIn/GaN heterojunction [38–40]. Neutron irradiation produces two main effects: an increase in the threshold voltage and a decrease in the charge carrier mobility of the material. The variation in the threshold voltage is due to an increase in the concentration of acceptor states in the barrier layer, and this variation increases linearly with neutron fluence. The cause of the decrease in material mobility is also attributed to the acceptors in the barrier layer, which result in a local threshold voltage and variations in electron channel density.

In general, neutrons prove to be less damaging than protons, both in terms of 'ON-resistance' and changes in the breakdown field [41, 42], but they appear to cause more extensive damage rather than the creation of point defects.

Once again, GaN is more resistant than GaAs, particularly to proton radiation[43][44], which is highly prevalent in the space environment. Proton irradiation can cause a wide range of effects in GaN-based devices, mainly related to the creation of defects caused by the interaction between the crystal lattice particles and energetic protons. The increase in defect concentration leads to a decrease in the concentration and mobility of charge carriers in the material, due to charge diffusion and trapping at defect sites.

The level of damage depends on the proton energy, and it turns out to be higher for lower proton energy[45]. This behavior might seem unexpected, but it is related to the greater non-ionizing energy loss of lower-energy particles in the barrier and channel region, whereas higher-energy protons cause damage deeper within the device structure[46]. Regarding the number of irradiated protons, a typical threshold value for device performance variation is a fluence of $10^{13} \text{ p}^+/\text{cm}^2$ at 1.8 MeV [47, 48], and $5 \times 10^9 \text{ p}^+/\text{cm}^2$ at 40 MeV [49]. The lower threshold fluence at a higher energy is unexpected and may be related to different device structures and quality in the various studies. The specific defects created by proton irradiation include deep donor and acceptor levels. Most of the degradation caused by proton irradiation is related to displacement damage and can be mitigated by high-temperature annealing [50].

For electron irradiation, the main effect is to cause a negative shift in the threshold voltage at low fluence, which becomes positive at higher fluence, due to the generation of traps with different charge states. Additionally, a decrease in channel mobility has been

reported [42].

For ions, the damage consists of vacancies, interstitial atoms, and extended defects such as dislocations and stacking faults. The crystalline structure of GaN is highly resistant to ion bombardment due to the strong ionicity of the Ga-N bond. Very large doses are required for amorphization, and the amorphization threshold is much higher than in other semiconductors [51]. Structural defects can be easily created with moderate implantation doses and can lead to lattice expansion, damaging the characteristics of GaN.

The effects induced by gamma rays include an increase in on-state resistance, a negative shift in threshold voltage, an increase in saturation current, a decrease in gate current, and an increase in breakdown voltage [52]. However, once again, studies show a trend towards greater resistance of GaN devices to radiation [53, 54]

1.5 Conclusion

This first chapter provides an overview of the context surrounding the work of this thesis. Various radiation environments are initially presented, along with the particles that compose them. In space, high energy levels are reached, whether from galactic cosmic rays or particles generated during solar events. Protons, which are present in all radiation environments, can cause several degradation effects on electronic components, as discussed in Section 1.3. This section also covers the effects of various particle interactions with materials, and delves into basic microelectronics with a description of the functioning of Metal-Oxide-Semiconductor Field-Effect Transistors (MOSFETs), Complementary Metal-Oxide Semiconductors (CMOS), and High-Electron-Mobility Transistors (HEMTs). Additionally, it introduces the four key radiation effects: dose rate, single event effects (SEE), ionizing dose, and non-ionizing dose. And finally, a retrospective on the history of GaN and the state of the art regarding radiation effects on this semiconductor is presented in Section 1.4.

Although many experimental studies of the effects of radiation on gallium nitride have been achieved over the last decade, most numerical simulations have been suggest that GaN is relatively resistant to radiation. However, much of this research dates back to the early 2000s, using the computational resources available at that time. In contrast, this work leverages modern computational power along with a robust foundation of previous studies to conduct a comprehensive numerical simulation on the radiation resistance of GaN. To achieve this, we will employ classical molecular dynamics and ab initio methods, combined with large-scale statistical analysis involving a very large number of simulations. This approach will contribute significantly to advancing knowledge in this field.

Bibliography

- [1] Howard H. Seliger. Wilhelm Conrad Röntgen and the Glimmer of Light. *Physics Today*, 48(11):25–31, 11 1995. ISSN 0031-9228. doi: 10.1063/1.881456. URL <https://doi.org/10.1063/1.881456>.
- [2] Victor Hess. On the observations of the penetrating radiation during seven balloon flights, 2018. URL <https://arxiv.org/abs/1808.02927>.
- [3] J.L. Barth, C.S. Dyer, and E.G. Stassinopoulos. Space, atmospheric, and terrestrial radiation environments. *IEEE Transactions on Nuclear Science*, 50(3):466–482, 2003. doi: 10.1109/TNS.2003.813131.
- [4] Measurement and reporting of alpha particles and terrestrial cosmic ray-induced soft errors in semiconductor devices: Jesd89a. *JEDEC STANDARD, JEDEC Solid State Technology Association*, 89:1–85, 2006.
- [5] Michael Tice. Palaeontology: Modern life in ancient mats. *Nature*, 452:40–1, 04 2008. doi: 10.1038/452040a.
- [6] Albert Einstein. Über einen die erzeugung und verwandlung des lichtes betreffenden heuristischen gesichtspunkt, 1905.
- [7] R.H. Pratt, L.A. LaJohn, V. Florescu, T. Surić, B.K. Chatterjee, and S.C. Roy. Compton scattering revisited. *Radiation Physics and Chemistry*, 79(2):124–131, 2010. ISSN 0969-806X. doi: <https://doi.org/10.1016/j.radphyschem.2009.04.035>. URL <https://www.sciencedirect.com/science/article/pii/S0969806X09003491>. Special Issue on Future Directions in Atomic and Condensed Matter Research and Applications.
- [8] Aymeric Van Lauwe and Frédéric Marie. irfu.cea.fr, 2017. URL https://irfu.cea.fr/Phoce/Vie_des_labos/Ast/ast_visu.php?id_ast=2826. Accessed on August 8, 2024.
- [9] Giuseppe Maino and Enzo Menapace. Nuclear photoreactions in the context of a nuclear data review for radiation shielding in advanced technology applications. *Journal of Nuclear Science and Technology*, 39(sup2):1349–1352, 2002.
- [10] Leslie L. Foldy. Neutron-electron interaction. *Rev. Mod. Phys.*, 30:471–481, Apr 1958. doi: 10.1103/RevModPhys.30.471. URL <https://link.aps.org/doi/10.1103/RevModPhys.30.471>.
- [11] A Paccagnella and S Gerardin. Basics of radiation effects in electronic devices. *RADECS short course*, 2009.
- [12] Robert C Baumann. Radiation-induced soft errors in advanced semiconductor technologies. *IEEE Transactions on Device and materials reliability*, 5(3):305–316, 2005.

- [13] Jingtian Fang, Mahmud Reaz, Stephanie L. Weeden-Wright, Ronald D. Schrimpf, Robert A. Reed, Robert A. Weller, Massimo V. Fischetti, and Sokrates T. Pantelides. Understanding the average electron–hole pair-creation energy in silicon and germanium based on full-band monte carlo simulations. *IEEE Transactions on Nuclear Science*, 66(1):444–451, 2019. doi: 10.1109/TNS.2018.2879593.
- [14] Thomas Jarrin. *Modelisation des effets de déplacements atomiques induits par irradiation dans les matériaux pour la microelectronique*. PhD thesis, Toulouse 3, 2021.
- [15] T.R. Oldham and F.B. McLean. Total ionizing dose effects in mos oxides and devices. *IEEE Transactions on Nuclear Science*, 50(3):483–499, 2003. doi: 10.1109/TNS.2003.812927.
- [16] H. J. Barnaby. Total-ionizing-dose effects in modern cmos technologies. *IEEE Transactions on Nuclear Science*, 53(6):3103–3121, 2006. doi: 10.1109/TNS.2006.885952.
- [17] M.J. Boschini, P.G. Rancoita, and M. Tacconi. Sr-niel–7 calculator: Screened relativistic (sr) treatment for niel dose, nuclear and electronic stopping power calculator (version 10.16), 2014. URL <https://www.sr-niel.org/>. Accessed on August, 2024.
- [18] GC Messenger, EJ Steele, and M Neustadt. Displacement damage in mos transistors. *IEEE Transactions on Nuclear Science*, 12(5):78–82, 1965.
- [19] Pengfei Wan, Jianqun Yang, Hao Jiang, Yuanting Huang, Ling Lv, Lei Dong, Xiaoqing Yue, Bin Zhang, Gang Lin, Guojian Shao, et al. The effect of ionization damage on displacement damage in algan/gan hemts. *IEEE Transactions on Nuclear Science*, 69(10):2129–2135, 2022.
- [20] H.Hahn VB.Juza. Über die kristallstrukturen von cu_3n , gan und inn metallarnide und metallnitride. *Zeischrift fiir anorgankche und allgemeine Chemie*, 239:282–287, 1938.
- [21] Z.H-Koelmans H.Grimmeiss. Effects of secondary particles on the total dose and the displacement damage in space proton environments. *Nature*, 14a:264, 1959.
- [22] J.J.Tietjen H.P.Maruska. The preparation and properties of vapor-deposited single-crystal-line gan. *Appl.Phys.Lett*, 15(10):327, 1969.
- [23] Herbert Paul Maruska and Walden Clark Rhines. A modern perspective on the history of semiconductor nitride blue light sources. *Solid-State Electronics*, 111:32–41, 2015. ISSN 0038-1101. doi: <https://doi.org/10.1016/j.sse.2015.04.010>. URL <https://www.sciencedirect.com/science/article/pii/S0038110115001318>.
- [24] Takahiro Kozawa Kazumasa Hiramatsu Nobuhiko Sawaki Kousuke Ikeda Hiroshi Amano, Isamu Akasaki and Yoshikazu Ishii. Electron beam effects on blue luminescence of zinc-doped gan. *Journal of Luminescence*, 40 and 41:121–122, 1988.
- [25] Hiroshi Amano. Nobel lecture: Growth of gan on sapphire via low-temperature deposited buffer layer and realization of *p*-type gan by mg doping followed by low-energy electron beam irradiation. *Rev. Mod. Phys.*, 87:1133–1138, Oct 2015.

- [26] M. Asif Khan, J. N. Kuznia, A. R. Bhattarai, and D. T. Olson. Metal semiconductor field effect transistor based on single crystal gan. *Applied Physics Letters*, 62(15):1786–1787, 1993. doi: 10.1063/1.109549.
- [27] M. Asif Khan, A. Bhattarai, J. N. Kuznia, and D. T. Olson. High electron mobility transistor based on a gan-alxga1-xn heterojunction. *Applied Physics Letters*, 63(9): 1214–1215, 1993. doi: 10.1063/1.109775.
- [28] M. Asif Khan, J. N. Kuznia, D. T. Olson, W. J. Schaff, J. W. Burm, and M. S. Shur. Microwave performance of a 0.25 micrometers gate algan/gan heterostructure field effect transistor. *Applied Physics Letters*, 65(9):1121–1123, 1994. doi: 10.1063/1.112116.
- [29] S.T. Sheppard, K. Doverspike, W.L. Pribble, S.T. Allen, J.W. Palmour, L.T. Kehias, and T.J. Jenkins. High-power microwave gan/algan hemts on semi-insulating silicon carbide substrates. *IEEE Electron Device Letters*, 20(4):161–163, 1999. doi: 10.1109/55.753753.
- [30] S. Tripathy, Vivian K. X. Lin, S. B. Dolmanan, Joyce P. Y. Tan, R. S. Kajen, L. K. Bera, S. L. Teo, M. Krishna Kumar, S. Arulkumaran, G. I. Ng, S. Vicknesh, Shane Todd, W. Z. Wang, G. Q. Lo, H. Li, D. Lee, and S. Han. Algan/gan two-dimensional-electron gas heterostructures on 200mm diameter si(111). *Applied Physics Letters*, 101(8):082110, 2012. doi: 10.1063/1.4746751. URL <https://doi.org/10.1063/1.4746751>.
- [31] Toshihide Kikkawa, Tsutomu Hosoda, Ken Shono, Kenji Imanishi, Yoshimori Asai, YiFeng Wu, Likun Shen, Kurt Smith, Dixie Dunn, Saurabh Chowdhury, Peter Smith, John Gritters, Lee McCarthy, Ronald Barr, Rakesh Lal, Umesh Mishra, and Primit Parikh. Commercialization and reliability of 600 v gan power switches. In *2015 IEEE International Reliability Physics Symposium*, pages 6C.1.1–6C.1.6, 2015. doi: 10.1109/IRPS.2015.7112766.
- [32] Saichiro Kaneko, Masayuki Kuroda, Manabu Yanagihara, Ayanori Ikoshi, Hideyuki Okita, Tatsuo Morita, Kenichiro Tanaka, Masahiro Hikita, Yasuhiro Uemoto, Satoru Takahashi, and Tetsuzo Ueda. Current-collapse-free operations up to 850 v by gan-git utilizing hole injection from drain. In *2015 IEEE 27th International Symposium on Power Semiconductor Devices IC's (ISPSD)*, pages 41–44, 2015. doi: 10.1109/ISPSD.2015.7123384.
- [33] Kenichiro Tanaka, Tatsuo Morita, Hidekazu Umeda, Saichiro Kaneko, Masayuki Kuroda, Ayanori Ikoshi, Hiroto Yamagiwa, Hideyuki Okita, Masahiro Hikita, Manabu Yanagihara, Yasuhiro Uemoto, Satoru Takahashi, Hiroaki Ueno, Hidetoshi Ishida, Masahiro Ishida, and Tetsuzo Ueda. Suppression of current collapse by hole injection from drain in a normally-off gan-based hybrid-drain-embedded gate injection transistor. *Applied Physics Letters*, 107(16):163502, 2015. doi: 10.1063/1.4934184. URL <https://doi.org/10.1063/1.4934184>.
- [34] Kenichiro Tanaka, Tatsuo Morita, Masahiro Ishida, Tsuguyasu Hatsuda, Tetsuzo Ueda, Kazuki Yokoyama, Ayanori Ikoshi, Masahiro Hikita, Masahiro Toki, Manabu

- Yanagihara, and Yasuhiro Uemoto. Reliability of hybrid-drain-embedded gate injection transistor. In *2017 IEEE International Reliability Physics Symposium (IRPS)*, pages 4B–2.1–4B–2.10, 2017. doi: 10.1109/IRPS.2017.7936308.
- [35] 600V CoolGaN enhancement-mode Power Transistor Infineon. 600v coolgan™ enhancement-mode power transistor, 2021.
- [36] Christian Mion. *Investigation of the thermal properties of gallium nitride using the three omega technique*. North Carolina State University, 2005.
- [37] M. Leszczynski, T. Suski, H. Teisseyre, P. Perlin, I. Grzegory, J. Jun, S. Porowski, and T. D. Moustakas. Thermal expansion of gallium nitride. *Journal of Applied Physics*, 76(8):4909–4911, 1994. doi: 10.1063/1.357273. URL <https://doi.org/10.1063/1.357273>.
- [38] K.-X. Sun, H. Valencia, L. Soriano, and R. O. Nelson. Neutron radiation hardness of aluminum gallium nitride uv leds at various wavelengths. *Review of Scientific Instruments*, 92(4):043501, 2021. doi: 10.1063/5.0043852. URL <https://doi.org/10.1063/5.0043852>.
- [39] K.-X. Sun, M. Valles, H. Valencia, and R.O. Nelson. Gallium nitride (gan) devices as a platform technology for radiation hard inertial confinement fusion diagnostics. *Review of Scientific Instruments*, 89(10):10K113, 2018. doi: 10.1063/1.5039407. URL <https://doi.org/10.1063/1.5039407>.
- [40] Luis Soriano, Hector Valencia, Ke-Xun Sun, and Ronald Nelson. Fast neutron irradiation effects on multiple gallium nitride (gan) device reliability in presence of ambient variations. In *2020 IEEE International Reliability Physics Symposium (IRPS)*, pages 1–6, 2020. doi: 10.1109/IRPS45951.2020.9129517.
- [41] M. P. King, A. M. Armstrong, J. R. Dickerson, G. Vizkelethy, R. M. Fleming, J. Campbell, W. R. Wampler, I. C. Kizilyalli, D. P. Bour, O. Aktas, H. Nie, D. Disney, J. Wierer, A. A. Allerman, M. W. Moseley, F. Leonard, A. A. Talin, and R. J. Kaplar. Performance and breakdown characteristics of irradiated vertical power gan p-i-n diodes. *IEEE Transactions on Nuclear Science*, 62(6):2912–2918, 2015. doi: 10.1109/TNS.2015.2480071.
- [42] S. J. Pearton, F. Ren, Erin Patrick, M. E. Law, and Alexander Y. Polyakov. Review—ionizing radiation damage effects on gan devices. *ECS Journal of Solid State Science and Technology*, 5(2):Q35, nov 2015. doi: 10.1149/2.0251602jss. URL <https://dx.doi.org/10.1149/2.0251602jss>.
- [43] S.M. Khanna, J. Webb, H. Tang, A.J. Houdayer, and C. Carlone. 2 mev proton radiation damage studies of gallium nitride films through low temperature photoluminescence spectroscopy measurements. *IEEE Transactions on Nuclear Science*, 47(6):2322–2328, 2000. doi: 10.1109/23.903772.
- [44] V.M. Ayres, B.W. Jacobs, M.E. Englund, E.H. Carey, M.A. Crimp, R.M. Ronningen, A.F. Zeller, J.B. Halpern, M.-Q. He, G.L. Harris, D. Liu, H.C. Shaw, and M.P. Petkov.

- Investigations of heavy ion irradiation of gallium nitride nanowires and nanocircuits. *Diamond and Related Materials*, 15(4):1117–1121, 2006. ISSN 0925-9635. doi: <https://doi.org/10.1016/j.diamond.2005.11.055>. URL <https://www.sciencedirect.com/science/article/pii/S0925963505005923>. Diamond 2005.
- [45] A.P. Karmarkar, B.D. White, D. Buttari, D.M. Fleetwood, R.D. Schrimpf, R.A. Weller, L.J. Brillson, and U.K. Mishra. Proton-induced damage in gallium nitride-based schottky diodes. *IEEE Transactions on Nuclear Science*, 52(6):2239–2244, 2005. doi: 10.1109/TNS.2005.860668.
- [46] C.H. Zhang, Y. Song, Y.M. Sun, H. Chen, Y.T. Yang, L.H. Zhou, and Y.F. Jin. Damage accumulation in gallium nitride irradiated with various energetic heavy ions. *Nuclear Instruments and Methods in Physics Research Section B: Beam Interactions with Materials and Atoms*, 256(1):199–206, 2007. ISSN 0168-583X. doi: <https://doi.org/10.1016/j.nimb.2006.12.003>. URL <https://www.sciencedirect.com/science/article/pii/S0168583X06012298>. Atomic Collisions in Solids.
- [47] Xinwen Hu, A.P. Karmarkar, Bongim Jun, D.M. Fleetwood, R.D. Schrimpf, R.D. Geil, R.A. Weller, B.D. White, M. Bataiev, L.J. Brillson, and U.K. Mishra. Proton-irradiation effects on algan/aln/gan high electron mobility transistors. *IEEE Transactions on Nuclear Science*, 50(6):1791–1796, 2003. doi: 10.1109/TNS.2003.820792.
- [48] A.P. Karmarkar, Bongim Jun, D.M. Fleetwood, R.D. Schrimpf, R.A. Weller, B.D. White, L.J. Brillson, and U.K. Mishra. Proton irradiation effects on gan-based high electron-mobility transistors with si-doped al/sub x/ga/sub 1-x/n and thick gan cap layers. *IEEE Transactions on Nuclear Science*, 51(6):3801–3806, 2004. doi: 10.1109/TNS.2004.839199.
- [49] B. Luo, J. W. Johnson, F. Ren, K. K. Allums, C. R. Abernathy, S. J. Pearton, R. Dwivedi, T. N. Fogarty, R. Wilkins, A. M. Dabiran, A. M. Wowchack, C. J. Polley, P. P. Chow, and A. G. Baca. dc and rf performance of proton-irradiated algan/gan high electron mobility transistors. *Applied Physics Letters*, 79(14):2196–2198, 2001. doi: 10.1063/1.1408606. URL <https://doi.org/10.1063/1.1408606>.
- [50] J.W. Ren F. Luo, B. Johnson. High-energy proton irradiation effects on algan/gan high-electron mobility transistors. *J. Electron. Mater.*, 31:437–441, 2002. doi: <https://doi.org/10.1007/s11664-002-0097-4>.
- [51] C Ronning, E.P Carlson, and R.F Davis. Ion implantation into gallium nitride. *Physics Reports*, 351(5):349–385, 2001. ISSN 0370-1573. doi: [https://doi.org/10.1016/S0370-1573\(00\)00142-3](https://doi.org/10.1016/S0370-1573(00)00142-3). URL <https://www.sciencedirect.com/science/article/pii/S0370157300001423>.
- [52] A.M. Kurakin. Effect of gamma radiation on the characteristics of gallium nitride hemt heterostructures. *Tech. Phys.*, 29:748–749, 2003. ISSN 0370-1573. doi: <https://doi.org/10.1134/1.1615553>.

- [53] Jinghui Wang, Padhraic Mulligan, Leonard Brillson, and Lei R. Cao. Review of using gallium nitride for ionizing radiation detection. *Applied Physics Reviews*, 2(3):031102, 2015. doi: 10.1063/1.4929913. URL <https://doi.org/10.1063/1.4929913>.
- [54] O. Aktas, A. Kuliev, V. Kumar, R. Schwindt, S. Toshkov, D. Costescu, J. Stubbins, and I. Adesida. 60co gamma radiation effects on dc, rf, and pulsed i-v characteristics of algan/gan hemts. *Solid-State Electronics*, 48(3):471–475, 2004. ISSN 0038-1101. doi: <https://doi.org/10.1016/j.sse.2003.08.003>. URL <https://www.sciencedirect.com/science/article/pii/S0038110103003344>.

Chapter 2:

Simulation Methodology

Contents

2.1	Introduction	49
2.2	Multi-model numerical simulation approach	50
2.3	Monte-Carlo	52
2.3.1	Binary Collision Approximation	53
2.3.2	SRIM & TRIM	57
2.3.3	The case of Displacement Damage	59
2.4	Molecular Dynamics	59
2.4.1	Generalities	59
2.4.2	Integration algorithms	60
2.4.2.1	Position-Verlet	60
2.4.2.2	Velocity-Verlet	61
2.4.2.3	Thermodynamical conditions	61
2.4.3	The Case of Displacement Damage	62
2.4.3.1	Timestep	62
2.4.3.2	Interatomic potentials	63
2.4.3.3	Tersoff/ZBL potential	63
2.4.4	Available tool	67
2.4.5	Advantages and limitations	67
2.4.6	Threshold Displacement Energy	67
2.5	<i>Ab initio</i> Methods	71
2.5.1	<i>Ab initio</i> Molecular Dynamics	71
2.5.2	Density Functional Theory	71
2.5.2.1	Schrödinger equation, Born-Oppenheimer and electron density	71
2.5.2.2	Hohenberg-Kohn theorems	74

2.5.2.3	Kohn and Sham equations	75
2.5.2.4	DFT cycle	75
2.5.2.5	Approximations	77
2.5.2.6	Plane wave formalism	77
2.5.2.7	Advantages and limitations	78
2.5.2.8	Available tools	78
2.5.2.9	The case of Threshold Displacement Energy	78
2.6	Conclusion	81

2.1 Introduction

This work is centered on the use of numerical simulation tools within a multi-model framework. A key aspect of this approach involves as much as possible comparing our simulation results with experimental data available in the literature. However, the experimental characterization of the dynamics of collision cascades remains difficult as it requires a direct observation of atomistic events with sufficient temporal and spatial precision. In addition, these experiments often necessitate specialized techniques and infrastructures.

Indeed, numerical simulations not only overcome the practical challenges associated with experimental observation but also provide a detailed atomistic description of the physical mechanisms at play, allowing precise control over the parameters influencing these events. Beyond the inherent constraints linked to the description of a dynamic system at the atomic scale, the wide range of time scales characterizing each stage of the cascades complicates their full description. Numerical simulations address this challenge by enabling the exploration of dynamic phenomena occurring on extremely short time scales. In particular, the multi-model approach stands out as a powerful method by combining complementary models to analyze the various stages of displacement damage at appropriately matched spatial and temporal scales. This approach offers a comprehensive and coherent view of the phenomenon.

This chapter introduces the multi-model numerical simulation approach used in this study. First, the different simulation methods are presented, following the successive stages of the displacement damage process. For each method, the advantages, limitations, and available tools are discussed, with particular attention to their application in our work.

2.2 Multi-model numerical simulation approach

The multi-model numerical simulation approach developed in this study aims to describe all stages involved in displacement damage, from the interaction between the incident particle to the electronic characterization of defects. Initially conceptualized by Srour and Palko in 2013 [1], and detailed later by Raine *et al.* [2], this approach integrates four distinct numerical simulation methods. These methods, although used independently, complement one another, with output files from one simulation method often serving as input or supplement for another. Unlike conventional methods that optimize each stage independently, our approach systematically exploits the results from intermediate methods.

Our methodology captures phenomena across a wide range of temporal and spatial scales, from femtoseconds to minutes, and from atomic dimensions to macroscopic structures. By coherently integrating these scales, this interconnected workflow ensures that each method contributes to a coherent and comprehensive understanding of the studied phenomena. This collaborative use of diverse codes significantly enhances the overall precision and reliability of the results, offering a more robust and accurate simulation workflow. Figure 2.1 presents this approach isolating each stage of the event and associating it with a specific simulation method.

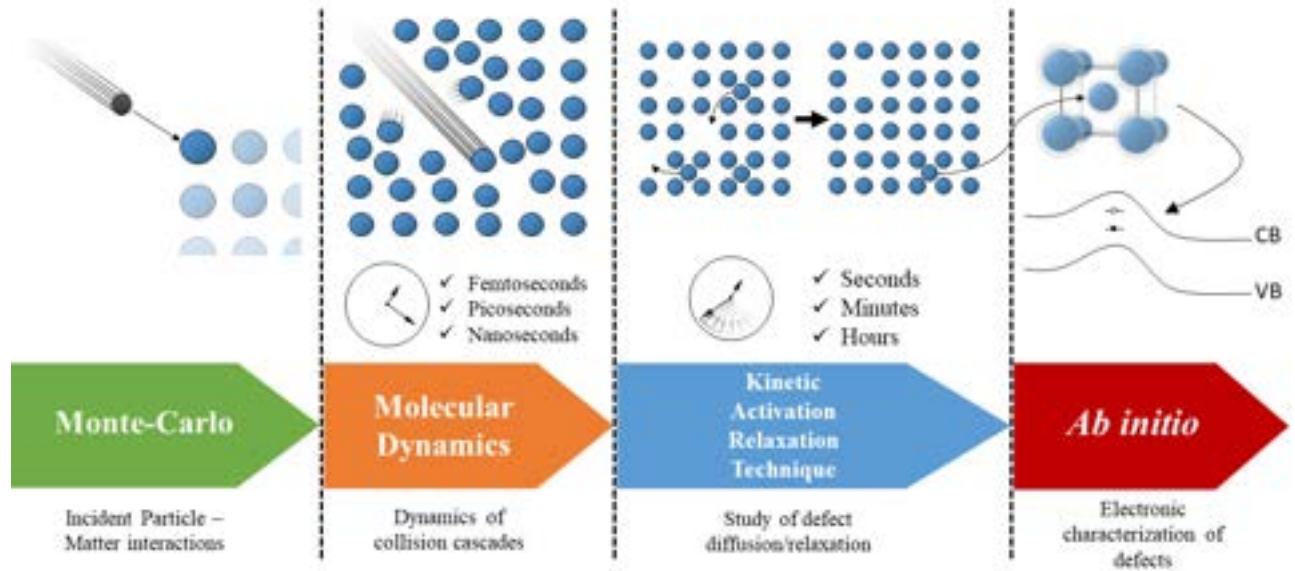


Figure 2.1: Schematic overview of the multi-model numerical simulation approach.

The initial interaction between the incident particle and the material is modeled using Monte-Carlo (MC) simulations, implemented in codes such as SRIM [3], IRADINA [4], and Geant4 [5]. While SRIM and IRADINA are primarily based on the Binary Collision

Approximation (BCA), Geant4 incorporates more comprehensive physical models, allowing for the simulation of both ion-matter and particle-matter interactions beyond the BCA. These simulations enable the rapid determination of important parameters such as the types and energy spectra of Primary Knock-On Atom (PKA) produced during the interaction. This information is critical, as it directly informs the initial conditions, i.e input, for subsequent Molecular Dynamics (MD) simulations.

MD simulations are then used to study the dynamic stages of the interaction, leveraging the PKA data derived from MC simulations. The atomic type is selected, and its energy is assigned as an initial condition for the MD simulations. Unlike MC simulations, MD provides detailed insights into the movement of the PKA and surrounding atoms over time. This results in a time-resolved representation of collision cascades, where the PKA initiates a chain of atomic collisions, leading to defect creation and clustering. The full atomic-scale description of MD allows to characterizing the geometry of the created defects. MD simulations are typically limited to timescales up to a few nanoseconds.

For processes occurring on longer timescales, such as defect diffusion and relaxation, Kinetic Activation-Relaxation technique (kART) simulations are utilized. By taking defect configurations identified in MD as inputs, kART enables the exploration of the diffusion of atoms on longer timescales ranging from seconds to minutes. This step provides a critical bridge between the atomic-scale dynamics captured by MD and the experimental observables.

Finally, once defect configurations stabilize over extended time scales, the defect positions output from kART are used as inputs for *ab initio* calculations, specifically using the Density Functional Theory (DFT). This method allows the electronic characterization of defects, such as the energy levels within the band gap that are compared to experimental results. This enables a direct connection between the defect structures formed during radiation damage and their electronic consequences, offering a comprehensive understanding of radiation-induced effects on semiconductor materials.

However, the use of the multi-model numerical simulation approach in this thesis differs slightly from the method used in [2]. While the classical purpose is to study each stage of the process with its corresponding simulation method, optimizing each step individually, our methodology incorporates multiple simulation methods to both study the different stages and validate results through cross-comparison with simulation methods, as represented in Figure 2.2. Specifically, the MC method is employed to gather information on particle-matter interactions. MC results, such as the number of defects and the penetration depth of PKA in the material, are compared with MD outcomes to ensure consistency. The MD method is then used to study the dynamics of collision cascades and the spatial characterization of defects and clusters. Subsequently, MD and DFT based *ab initio* method, are used to study the Threshold Displacement Energy (TDE) which is an important parameter to provide to the MC simulation. While MD simulations allow statistical analysis over a large number of simulations, DFT accounts for electronic interactions to achieve the highest level of precision.

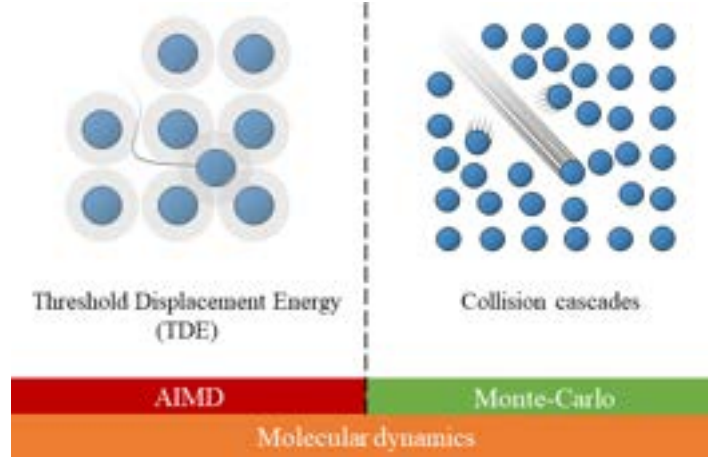


Figure 2.2: Schematic overview of the multi-model numerical simulation approach used in this work.

The combined use of MD and DFT to estimate threshold displacement energies (TDE) represents a significant advancement. This integration enables precise evaluation of TDE values by leveraging the statistical robustness of MD simulations alongside the detailed representation of electronic interactions provided by DFT. By accounting for both atomic-scale dynamics and complex electronic effects, this approach ensures high accuracy in determining a critical parameter for radiation damage analysis.

Together, these methods help estimating the material’s resistance to radiation within the studied energy and temperature ranges. The following sections focus on detailing the simulation methods employed and their role in our investigations, starting with MC simulations.

2.3 Monte-Carlo

The Monte Carlo (MC) calculation method [6, 7], first developed and applied in the 1940s during the Manhattan Project, is a powerful statistical method based on the use of random sampling to solve problems that may be deterministic in nature but are too complex for direct analytical solutions.

In the context of particle-matter interaction simulations, tools using the MC method model the stochastic nature of physical processes. Random sampling determines interaction types, scattering angles, energy transfer, and other outcomes based on physical cross-sections and interaction potentials. In the particle-matter interaction code Geant4, for each possible interaction mechanism, probabilities of occurrences are calculated based on the cross-sections of each of the mechanisms. One of the mechanism is then chosen by comparing its probability to a generated random number. Then, physical models adequate

to describe the chosen mechanism are applied. For Coulomb interactions between nuclei, i.e. atomic collisions, the BCA is used. The BCA is also fundamental to other MC codes like TRIM [3] and IRADINA [4], in which the only possible interaction is the atomic collision. In those MC codes, random number generators are thus not employed to choose an interaction mechanism. In the following, the BCA in the context of TRIM and IRADINA is detailed, as well as the TRIM interface.

2.3.1 Binary Collision Approximation

The references [8–10] show that BCA is based on the principle that, as a particle travels through a material or interacts with other particles, its trajectory and energy are primarily influenced by successive collisions with individual atoms in this environment. These collisions are modeled as interactions between the incident particle and a single target atom at each step, ignoring collective or multiple interactions involving multiple particles simultaneously. Between collisions, the particles are assumed to move without experiencing any force, following linear trajectories. Below, we review the basic equations of BCA. It is important to note that here we only treat the case of a projectile colliding with an atom initially at rest.

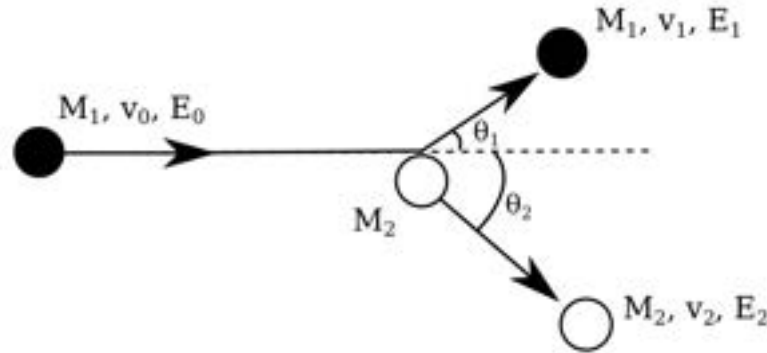


Figure 2.3: Schematic representation of the scenario modeled by the BCA in the laboratory system. The projectile atom is illustrated by the black circle, while the target atom is represented by the white circle [11].

A projectile of mass M_1 and velocity \vec{v}_0 (corresponding to energy E_0) is heading towards a target atom initially at rest of mass M_2 . After the collision, the projectile velocity is \vec{v}_1 (energy E_1), and the velocity of the target atom is \vec{v}_2 (energy E_2). The projectile is deflected by an angle θ_1 , and the target atom now moves along the direction characterized by θ_2 . During this collision, an amount of energy Q is lost to inelastic electronic excitations. Since Q is very small compared to E_0 , E_1 , or E_2 , the collision is said to be quasi-elastic. Moreover, the energy loss Q is considered to be entirely internal. The conservation of energy applied to the situation gives:

$$E_0 = E_1 + E_2 + Q \quad (2.1)$$

or equivalently,

$$\frac{1}{2}M_1v_0^2 = \frac{1}{2}M_1v_1^2 + \frac{1}{2}M_2v_2^2 + Q \quad (2.2)$$

The conservation of momentum gives:

$$M_1v_1 \cos(\theta_1) + M_2v_2 \cos(\theta_2) = M_1v_0 \quad (2.3)$$

$$M_1v_1 \sin(\theta_1) + M_2v_2 \sin(\theta_2) = 0 \quad (2.4)$$

By combining 2.1, 2.2, 2.3 and 2.4, we obtain the following expressions for the scattering angles θ_1 and θ_2 :

$$\begin{aligned} \cos(\theta_1) &= \frac{1}{2} \sqrt{\frac{E_1}{E_0}} (1 + A) + \frac{1}{2} \sqrt{\frac{E_0}{E_1}} \left(1 - A \left(1 - \frac{Q}{E_0} \right) \right) \\ \cos(\theta_2) &= \frac{1}{2} \sqrt{\frac{E_2}{E_0}} \frac{1 + A}{\sqrt{A}} + \frac{1}{2} \sqrt{\frac{E_0}{E_2}} \frac{1}{\sqrt{A}} \frac{Q}{E_0} \end{aligned}$$

where $A = \frac{M_2}{M_1}$.

The above equations are valid for what is often called the “laboratory system,” i.e. for a fixed external observer of the collision. However, in order to go further in the derivation of the equations of the BCA, we also have to apply the energy and momentum conservation in the center-of-mass system.

In this system, the observer is no longer fixed in the laboratory but moves with the center of mass of the system constituted by the projectile and the target atom. Therefore, even if the target atom is initially at rest in the laboratory system, it has a velocity \vec{v}_2 in the center-of-mass system before the collision, as the center of mass is moving (because the projectile is moving).

The situation in the center-of-mass system is depicted in Figure 2.4. The angle $\bar{\theta}/2$ is defined as the angle between the direction perpendicular to \vec{v}_0 (or \vec{v}_1) and the segment connecting the position of the two atoms. The projectile has a velocity \vec{v}_1 (energy \bar{E}_1) before the collision and a velocity \vec{v}_1' (energy \bar{E}_1') after. The target atom has a velocity \vec{v}_2 (energy \bar{E}_2) before the collision and a velocity \vec{v}_2' (energy \bar{E}_2') after.

The velocities are correlated by the following relations, with \vec{v} being the velocity of the center of mass in the laboratory system:

$$\begin{cases} \vec{v}_1 = \vec{v}_0 - \vec{v} \\ \vec{v}_2 = -\vec{v} \end{cases} \quad (2.5)$$

In this system, energy and momentum conservation respectively give:

$$\bar{E}_1 + \bar{E}_2 = \bar{E}_1' + \bar{E}_2' + Q \quad (2.6)$$

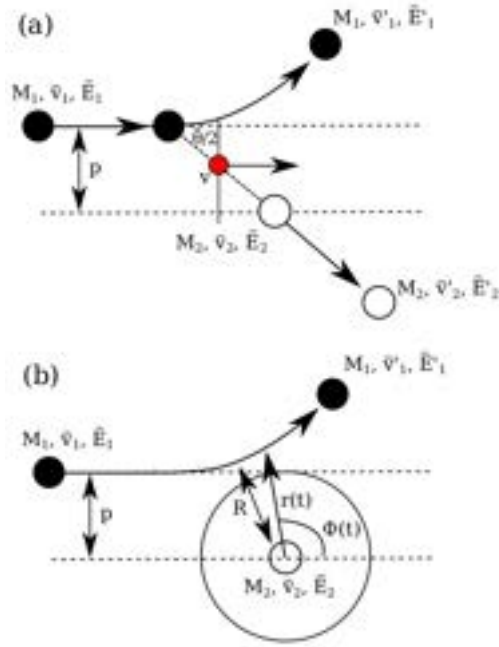


Figure 2.4: (a) Schematic view of the situation modeled by the BCA in the center-of-mass system. The projectile atom is depicted by the black circle and the target atom by the white circle. The smaller red circle represents the center-of-mass. In (b) are illustrated the polar coordinates (r, ϕ) used in the derivation of the BCA model. The signification of all the letters and symbols is given in the text [11].

or equivalently,

$$\frac{1}{2}M_1\vec{v}_1^2 + \frac{1}{2}M_2\vec{v}_2^2 = \frac{1}{2}M_1\vec{v}'_1^2 + \frac{1}{2}M_2\vec{v}'_2^2 + Q \quad (2.7)$$

and

$$M_1\vec{v}_1 + M_2\vec{v}_2 = M_1\vec{v}'_1 + M_2\vec{v}'_2 = 0. \quad (2.8)$$

It is then possible to obtain the energy $E_r = \bar{E}_1 + \bar{E}_2$ of the center-of-mass system from the above equations:

$$E_r = \frac{A}{1+A}E_0 \quad (2.9)$$

Going back to the laboratory system, one can write the energy of the projectile after the collision:

$$\frac{E_2}{E_0} = A \left(\frac{v_2}{v_0} \right)^2 = \left(\frac{A}{(1+A)^2} \right) \left(\cos(\theta_2) \pm \sqrt{f^2 - \sin(\theta_2)^2} \right)^2 \quad (2.10)$$

with $f^2 = 1 - \frac{(1+A)Q}{AE_0}$.

A similar expression, depending on θ_1 , can be obtained for the $\frac{E_1}{E_0}$ quantity [9]. Using 2.9 and 2.10, the maximum energy transferred (for $f = 1$) to the target atom T_{\max} can be written:

$$T_{\max} = \frac{4}{1+A} E_r. \quad (2.11)$$

Moreover, by using relations between the angles in the laboratory and center-of-mass system derived and given in [9], it is possible to define the ratio $\frac{E_2}{E_0}$ as a function of the center-of-mass scattering angle $\bar{\theta}$:

$$\frac{E_2}{E_0} = \frac{A}{(1+A)^2} \left((1-f^2) + 4f \sin^2 \left(\frac{\bar{\theta}}{2} \right) \right)^2 \quad (2.12)$$

Thus, the transferred energy T can be written, thanks to 2.11:

$$T = T_{\max} \left(f \sin^2 \left(\frac{\bar{\theta}}{2} \right) + \frac{1}{4} (1-f)^2 \right) \quad (2.13)$$

The energy transferred after each collision can be obtained following the calculation of the $\bar{\theta}$ angle. The objective of the following is thus to derive an expression for $\bar{\theta}$ which can be calculated.

The kinetic energy in the center-of-mass system is:

$$E_{\text{kin}} = \frac{1}{2} M_1 \bar{v}_1^2 + \frac{1}{2} M_2 \bar{v}_2^2 = \frac{1}{2} \frac{M_1 M_2}{M_1 + M_2} v_0^2 = E_r \quad (2.14)$$

If we write the term v_0^2 in the polar coordinates (r, ϕ) , depicted in 2.4, the energy conservation gives:

$$E_{\text{kin}} + E_{\text{pot}} = \frac{\mu}{2} \left(\dot{r}^2 + r^2 \dot{\phi}^2 \right) + V(r) = E_r \quad (2.15)$$

where $\mu = \frac{M_1 M_2}{M_1 + M_2}$ is the reduced mass, $V(r)$ the interaction interatomic potential, and dots above r and ϕ indicate differentiation with respect to time. The conservation of angular momentum gives:

$$r^2 \dot{\phi} = -v_0 p \quad (2.16)$$

with p the impact parameter, defined in Figure 2.4. Combining 2.15 and 2.16, we obtain \dot{r} :

$$\dot{r} = \pm v_0 \sqrt{1 - \frac{V(r)}{E_r} - \frac{p^2}{r^2}} \quad (2.17)$$

The minimum distance R between the two colliding atoms is given by:

$$g(R) = 0 \quad (2.18)$$

with

$$g(r) = \sqrt{1 - \frac{V(r)}{E_r} - \frac{p^2}{r^2}} \quad (2.19)$$

From 2.16 and 2.17 we can obtain $\frac{d\phi}{dr}$:

$$\frac{d\phi}{dr} = \frac{\dot{\phi}}{\dot{r}} = \pm \frac{p}{g(r)r^2} \quad (2.20)$$

Finally, from 2.20 and following symmetry considerations clearly exposed in [9], it is possible to derive an expression for the scattering angle $\bar{\theta}$:

$$\int_{\bar{\theta}}^{\pi} d\phi = 2p \int_R^{\infty} \frac{1}{r^2 g(r)} dr \quad (2.21)$$

which leads to:

$$\bar{\theta} = \pi - 2p \int_R^{\infty} \frac{1}{r^2 g(r)} dr \quad (2.22)$$

The final expression 2.22 constitutes the main equation of the BCA, from which the scattering angle can be calculated but also the energy transferred following 2.13.

In BCA, the MC component is used to model the stochastic interactions between the incident ion and target atoms. The initial positions of the latter are chosen probabilistically and the selection of collision targets and the incidence or deflection angles are statistically determined based on cross-sections. Finally, after each collision, the transferred energy and the new direction of the ion are randomly calculated while respecting conservation laws.

There are several MC simulation tools using BCA, such as GEANT4 [5], IRADINA [4] and SRIM [3]. The following section presents the latter, which was used for this work.

2.3.2 SRIM & TRIM

Stopping and Range of Ions in Matter (SRIM) is a software developed by James F. Ziegler and used to model the interaction of ions with matter [3]. Highly useful in studies of ion implantation, diffusion, and ion transport in solid materials, the first version of this software dates back to 1985 and has been widely used since, thanks to numerous updates.

With a straightforward interface, as shown in Figure 2.5, SRIM generates stopping power and range tables for ions. These tables are derived from a combination of theoretical models and experimental data, which enhances their reliability in predicting ion interactions with matter. The outputs include nuclear and electronic stopping power, the average number of defects created, and the average penetration depth in the material.

It is important to note that SRIM itself does not use the MC and BCA methods; this functionality is provided by its sub-program called Transport of Ions in Matter (TRIM). As outlined earlier, the stopping power tables accessible in the main SRIM interface are based on theoretical models. For instance, nuclear and electronic stopping powers are calculated



Figure 2.5: SRIM interface.

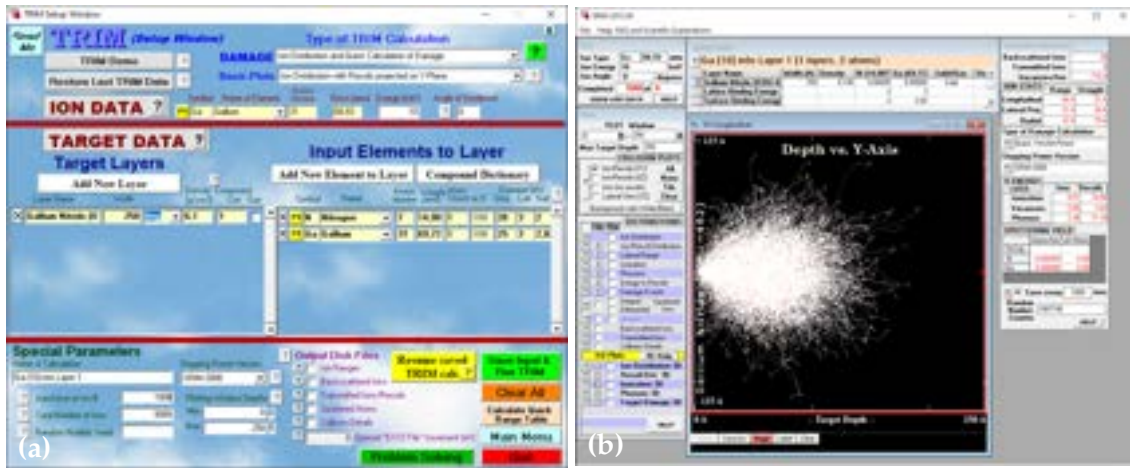


Figure 2.6: Transport of Ions in Matter (TRIM) interfaces.

using the Lindhard, Scharff, and Schiøtt (LSS) model and the Bethe-Bloch theory, respectively. Experimental data are also incorporated to refine these models, with additional values obtained through interpolation and extrapolation.

The TRIM sub-program, see Figure 2.6, uses the MC method to simulate ion interactions with matter. It enables the configuration of parameters such as material composition, thickness, displacement threshold energy, incident ion type, and energy. The simulations calculate various outcomes, including the number of defects, energy transfer during collisions, and phonon generation, providing detailed insights into ion-material interactions. However, one limitation is that TRIM functions as a black box, making it impossible to verify the underlying calculations. TRIM is not open source, which means that the underlying algorithms and assumptions used in the simulations are not fully accessible to users. This lack of transparency can make it difficult, or even impossible, to verify or

understand certain details of the calculations, such as the specific treatment of energy loss or the handling of edge cases in the models. As a result, users may face challenges when trying to validate or adapt the results to specialized scenarios.

2.3.3 The case of Displacement Damage

In the case of our study on displacement damage, MC method is used to examine the interaction between the radiation particle and the material. How much energy is transferred from the incident particle to the atoms of the material? What type of PKA is created? What is the average distance traveled by the PKA? These are questions that can be answered very quickly using the MC method. In addition to providing a lot of preliminary information, the results of these simulations also determine and influence the choice of input parameters for MD simulations.

Unfortunately, if we want to go further in the study of the behaviour of atoms during cascades, we need to change our simulation method. Indeed, many dynamic details are not taken into account. For instance, MC simulations often neglect time-dependent processes, such as the sequential evolution of particle trajectories or the detailed mechanisms of energy transfer over time. Instead, these methods rely on statistical sampling to approximate outcomes, which can oversimplify phenomena like movements, intermediate states, or transient effects like diffusion and relaxation. This simplification can lead to inaccuracies.

The next section presents the MD method used to go further and describe the ballistic phase of cascades.

2.4 Molecular Dynamics

Molecular dynamics (MD) is a numerical simulation method that allows tracking the movements of a set of particles, a molecule, or a more complex system over time. This method is based on classical mechanics and interatomic forces. To run the simulation, it only requires the positions of the particles, their initial velocities, and an interatomic potential as input. The practical implementation is detailed in the following.

2.4.1 Generalities

MD simulation method is discretized over time and based on classical mechanics, specifically on solving at each timestep of duration Δt the Newton's equation of motion for each atom i in the simulation box:

$$\vec{F}_i(t) = m_i \frac{d\vec{v}_i(t)}{dt} = m_i \frac{d^2 r_i(t)}{dt^2} \quad (2.23)$$

where m_i is the mass of atom i , $r_i(t)$ is the position of atom i at time t , $\vec{v}_i(t)$ its velocity at time t , and $\vec{F}_i(t)$ the force acting on atom i at time t . In order to update the velocity and position of atom i at each timestep, the force $\vec{F}_i(t)$ acting on it must be known. In MD the force can be analytically derived from interatomic potentials which are an analytical

expression of the potential energy $U(\mathbf{r})$ of the atoms of the system that allow calculating the forces. Section 2.4.3.2 delves into more detail on interatomic potentials. For each particle i , the force acting on it is given by the negative gradient of the potential energy with respect to its position \mathbf{r}_i :

$$\mathbf{F}_i = -\nabla_i U(\mathbf{r}) \quad (2.24)$$

To propagate over time the positions and velocities of each atom through the equation of motion (2.23 and 2.24), integration algorithms are employed. It updates the positions and velocities of the particles, progressing from a time step t to the next time step $t + \Delta t$. Several integration algorithms exist, each with its own advantages and disadvantages. The following section presents the most commonly used algorithms.

2.4.2 Integration algorithms

At each timestep Δt , the motion of the particles is described by second-order differential equations. To solve these second-order differential equations, an integration algorithm is used.

2.4.2.1 Position-Verlet

The Position-Verlet algorithm [12] is valued for its simplicity, stability, and its ability to conserve energy well over long simulation periods. The algorithm is based on a Taylor series approximation to predict the future position of particles based on their current position and acceleration:

$$\begin{cases} \vec{r}_i(t + \Delta t) = \vec{r}_i(t) + \frac{d\vec{r}_i(t)}{dt}\Delta t + \frac{1}{2!}\frac{d^2\vec{r}_i(t)}{dt^2}\Delta t^2 + \frac{1}{3!}\frac{d^3\vec{r}_i(t)}{dt^3}\Delta t^3 + \mathcal{O}(\Delta t^4) \\ \vec{r}_i(t - \Delta t) = \vec{r}_i(t) - \frac{d\vec{r}_i(t)}{dt}\Delta t + \frac{1}{2!}\frac{d^2\vec{r}_i(t)}{dt^2}\Delta t^2 - \frac{1}{3!}\frac{d^3\vec{r}_i(t)}{dt^3}\Delta t^3 + \mathcal{O}(\Delta t^4) \end{cases} \quad (2.25)$$

with 2.25 we can get:

$$\vec{r}_i(t + \Delta t) = 2\vec{r}_i(t) - \vec{r}_i(t - \Delta t) + \frac{\vec{F}_i(\vec{r}_i(t))}{m_i}\Delta t^2 + \mathcal{O}(\Delta t^4) \quad (2.26)$$

With:

$$\frac{d^2\vec{r}_i(t)}{dt^2} = \frac{\vec{F}_i(\vec{r}_i(t))}{m_i} \quad (2.27)$$

that can also be written as:

$$\vec{r}_i(t + \Delta t) = 2\vec{r}_i(t) - \vec{r}_i(t - \Delta t) + \frac{\vec{F}_i(\vec{r}_i(t))}{m_i}\Delta t^2 + \mathcal{O}(\Delta t^4) \quad (2.28)$$

with $\mathcal{O}(\Delta t^4)$ the error order.

Unfortunately, a problem arises with this algorithm: it requires the positions from the two previous timesteps to be able to start the algorithm. In addition, velocities are not computed directly and must be determined after the calculation of $\vec{r}_i(t + \Delta t)$, by subtracting $\vec{r}_i(t - \Delta t)$ from $\vec{r}_i(t + \Delta t)$, with an overall error on the order of $\mathcal{O}(\Delta t^2)$

2.4.2.2 Velocity-Verlet

The Velocity-Verlet algorithm [12] addresses the previous problems. This algorithm is also based on Taylor series, one for position and one for velocity:

$$\begin{cases} \vec{r}_i(t + \Delta t) = \vec{r}_i(t) + \frac{d\vec{r}_i(t)}{dt} \Delta t + \frac{1}{2!} \frac{d^2\vec{r}_i(t)}{dt^2} \Delta t^2 + \mathcal{O}(\Delta t^3) \\ \vec{v}_i(t + \Delta t) = \vec{v}_i(t) + \frac{1}{2} \left(\frac{d\vec{v}_i(t)}{dt} + \frac{d\vec{v}_i(t + \Delta t)}{dt} \right) \Delta t + \mathcal{O}(\Delta t^3) \end{cases} \quad (2.29)$$

where the lower equation of the system can be obtained by writing the Taylor expansion of $\mathbf{a}_i(t + \Delta t) = \frac{d\mathbf{v}_i(t + \Delta t)}{dt}$. With the integration of Newton's equation:

$$\begin{cases} \vec{r}_i(t + \Delta t) = \vec{r}_i(t) + \vec{v}_i(t) \Delta t + \frac{1}{2m_i} \vec{F}_i(\vec{r}_i(t)) \Delta t^2 + \mathcal{O}(\Delta t^3) \\ \vec{v}_i(t + \Delta t) = \vec{v}_i(t) + \frac{1}{2m_i} \left(\vec{F}_i(\vec{r}_i(t)) + \vec{F}_i(\vec{r}_i(t + \Delta t)) \right) \Delta t + \mathcal{O}(\Delta t^3) \end{cases} \quad (2.30)$$

with $\mathcal{O}(\Delta t^3)$ the error order. With this algorithm, the startup problem is no longer an issue. The future position can be calculated using 2.30, and then, using this future position, the forces can be obtained to finally compute the future velocity.

2.4.2.3 Thermodynamical conditions

Thermodynamic conditions can be imposed using integration ensembles. Each ensemble corresponds to a set of variables that remain constant during the simulation, allowing the system's properties to be studied in a well-defined framework.

The three most common ensembles in MD are the microcanonical ensemble (NVE), the canonical ensemble (NVT), and the isothermal-isobaric ensemble (NPT).

The microcanonical ensemble (NVE) is simple and fundamental in MD. The name NVE refers to the variables that are conserved during the simulation, where N indicates that the number of particles is constant, V means the system's volume is constant, and E indicates that the system's total energy is constant. The system is isolated from its environment, meaning that neither energy nor matter can enter or leave the system during the simulation. As a result, the total energy of the system remains constant throughout the simulation.

The canonical ensemble (NVT) is an integration ensemble in which the number of particles (N), the volume (V), and the temperature (T) are kept constant. The system's temperature is maintained constant throughout the simulation, typically using a thermostat.

The temperature is controlled by adjusting the average kinetic energy of the particles.

To keep the temperature constant, numerical thermostats are used, adjusting the particle velocities so that the temperature stays close to a target value. For example, the Nosé-Hoover thermostat [13] controls temperature by adding an additional degree of freedom to represent a fictitious heat reservoir, while the Langevin thermostat [14] mimics the effect of collisions with surrounding particles by adding a random term to the equations of motion to simulate the effect of a thermal bath.

Finally, the isothermal-isobaric ensemble (NPT) is used to model systems with a constant number of particles (N), pressure (P), and temperature (T). In this ensemble, not only is the temperature controlled with a thermostat, but the pressure is also kept constant using a barostat. This allows the simulation of systems where heat and volume exchanges can occur.

2.4.3 The Case of Displacement Damage

The simulation of collision cascades with MD implies being very cautious with the parameters of the simulations. Indeed, collision cascades involve high energy particles and collisions, and the time discretization as well as the force calculations need to take this into account. Indeed, usual MD timesteps are not adequate when fast particles are involved as those particles would travel long distances between each timestep compared to thermal vibrations, and the interatomic potentials are not all built to be able to take into account close collisions. Those aspects, as well as practical considerations regarding the statistical ensembles and simulation box are detailed below.

2.4.3.1 Timestep

Unlike the continuous MC simulation method, MD method solves equation 2.23 for each particle in the simulation in a discrete manner over time. The time interval between each solution of the equation is called the timestep Δt , which is the period during which the forces acting on the particles are assumed to remain approximately constant before being recalculated. At each timestep, solving the equations allows updating the forces, positions, and velocities of the particles through an integration algorithm.

If the timestep is too large, the values of positions, velocities, and forces will undergo significant changes, leading to a loss of accuracy in tracking the simulation. It is also possible that energy will not be conserved during the simulation, or that the total energy will oscillate chaotically.

A timestep that is too small will greatly increase precision but also the computation time, as the equations will need to be solved more frequently.

Therefore, the choice of timestep is crucial; a balance must be found to ensure accurate simulation while minimizing computational cost. The usual timestep is on the order of 1 fs.

During a collision cascade, the timestep must be adapted according to the velocity of the atoms. A small timestep is chosen to cover the beginning and the ballistic phase of the cascade, *i.e.* when the velocities are high, to rigorously capture the atomic displacements. It is preferable for the timestep to capture a displacement of less than 0.25 Å. When the atoms lose velocity, the timestep is generally increased, always in such a way as to respect the factor described above.

2.4.3.2 Interatomic potentials

As explained earlier in Section 2.4.1, the forces are analytically derived from interatomic potentials. Indeed, these potentials allow the calculation of the forces acting on the particles based on their relative positions.

Interatomic potentials represent the interaction energy between particles, which can be attractive or repulsive, depending on the distance between them. The calculation of the forces directly follows from these potentials, as according to Newton's second law, the forces F_i on atom i are equal to the derivative of the potential energy U with respect to the positions r , see equation 2.24.

Typically, interatomic potentials are designed to perform well near equilibrium states. However, during collision cascades, particles gain significant energy, resulting in intense collisions, particularly at very short distances. These extreme interactions are often not accurately captured by classical interatomic potentials. Therefore, for our study, it is necessary to use a potential that accurately describes both the general properties of the material (crystal structure, melting temperature, thermal conductivity...) and the atomic interactions at small distances due to the displacement cascades. In their MD study on GaN, Nord *et al.* [15] used the Tersoff/ZBL potential, which couples the Tersoff potential [16] to model interactions at short, normal and long distances, and the ZBL [3] potential to handle repulsive forces at very short distances. This combination of potentials being well-suited for collision cascade simulations, we use it for this work.

2.4.3.3 Tersoff/ZBL potential

The Tersoff potential [16] considers three-body interactions, allowing not only the modeling of interatomic distances but also the bond angles between neighboring atoms. This is crucial for accurately representing the geometric structures of covalent materials, such as crystal lattices. It also adjusts the strength of interatomic forces based on local coordination, making it suitable for materials subjected to mechanical deformation or phase changes.

The general formula for the Tersoff potential can be written as follows:

$$V_{Tersoff}(r) = f_c(r_{ij}) [f_R(r_{ij}) - b_{ij}f_A(r_{ij})] \quad (2.31)$$

where:

- r_{ij} is the distance between atoms i and j ,
- $f_c(r_{ij})$ is the cut-off function, which becomes zero for distances beyond a certain limit. This function controls the distance at which interactions between atoms become significant,

$$f_c(r) = \begin{cases} 1, & r_{ij} < R - D \\ \frac{1}{2} - \frac{1}{2} \sin\left(\frac{\pi}{2} \frac{r_{ij} - R}{D}\right), & R - D \leq r_{ij} \leq R + D \\ 0, & r_{ij} > R + D \end{cases} \quad (2.32)$$

with : R a central threshold distance, D a tolerance around R and the different domains:

- $f_c(r) = 1$: Full interaction if $r_{ij} < R - D$ (normal distance).
- Smooth transition for $R - D \leq r_{ij} \leq R + D$ via a sinusoidal function.
- $f_c(r) = 0$: No interaction if $r_{ij} > R + D$ (long distance).
- b_{ij} is the modulation factor depending on local coordination, introducing angular dependence and the nature of covalent bonds. It adjusts the bonding strength between two atoms i and j based on their local environment.

$$b_{ij} = \left(1 + \beta^n \zeta_{ij}^n\right)^{-1/2n} \quad (2.33)$$

with :

- ζ_{ij} represents the influence of the neighbors of j on i .
- β and n are adjustable parameters that determine sensitivity to the atomic environment.
- $f_R(r_{ij})$ is the repulsive part at short distances (due to nuclear interactions),

$$f_R(r) = Ae^{-\lambda_1 r} \quad (2.34)$$

- $f_A(r_{ij})$ is the attractive part at long distances (due to chemical bonding interactions),

$$f_A(r) = Be^{-\lambda_2 r} \quad (2.35)$$

where A , B , λ_1 , and λ_2 are parameters adjusted for each material.

The ZBL potential [3] can be expressed as follows:

$$V_{ZBL}(r) = \frac{Z_1 Z_2 e^2}{4\pi\epsilon_0 r} \Phi\left(\frac{r}{a}\right) \quad (2.36)$$

where:

- Z_1 and Z_2 are the atomic numbers of atoms i and j ,
- e is the elementary charge,
- ϵ_0 is the permittivity of free space,
- r is the interatomic distance,
- $\Phi(r/a)$ is a screening function that models the electron shielding, defined as:

$$\Phi(x) = 0.1818e^{-3.2x} + 0.5099e^{-0.9423x} + 0.2802e^{-0.4029x} + 0.02817e^{-0.2016x} \quad (2.37)$$

where $x = r/a$, and a is a characteristic length parameter:

$$a = \frac{0.8854 a_0}{Z_1^{0.23} + Z_2^{0.23}} \quad (2.38)$$

In the Tersoff-ZBL potential, these two approaches are combined to handle interactions at different interatomic distance scales. The Tersoff potential is used to model chemical interactions (covalent bonds) in most situations where atoms are at normal distances, while the ZBL potential takes over to model repulsion at very short distances.

The combination is achieved via a transition function from the Tersoff potential to the ZBL potential when the distance between atoms becomes sufficiently small.

The total potential is given by:

$$E = \frac{1}{2} \sum_i \sum_{j \neq i} (1 - f_F(r_{ij})) V^{ZBL}(r_{ij}) + f_F(r_{ij}) V^{Tersoff}(r_{ij}) \quad (2.39)$$

To ensure a smooth connection between these two potentials, a cut-off function $f_F(r)$ is generally used to make the ZBL potential dominate at short distances and the Tersoff potential dominate at longer distances. The function $f_F(r)$ is given by:

$$f_F(r) = \frac{1}{1 + e^{A_F(r-r_c)}} \quad (2.40)$$

where:

- r is the adjusted distance between two particles i and j ,

#	m	γ	μ	c	d	h	n
Ga-Ga-Ga	1.0	0.007874	1.846	1.918000	0.75000	-0.301300	1.0
Ga-Ga-N	1.0	0.001632	0.000	65.20700	2.82100	-0.518000	1.0
Ga-N-Ga	1.0	0.007874	1.846	1.918000	0.75000	-0.301300	1.0
N-Ga-Ga	1.0	0.001632	0.000	65.20700	2.82100	-0.518000	1.0
N-N-Ga	1.0	0.001632	0.000	65.20700	2.82100	-0.518000	1.0
N-Ga-N	1.0	0.766120	0.000	0.178493	0.20172	-0.045238	1.0
Ga-N-N	1.0	0.001632	0.000	65.20700	2.82100	-0.518000	1.0
N-N-N	1.0	0.766120	0.000	0.178493	0.20172	-0.045238	1.0
Si-Si-Si	1.0	1.0	0.000	1.0039e5	1.6217e1	-5.9825e-1	7.8734e-1
Ge-Ge-Ge	3.0	1.0	0.0	1.0643e5	15.652	-0.43884	0.75627

#	β	λ_2	$X_{ij}B$	R_c	D_c	λ_1	A	Z_i	Z_j	rF	rB
Ga-Ga-Ga	1.0	1.44970	410.132	2.87	0.15	1.60916	535.199	31	31	0.86	14
Ga-Ga-N	1.0	0.00000	0.00000	2.90	0.20	0.00000	0.00000	31	31	0.86	14
Ga-N-Ga	0.0	0.00000	0.00000	2.87	0.15	0.00000	0.00000	31	7	0.95	14
N-Ga-Ga	1.0	2.63906	3864.27	2.90	0.20	2.93516	6136.44	7	31	0.95	14
N-N-Ga	0.0	0.00000	0.00000	2.90	0.20	0.00000	0.00000	7	7	0.6	7.5
N-Ga-N	0.0	0.00000	0.00000	2.20	0.20	0.00000	0.00000	7	31	0.95	14
Ga-N-N	1.0	2.63906	3864.27	2.90	0.20	2.93516	6136.44	31	7	0.95	14
N-N-N	1.0	2.38426	423.769	2.20	0.20	3.55779	1044.77	7	7	0.6	7.5
Si-Si-Si	1.1e-6	1.7322	4.7118e2	2.85	0.15	2.4799	1.8308e3	14	14	0.95	14
Ge-Ge-Ge	9.0166e-7	1.7047	419.23	2.95	0.15	2.4451	1769.0	32	32	0.97	10.0

Table 2.1: Comparison of material interatomical parameters: (a) Parameters for GaN [15, 17, 18], Si [19] and Ge [20].

- A_F controls the slope or the transition between the two potentials,
- r_c is the cutoff distance characterizing the transition.

A_F and r_c must be determined for every couple of atoms of different type considered.

In our study of collision cascades in GaN, we used the parameters found in [15]. For comparison, we also studied the displacement effects induced by collision cascades in Si and Ge, with the potential parameters respectively taken from [21] and [11]. The parameters are available in Table 2.1.

2.4.4 Available tool

There are numerous MD simulation tools available. We use LAMMPS (Large-scale Atomic/ Molecular Massively Parallel Simulator) [22] for all of our MD work in this thesis. LAMMPS is open-source and particularly renowned for its efficiency and flexibility. Designed to take advantage of massively parallel architectures, LAMMPS allows the modeling of systems containing several million atoms, making it ideal for large-scale simulations.

2.4.5 Advantages and limitations

MD is a powerful method for modeling systems at the atomic and molecular scale, providing a complete description of dynamic phenomena. It allows the study of events in a discrete time manner while providing direct access to the thermodynamic and structural properties of simulated systems. Its flexibility in modeling complex systems over time makes it an essential method for our project.

However, MD has some disadvantages, particularly regarding the time size and scales it can model. Simulations are often limited to time scales ranging from femtoseconds to nanoseconds and system sizes of a few million atoms. Although supercomputer advances now allow systems to contain a very large number (hundreds of millions) of particles, a new problem arises: the size of the output files. It is sometimes necessary to use many timesteps for the sake of precision, which results in output files containing positions, velocities, and other information for millions of atoms, multiplied by the number of timesteps. The file size then becomes substantial and can sometimes exceed tens of gigabytes. If the simulation is repeated hundreds of times to obtain good statistics, terabytes of data can quickly accumulate. It is therefore crucial to properly manage data handling, especially in storage-limited environments. Additionally, complex or large-scale systems require significant computational resources.

2.4.6 Threshold Displacement Energy

MD encompasses a large part of our study on GaN, whether in the investigation of the TDE, the number of defects generated at the end of a cascade, or the dynamic phase of these events. It is therefore essential to thoroughly understand and carefully manage

the use of this method to optimize simulations as much as possible in the context of displacement damage. As explained in Section 2.4.3.3, in addition to using an appropriate potential, other parameters must also be taken into account.

In order to better explain these parameters, this section is structured as a description of the methodology specifically used to initiate cascade collision simulations in MD.

The first step is to model our system. For this, the simulation box is created with a certain size that allows it to contain the entire collision cascade. Since the boundaries are periodic, the cascade could potentially overlap if the box is too small. For highly energetic collision cascades, the box size may exceed 500 Å and contain tens of millions of atoms.

Next, the box is divided into two regions containing atoms. One is the NVE region, also called the inner region, which will contain the cascade, and the other is the NVT region located at the boundary. It is mandatory for the cascade to occur in an NVE ensemble because NVT and NPT ensembles would distort the results by altering the equations of motion due to the constant maintenance of temperature or pressure. The bordering NVT region allows the heat generated by the collision cascade to dissipate and prevents the temperature from uncontrollably rising in the NVE region.

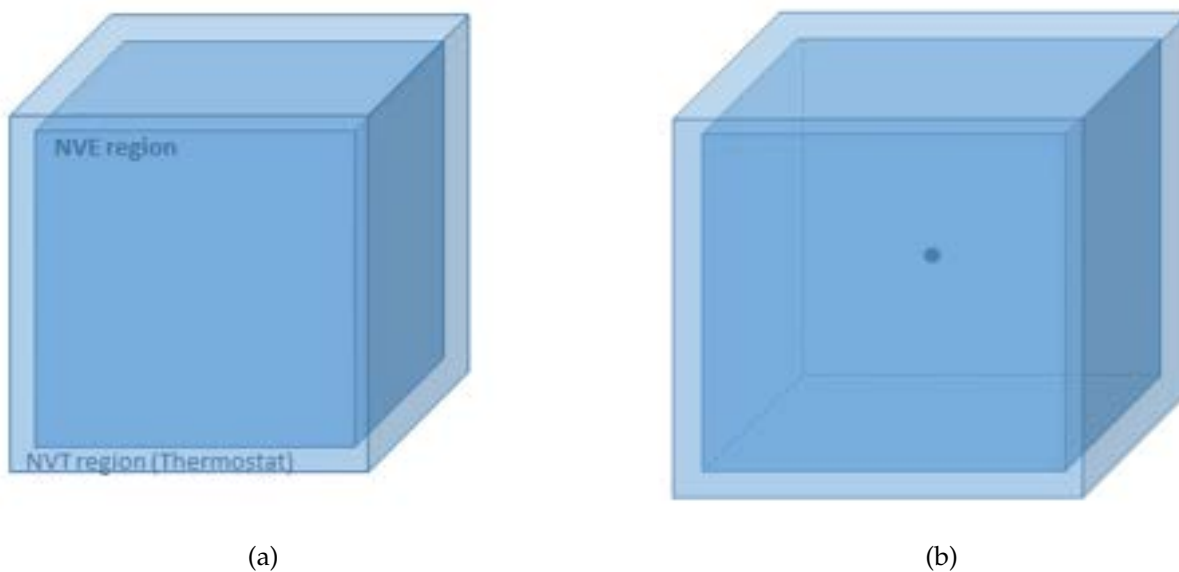


Figure 2.7: Schematic representation of the simulation box: a) illustration of the NVE and NVT regions, b) positioning of the PKA at the center of the box.

After performing temperature equilibration and force minimization to ensure that these are at their equilibrium values before starting the cascade simulation, an atom in the simulation box is chosen to be the PKA. A vector is assigned to it to give it a velocity and direction. The position of the PKA is crucial for the proper execution of the simulation.

At low energy (in our study, around 1 keV), the PKA is generally chosen at the center of the box, as in Figure 2.7 (b), as the energy is not high enough for the cascade to reach the boundaries of the simulation box. However, for more energetic cascades, the position of the PKA must be optimized according to its initial direction.

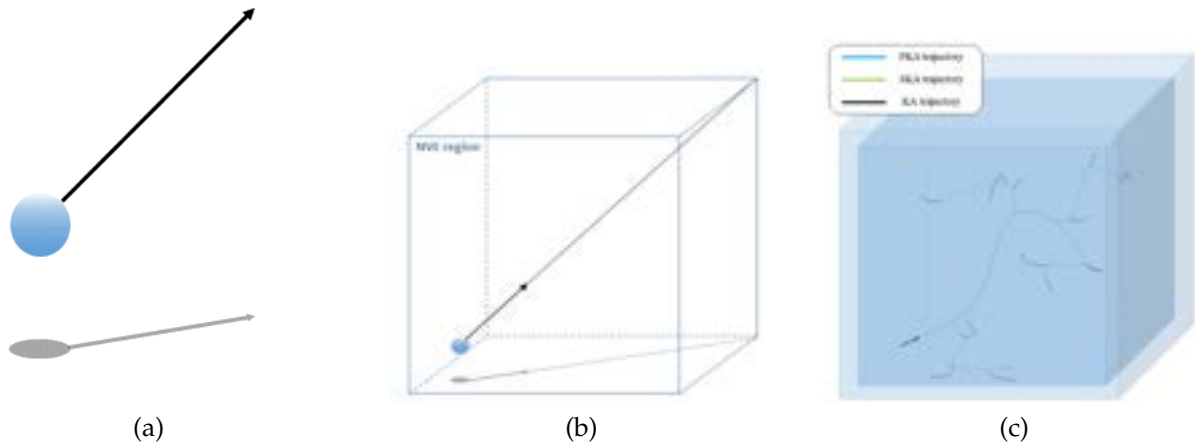


Figure 2.8: Schematic representation of: a) the PKA with a vector indicating its direction and energy to enable its movement, b) the PKA optimally positioned within the simulation box to maximize its travel distance without exiting it, and c) the trajectories of displaced atoms (remaining within the simulation box) following the cascade.

Figure 2.8 describes this optimization process. We take into account the direction of the vector and then choose the PKA in such a way that there is the maximum distance for the collision cascade to occur. We often aim at aligning the direction with the diagonal of the cube that represents the simulation box as shown in Figure 2.8b.

During the cascade, the series of collisions between atoms creates displacements. These interactions are highly stochastic, as they depend on many variable factors such as the direction of the PKA and the positions of the atoms which is a temperature influenced parameter, at the moment of the collision. Due to this random nature, collision cascade simulations must be repeated multiple times to obtain reliable statistics on the damage created.

In order to broaden the spectrum of extreme events that could occur and to conduct a fair and rigorous statistical study, several works have focused on determining the number of cascades to simulate in order to meet the previously stated requirement. A detail to keep in mind is that the number of simulations in the study is limited by the computational cost and the time allocated to it. Therefore, a balance must be found between the number of simulations needed to obtain converged results and the time cost.

Jarrin *et al.*[23] have shown that a minimum of 100 simulations must be carried out to obtain converged statistical data, similarly to Buchan *et al.* [24] and Christie *et al.* [25]. It is shown that selecting a set of directions by considering symmetry, rather than

choosing these directions randomly, facilitates result convergence. Indeed, the directions are uniformly distributed on the surface of a sphere, and only those directions located within the minimal spatial domain, not equivalent to others by crystalline symmetries, as shown in Figure 2.9, are considered. This method was introduced by Jay *et al.* [26].

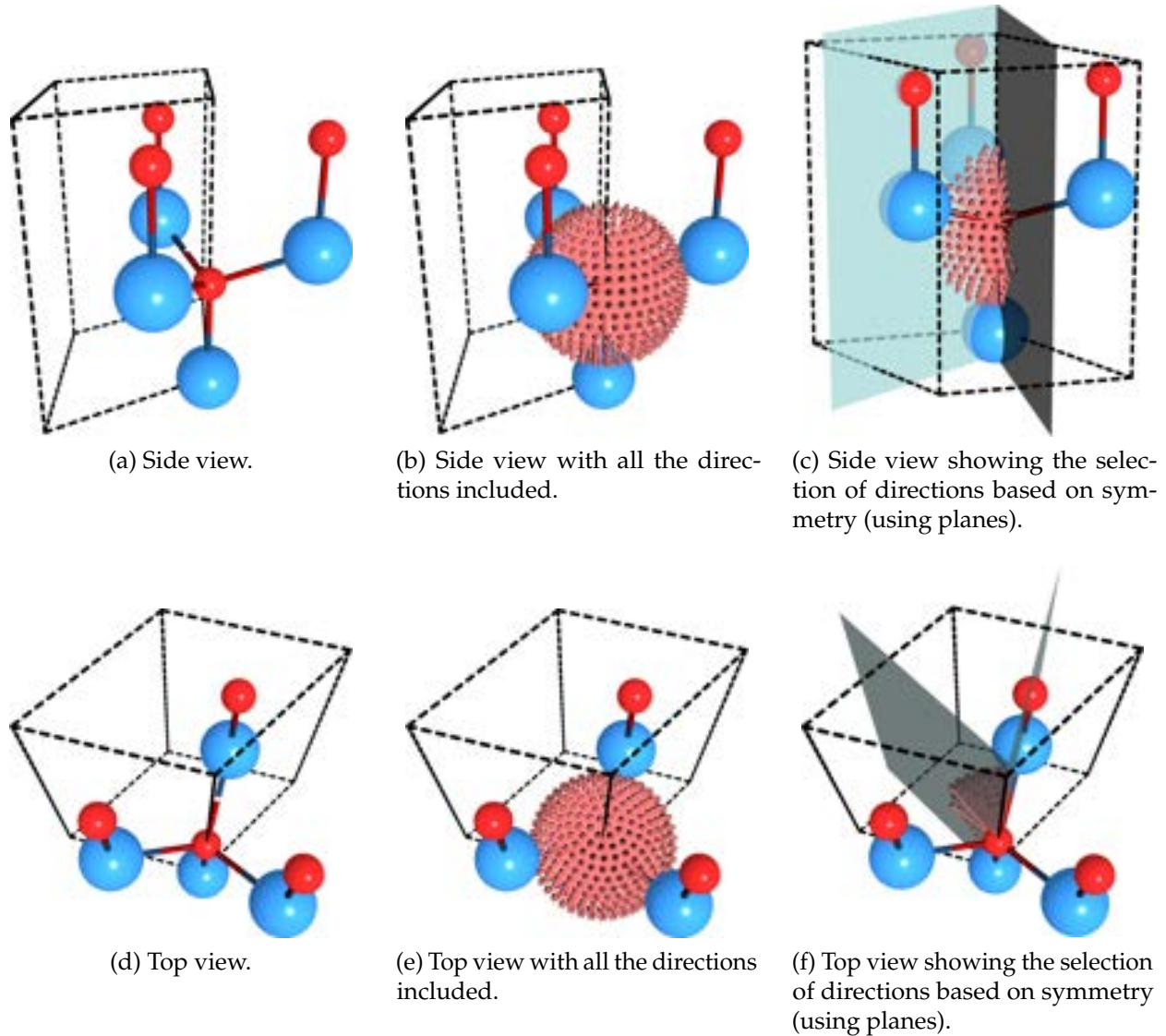


Figure 2.9: Schematic representation of the selection of directions according to symmetry. With the elementary cell in dotted lines, Ga atoms (blue), N atoms (red), vectors in pink, and planes in green.

In a very similar manner as for collision cascades, MD can be employed to calculate TDE. The simulations are set up in the same way as for the cascades, but as the energies studied are lower, some of the simulation parameters are modified accordingly. The simulation boxes are smaller and the simulations require less time. For more details, refer to Section 4.3.2 of Chapter 4.

2.5 *Ab initio* Methods

2.5.1 *Ab initio* Molecular Dynamics

Ab Initio Molecular Dynamics (AIMD) [27, 28] combines the approaches of DFT and MD by sequentially calculating the electronic density and the motion of atoms. First, the ground state energy is computed using DFT based on the current atomic configuration, including the potential energy and forces acting on each atom. These forces are then used in MD to update the positions and velocities of the atoms for the next time step. Subsequently, the new ground state energy is determined through DFT for this new configuration, and the cycle repeats. This iterative process allows the simulation of atomic-scale systems by accurately accounting for electronic effects, avoiding the empirical approximations inherent to classical methods. By calculating the electronic density at each step, the AIMD method is particularly effective for modelling accurately complex phenomena, such as chemical reactions and charge transfer.

However, AIMD has also drawbacks. The method is extremely computationally demanding because of the DFT part. Although solving the equations in MD is fast, calculating the forces using DFT is much slower. This computational cost often makes AIMD impractical for large systems or simulations requiring long timescales. Consequently, researchers are often forced to restrict the size of the system or the duration of the simulation, limiting its applicability compared to classical MD methods.

2.5.2 Density Functional Theory

Density Functional Theory (DFT) is a computational method that solves the Schrödinger equation to describe the electronic properties of a system based on electron density rather than the complex wavefunction of a set of electrons. Based on the Hohenberg-Kohn theorems, DFT asserts that all properties of a quantum system can be derived solely from its electron density, which greatly simplifies the calculations. The practical implementation of DFT relies on the approximation of the exchange-correlation functional, explained in Section 2.5.2.5, which accounts for complex electronic interactions. This section is based on the excellent work of Sholl and Steckel [29].

2.5.2.1 Schrödinger equation, Born-Oppenheimer and electron density

Let's take as an example the task of describing the atoms that make up a crystal. A fundamental piece of information to know is the energy of each atom and how it changes if the atoms are displaced. To determine where an atom is located, we need to know the position of its nucleus. Using quantum mechanics we will try to find out more about these atoms. We can use the Schrödinger equation, as follows:

$$\hat{H}\Psi = E\Psi \quad (2.41)$$

Where:

- The Hamiltonian \hat{H} is the total energy operator of the system, responsible for the time

evolution of quantum states.

- The wave function Ψ describes the quantum state of the system. Each solution Ψ_n has an associated eigenvalue E_n , a real number that satisfies the eigenvalue equation.

For describing the electronic structure of a system with multiple nuclei and electrons the equation is:

$$\hat{H}\Psi = \left[-\sum_i^N \frac{\hbar^2}{2m} \nabla_i^2 - \sum_I^A \frac{\hbar^2}{2M} \nabla_I^2 - \sum_{i,I} \frac{Z_I e^2}{|\vec{r}_i - \vec{R}_I|} + \sum_{i<j} \frac{e^2}{|\vec{r}_i - \vec{r}_j|} + \sum_{I<J} \frac{Z_I Z_J e^2}{|\vec{R}_I - \vec{R}_J|} \right] \Psi = E\Psi, \quad (2.42)$$

The first two terms of the Hamiltonian are the kinetic energy operators for the N electrons i and the A atomic nuclei I , respectively. The last three terms represent the interaction potentials for electron-nucleus, electron-electron and nucleus-nucleus interactions.

In this form, the Schrödinger equation is too complex to solve analytically. To simplify its resolution, Max Born and Robert Oppenheimer proposed an approximation to simplify the Schrödinger equation. This is based on the fact that there is a significant difference in mass between the nucleus and the electron; a neutron or proton has a mass approximately 1,800 times greater than that of an electron. Therefore, an electron tends to respond much faster to changes in its environment than a nucleus.

This allow us to proceed as follows: we fix the positions of the nuclei and solve the equations of motion for the electrons. We find the most stable energy configuration (ground state) for these electrons in the field of a set of fixed nuclei. This separation is called the Born-Oppenheimer approximation. If we have M nuclei at positions $R_1, R_2, R_3, \dots, R_M$, then we can express the ground state energy as a function of these positions: $E(R_1, \dots, R_M)$.

Under the Born-Oppenheimer approximation, the positions of the atomic nuclei are considered fixed; hence, their kinetic energy can be neglected and the nucleus-nucleus interaction term can be treated as a constant (denoted E_{II}). The resulting equation becomes:

$$\hat{H}\Psi = [T_e + V_{ei} + V_{ee} + E_{II}] \Psi = E\Psi, \quad (2.43)$$

where:

$$T_e = -\sum_i^N \frac{\hbar^2}{2m} \nabla_i^2, \quad (2.44)$$

$$V_{ei} = -\sum_{i,I} \frac{Z_I e^2}{|\vec{r}_i - \vec{R}_I|}, \quad (2.45)$$

$$V_{ee} = \sum_{i<j} \frac{e^2}{|\vec{r}_i - \vec{r}_j|}. \quad (2.46)$$

To simplify the notation, we conventionally represent the kinetic energy operator by

T , the external potential felt by the electrons by V_{ext} , and the electron-electron interaction potential by U . The equation then takes a more compact form:

$$H\Psi = [T + V_{\text{ext}} + U] \Psi = E\Psi. \quad (2.47)$$

Many methods have been developed to solve the multi-electron Schrödinger equation, such as describing the wavefunction with a Slater determinant:

$$\Psi(r_1, r_2, \dots, r_N) = \frac{1}{\sqrt{N!}} \begin{vmatrix} \phi_1(r_1) & \phi_2(r_1) & \dots & \phi_N(r_1) \\ \phi_1(r_2) & \phi_2(r_2) & \dots & \phi_N(r_2) \\ \vdots & \vdots & \ddots & \vdots \\ \phi_1(r_N) & \phi_2(r_N) & \dots & \phi_N(r_N) \end{vmatrix} \quad (2.48)$$

$\phi_i(r)$ are the spatial orbitals of the electrons. This wave function automatically satisfies the antisymmetry required by the Pauli exclusion principle.

We use an other approximation called the Hartree product, defined as follows: Ψ can be approximated as a product of individual electronic wavefunctions:

$$\Psi = \Psi_1(r) \cdot \Psi_2(r) \cdot \dots \cdot \Psi_N(r) \quad (2.49)$$

However, the number of electrons is much greater than the number of atoms, so the number of dimensions explodes as the number of atoms increases. This poses a challenge when determining the electron-electron interaction term. It is not possible to find the contribution of an individual electronic wavefunction without considering the electronic wavefunctions of the other electrons. To address this issue, we can measure the probability that N electrons are at particular coordinates r_1, \dots, r_N . This probability is given by:

$$\Psi^*(\mathbf{r}_1, \dots, \mathbf{r}_N) \Psi(\mathbf{r}_1, \dots, \mathbf{r}_N) \quad (2.50)$$

It is then possible to define the electron density:

$$n(\mathbf{r}) = 2 \sum_i \Psi_i^*(\mathbf{r}) \Psi_i(\mathbf{r}) \quad (2.51)$$

The factor of 2 appears due to the electron spin and the Pauli exclusion principle, which states that each individual electronic wavefunction can be occupied by different electrons only if they have opposite spins.

The electron density $n(\mathbf{r})$ is a function of only three coordinates, yet it contains a lot of physically observable information from the complete wavefunction solution to the Schrödinger equation, which is a function of $3N$ coordinates.

The electronic density is the cornerstone of the DFT method, but to go further, it is necessary to rely on theorems, which the next section introduces.

2.5.2.2 Hohenberg-Kohn theorems

DFT is based on two mathematical theorems introduced by P. Hohenberg and W. Kohn.

The first theorem states that the ground state energy of the Schrödinger equation is a unique functional of the electronic density. In other words, the ground state energy E can be expressed as:

$$E[n(\mathbf{r})] \quad (2.52)$$

Thus, this means that, theoretically, it is possible to calculate the ground-state energy using only $n(\mathbf{r})$, which reduces the complexity of the problem from $3N$ variables to just 3 spatial variables.

However, in practice, approximations must be made. Determining $n(\mathbf{r})$ or $E[n(\mathbf{r})]$ requires the use of approximations or additional methodologies, notably through solving the Kohn-Sham equations.

The second theorem establishes that the electronic density that minimizes the energy of the entire functional is the true ground state electronic density corresponding to the full solution of the Schrödinger equation.

The goal is to vary the electronic density until the energy of the functional is minimized. Therefore, we need to know the form of the functional, which can be written using one-electron wavefunctions, $\Psi_i(\mathbf{r})$:

$$E[\{\Psi_i\}] = E_{\text{known}}[\{\Psi_i\}] + E_{\text{XC}}[\{\Psi_i\}] \quad (2.53)$$

The functional is split into two parts: a simple analytical form with the term $E_{\text{known}}[\{\Psi_i\}]$, and everything else in the term $E_{\text{XC}}[\{\Psi_i\}]$. More specifically, the analytical term includes four contributions:

$$E_{\text{known}}[\{\Psi_i\}] = -\frac{\hbar^2}{m} \sum_i \int \Psi_i^* \nabla^2 \Psi_i d^3r + \int V(\mathbf{r}) n(\mathbf{r}) d^3r + \frac{e^2}{2} \int \int \frac{n(\mathbf{r}) n(\mathbf{r}')}{|\mathbf{r} - \mathbf{r}'|} d^3r d^3r' + E_{\text{ion}} \quad (2.54)$$

Where:

- $-\frac{\hbar^2}{m} \sum_i \int \Psi_i^* \nabla^2 \Psi_i d^3r$ is the kinetic energy of the electrons,
- $\int V(\mathbf{r}) n(\mathbf{r}) d^3r$ describes the Coulomb interactions between the electrons and the nuclei,
- $\frac{e^2}{2} \int \int \frac{n(\mathbf{r}) n(\mathbf{r}')}{|\mathbf{r} - \mathbf{r}'|} d^3r d^3r'$ represents the Coulomb interactions between pairs of electrons,
- E_{ion} accounts for the Coulomb interactions between pairs of atoms.

The other term, $E_{\text{XC}} [\{\Psi_i\}]$, is the exchange-correlation functional, which includes all quantum mechanical effects not accounted for in the analytical term. Unfortunately, several challenges still block the path to solving the Schrödinger equation completely.

2.5.2.3 Kohn and Sham equations

To finally approach the resolution of the Schrödinger equation, W. Kohn and L. Sham demonstrated that the correct electronic density can be expressed using a set of equations, where each equation involves only a single electron:

$$\left[-\frac{\hbar^2}{2m} \nabla^2 + V(\mathbf{r}) + V_{\text{H}}(\mathbf{r}) + V_{\text{XC}}(\mathbf{r}) \right] \Psi_i(\mathbf{r}) = \varepsilon_i \Psi_i(\mathbf{r}) \quad (2.55)$$

Where:

$$V_{\text{H}}(\mathbf{r}) = e^2 \int \frac{n(\mathbf{r}')}{|\mathbf{r} - \mathbf{r}'|} d^3 r' \quad (2.56)$$

is the Hartree potential, which describes classical Coulomb interaction between charges defined by a density. A drawback of this potential is that it also accounts for the interaction of the electron with itself.

$$V_{\text{XC}}(\mathbf{r}) = \frac{\delta E_{\text{XC}}(\mathbf{r})}{\delta n(\mathbf{r})} \quad (2.57)$$

is the exchange-correlation potential, defined as the functional derivative of the exchange-correlation energy. This is a corrective term that models both the exchange effects (due to the Pauli exclusion principle) and the correlation effects (dynamic interactions between electrons).

Here arises a fundamental loop: to solve the Kohn-Sham equation, we need the Hartree potential $V_{\text{H}}(\mathbf{r})$, which depends on the electronic density. However, to find this density, we need the one-electron wavefunctions. These wavefunctions, in turn, can only be determined by solving the Kohn-Sham equation itself. This recursive dependency necessitates a systematic approach, commonly referred to as the DFT cycle, to resolve the issue.

2.5.2.4 DFT cycle

The DFT cycle is a self-consistent iterative algorithm designed to solve the Kohn-Sham equations. Figure 2.10 schematically represents its operation. To be more specific, here are each of the steps:

Step 1 - Define an initial guess for the electronic density $n(r)$.

Step 2 - Compute the Kohn-Sham potentials.

Step 3 - Solve the Kohn-Sham equations.

Step 4 - Calculate the new electronic density $n(r)$.

Step 5 - Compare the newly calculated electronic density to the previous iteration's density. If the two densities converge within a predefined tolerance, the self-consistent solution is reached, and the ground-state electronic density is determined. This density can then be used to calculate various properties of the system. If the densities do not converge, return to Step 2, using the new density as the updated input.

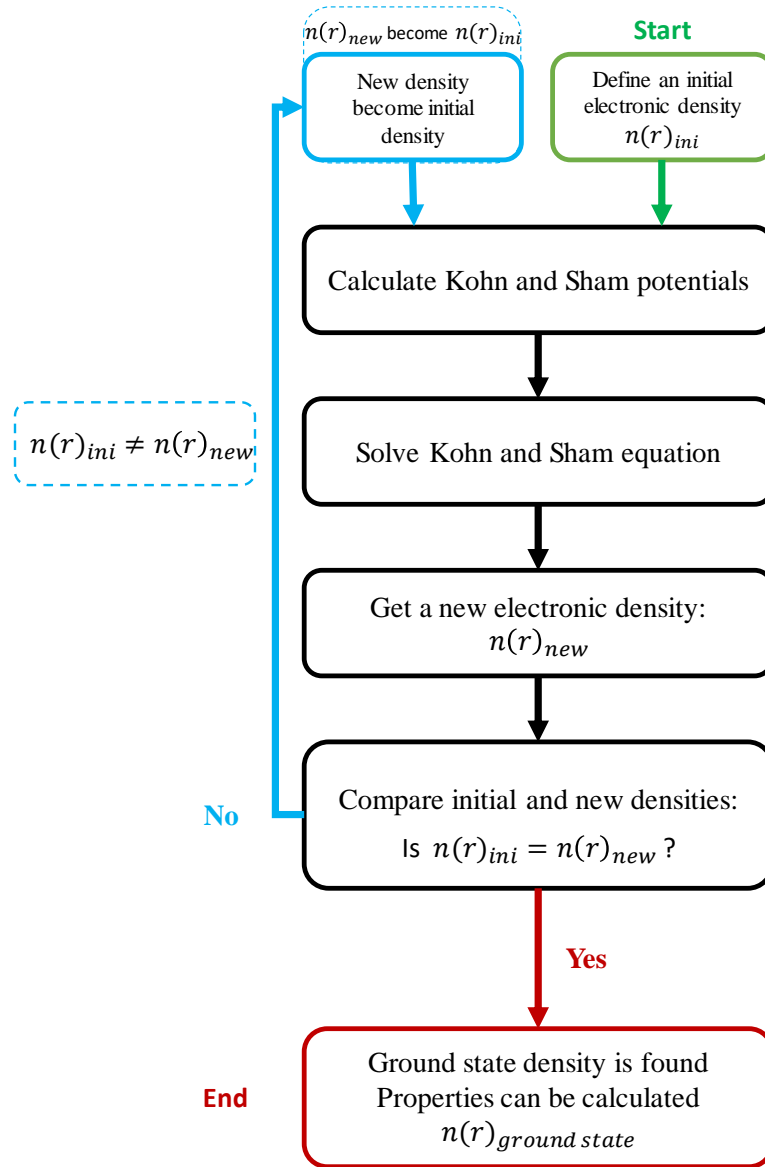


Figure 2.10: The self-consistent scheme used in DFT.

There remains one last problem to solve: we need to find the exchange-correlation function $E_{xc}[\{\Psi_i\}]$ to be able to solve the Kohn-Sham equations.

2.5.2.5 Approximations

Since E_{xc} is challenging to determine precisely, several approximations can be employed. The most well-known approximation is the Local Density Approximation (LDA): it assumes that E_{xc} is a function only of the local density at each point in space. Indeed, for a uniform electron gas, the electronic density is constant, which allows defining the exchange-correlation functional. The exchange-correlation potential is set at each position to be the exchange-correlation potential derived from a uniform electron gas at the electronic density at those positions.

$$E_{xc}[n] = \int n(\vec{r}) \epsilon_{xc}[n] d\vec{r} \quad (2.58)$$

Another approximation is the Generalized Gradient Approximation (GGA): it adds a spatial variability criterion for the electronic density, considering that real systems are not homogeneous. The spatial variation of the density is expressed through the exchange and correlation energies, as functions of the density and its gradient. Generally, in the GGA approximation, the exchange-correlation energy is defined as:

$$E_{xc}^{GGA}[n_\alpha, n_\beta] = \int n(\vec{r}) \epsilon_{xc}[n_\alpha, n_\beta, \nabla n_\alpha, \nabla n_\beta] d^3r \quad (2.59)$$

Other approximations may also be used but are not described here.

2.5.2.6 Plane wave formalism

Another crucial aspect, which governs many parameters, is the construction of single-electron wavefunctions from plane waves [30]. In the case of crystal, single-electron wavefunctions are periodic according to the unit cell, and it is defined as follows:

$$\Psi(r) = \sum_{\vec{G}} C_{\vec{G}} e^{i\vec{G}\vec{r}} \quad (2.60)$$

are vectors of the reciprocal space and \tilde{C} are plane-wave coefficients. The more \vec{G} vectors are employed, the closer to the real wavefunction will be the plane-wave summation. However, the number of plane-waves should be finite. Therefore, in order to set an upper value to the number of plane waves, we define an energy cutoff E_{cut} . Only \vec{G} vectors whose norm is lower than G_{cut} , defined by the following equation, are employed:

$$E_{\text{cut}} = \frac{\hbar^2 G_{\text{cut}}^2}{2m} \quad (3.98)$$

This rule sets an upper bound on the number of plane-waves. However, it must be ensured that enough plane-waves are employed to have converged calculations.

In cases where heavy atoms are present, core electrons have rapid variations around the nucleus, making plane waves inefficient due to the need for a very large number of waves to capture these details.

Pseudopotentials are used to circumvent this issue by replacing the actual nuclear potential with a simplified potential for valence electrons, masking the core electrons while preserving their overall effects. This simplification allows valence electrons to be represented with a more reasonable number of plane waves, significantly reducing computational complexity. Among common types of pseudopotentials, norm-conserving and ultrasoft pseudopotentials provide solutions for DFT calculations in the plane wave formalism.

2.5.2.7 Advantages and limitations

DFT offers many advantages compared to the methods discussed earlier in this chapter, particularly for simulating material properties and interatomic interactions. It provides much greater accuracy than the MC method and MD, especially by incorporating full electronic effects in simulations.

However, DFT also has its limitations. Exchange-correlation functionals, such as LDA or GGA, require approximations that may reduce result accuracy, and the use of this is highly dependent on the case studied. Furthermore, this method is generally limited to small systems, often around a hundred atoms, raising questions about the representativeness of the model's physical properties. As with MD, the time and computational cost of DFT can quickly become significant, thus requiring optimization of simulation parameters and sometimes even a restriction of the study.

2.5.2.8 Available tools

Several tools are available for performing DFT calculations, with some standing out due to their features and widespread use in the field. To cite some of them, VASP (the Vienna Ab initio Simulation Package) [31], is a commercial software. ABINIT [32] and Quantum ESPRESSO [33] are other open-source software tools. For this study, the TDE analyses discussed in Chapter 4 were conducted using Quantum ESPRESSO.

2.5.2.9 The case of Threshold Displacement Energy

To better understand the fundamental mechanisms underlying displacement damage in GaN, we focused on determining the threshold displacement energy (TDE) of atoms. The study primarily relied on AIMD, and while a detailed explanation is provided in Chapter 4, a brief overview of the methodology is presented here for clarity.

First, a simulation cell containing about a hundred GaN atoms is constructed. Several parametric tests were carried out using DFT to optimize the computational parameters required for simulating TDE accurately. After identifying the optimal DFT parameters, AIMD was employed to stabilize the simulation cell at a specific temperature. This preliminary simulation yielded the positions, velocities, and forces of each atom within the cell at the chosen temperature. Following stabilization, the main simulation phase commenced. Two atoms, one Ga and one N, located at the center of the cell are selected and assigned an

energy value and a directional vector. The simulation was then executed for a predetermined duration, after which the outcomes were analyzed.

In our study, the displacement threshold energy is defined as the minimum energy required for an atom to leave its equilibrium position permanently. A schematic representation of the TDE process is illustrated in Figure 2.11.

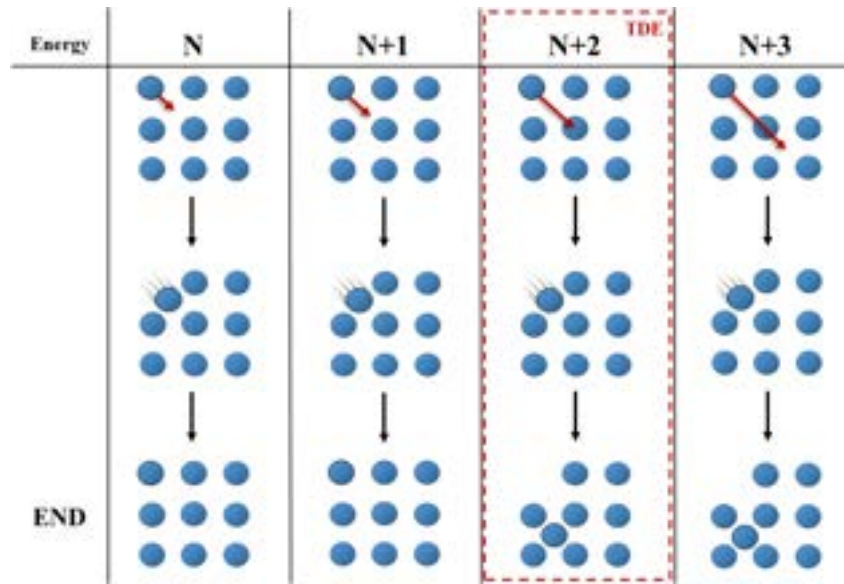


Figure 2.11: Schematic representation of TDE selection. Starting with the initial energy N , incrementing by 1: $N+1$, $N+2$, $N+3$. Here, the TDE is $N+2$, as this is the first energy for which an atom has moved and created a stable defect (in this case, a Frenkel pair).

The results are evaluated by observing whether an atom has been displaced from its equilibrium site after the simulation has run for a sufficient duration. However, in rare cases, the central atom whose energy was altered does not end up as the displaced atom. Instead, it may collide with another atom in the cell, causing the latter to be permanently displaced. In such scenarios, the energy given to the first atom is still considered the TDE.

If the assigned energy becomes excessively high, the simulation is terminated without determining the TDE. Excessive energy can lead to physical issues, such as thermal waves propagating isotropically from the energetic displacement event. These waves may cross the periodic boundaries of the simulation box and re-enter from the opposite side, destabilizing the simulation.

The combination of DFT and MD in AIMD provides more accurate descriptions of interatomic interactions than classical MD. However, the study is also conducted using classical MD because it allows simulations with much larger cells and greater statistical sampling. The methodology for classical MD simulations is similar to that described for AIMD, excluding the DFT parameterization step.

Additional details on the TDE study of GaN atoms using MD and AIMD are provided in Chapter [4](#).

2.6 Conclusion

This chapter explains the operation of all the numerical simulation tools used in our study. The multi-model approach to numerical simulation leverages the advantages of each simulation method to optimize the step-by-step study of events resulting from displacement damage due to collision cascades. Our use of this approach in this study focuses only on specific events within collision cascades, combining simulation methods to achieve the most accurate and precise results possible. The TDE is studied using MD, a simulation method that couples the solution of motion equations with the consideration of interatomic interactions through an interatomic potential, to gather as much statistical data as possible. It is also examined using AIMD, a method that additionally accounts for all electronic interactions through approximation strategies and the use of electronic density. Finally, collision cascades are studied with MD, a method best suited to represent atomic dynamics, and with MC, a simulation method that employs probability and randomness to generate extensive data.

The next chapter focuses on our results obtained in the study of collision cascades in GaN, Si, and Ge, using MC and MD simulation methods.

Bibliography

- [1] JR Srouer and JW Palko. Displacement damage effects in irradiated semiconductor devices. *IEEE Transactions on Nuclear Science*, 60(3):1740–1766, 2013.
- [2] Mélanie Raine, Antoine Jay, Nicolas Richard, Vincent Goiffon, Sylvain Girard, Marc Gaillardin, and Philippe Paillet. Simulation of single particle displacement damage in silicon—part i: global approach and primary interaction simulation. *IEEE Transactions on Nuclear Science*, 64(1):133–140, 2016.
- [3] J. F. Ziegler, M. D. Ziegler, and J. P. Biersack. SRIM - The stopping and range of ions in matter (2010). *Nuclear Instrument and Methods in Physics Research, B*, 268:1818–1823, Jun 2010. doi: 10.1016/j.nimb.2010.02.091.
- [4] Jean-Paul Crocombette and Christian Van Wambeke. Quick calculation of damage for ion irradiation: implementation in iradina and comparisons to srим. *EPJ N-Nuclear Sciences & Technologies*, 5:7, 2019.
- [5] S. Agostinelli and all. Geant4—a simulation toolkit. *Nuclear Instruments and Methods in Physics Research Section A: Accelerators, Spectrometers, Detectors and Associated Equipment*, 506(3):250–303, 2003. ISSN 0168-9002. doi: [https://doi.org/10.1016/S0168-9002\(03\)01368-8](https://doi.org/10.1016/S0168-9002(03)01368-8). URL <https://www.sciencedirect.com/science/article/pii/S0168900203013688>.
- [6] Enrico Zio and Enrico Zio. *Monte carlo simulation: The method*. Springer, 2013.
- [7] Samik Raychaudhuri. Introduction to monte carlo simulation. In *2008 Winter simulation conference*, pages 91–100. IEEE, 2008.
- [8] M. T. Robinson. The binary collision approximation: Background and introduction. *Radiation Effects and Defects in Solids*, null(1):3–20, 1994. doi: 10.1080/10420159408219767. URL <https://doi.org/10.1080/10420159408219767>.
- [9] Wolfgang Eckstein and Wolfgang Eckstein. The binary collision model. *Computer Simulation of Ion-Solid Interactions*, pages 4–32, 1991.
- [10] Christophe J. Ortiz, Laurence Luneville, and David Simeone. 1.19 - binary collision approximation. pages 595–619, 2020. doi: <https://doi.org/10.1016/B978-0-12-803581-8.11649-2>. URL <https://www.sciencedirect.com/science/article/pii/B9780128035818116492>.
- [11] Thomas Jarrin. *Modélisation des effets de déplacements atomiques induits par irradiation dans les matériaux pour la microélectronique*. PhD thesis, Toulouse 3, 2021.
- [12] Loup Verlet. Computer "experiments" on classical fluids. i. thermodynamical properties of lennard-jones molecules. *Phys. Rev.*, 159:98–103, Jul 1967. doi: 10.1103/PhysRev.159.98. URL <https://link.aps.org/doi/10.1103/PhysRev.159.98>.

- [13] Denis J Evans and Brad Lee Holian. The nose–hoover thermostat. *The Journal of chemical physics*, 83(8):4069–4074, 1985.
- [14] Ruslan L Davidchack, Richard Handel, and MV Tretyakov. Langevin thermostat for rigid body dynamics. *The Journal of chemical physics*, 130(23), 2009.
- [15] J Nord, K Nordlund, J Keinonen, and K Albe. Molecular dynamics study of defect formation in gan cascades. *Nuclear Instruments and Methods in Physics Research Section B: Beam Interactions with Materials and Atoms*, 202:93–99, 2003.
- [16] Jerry Tersoff. New empirical approach for the structure and energy of covalent systems. *Physical review B*, 37(12):6991, 1988.
- [17] J Nord, K Albe, P Erhart, and KJJoPCM Nordlund. Modelling of compound semiconductors: analytical bond-order potential for gallium, nitrogen and gallium nitride. *Journal of Physics: Condensed Matter*, 15(32):5649, 2003.
- [18] Nanjun Chen, Erich Rasch, Danhong Huang, Eric R Heller, and Fei Gao. Atomic-scale simulation for pseudometallic defect-generation kinetics and effective niel in gan. *IEEE Transactions on Nuclear Science*, 65(5):1108–1118, 2018.
- [19] R. Devanathan et al. Displacement threshold energies in β -SiC. *J. Nucl. Mat.*, 253(1):47–52, Mar 1998. ISSN 0022-3115. doi: [https://doi.org/10.1016/S0022-3115\(97\)00304-8](https://doi.org/10.1016/S0022-3115(97)00304-8).
- [20] J. Tersoff. Modeling solid-state chemistry: Interatomic potentials for multicomponent systems. *Phys. Rev. B*, 39:5566–5568, Feb 1989. doi: 10.1103/PhysRevB.39.5566.
- [21] Ramaswami Devanathan, T Diaz De La Rubia, and William J Weber. Displacement threshold energies in β -sic. *Journal of nuclear materials*, 253(1-3):47–52, 1998.
- [22] "A. P. Thompson, H. M. Aktulga, R. Berger, D. S. Bolintineanu, W. M. Brown, P. S. Crozier, P. J. in 't Veld, A. Kohlmeyer, S. G. Moore, T. D. Nguyen, R. Shan, M. J. Stevens, J. Tranchida, C. Trott, and S. J. Plimpton". "lammmps - a flexible simulation tool for particle-based materials modeling at the atomic, meso, and continuum scales". *Comp. Phys. Comm.*, 271:108171, 2022. doi: 10.1016/j.cpc.2021.108171.
- [23] Thomas Jarrin, Antoine Jay, Nicolas Richard, and Anne Hémercyck. Coping with the stochasticity of collision cascades in molecular dynamics simulations. *Nuclear Instruments and Methods in Physics Research Section B: Beam Interactions with Materials and Atoms*, 500-501:1–9, 2021. ISSN 0168-583X. doi: <https://doi.org/10.1016/j.nimb.2021.02.015>. URL <https://www.sciencedirect.com/science/article/pii/S0168583X21001683>.
- [24] JT Buchan, M Robinson, HJ Christie, DL Roach, DK Ross, and Nigel A Marks. Molecular dynamics simulation of radiation damage cascades in diamond. *Journal of Applied Physics*, 117(24), 2015.
- [25] HJ Christie, M Robinson, DL Roach, DK Ross, Irene Suarez-Martinez, and Nigel A Marks. Simulating radiation damage cascades in graphite. *Carbon*, 81:105–114, 2015.

- [26] Antoine Jay, Anne Hémerlyck, Nicolas Richard, Layla Martin-Samos, Mélanie Raine, Alexandre Le Roch, Normand Mousseau, Vincent Goiffon, Philippe Paillet, Marc Gaillardin, et al. Simulation of single-particle displacement damage in silicon—part iii: First principle characterization of defect properties. *IEEE Transactions on Nuclear Science*, 65(2):724–731, 2018.
- [27] Dominik Marx and Jurg Hutter. Ab initio molecular dynamics: Theory and implementation. *Modern methods and algorithms of quantum chemistry*, 1(301-449):141, 2000.
- [28] Eric Paquet and Herna L Viktor. Computational methods for ab initio molecular dynamics. *Advances in Chemistry*, 2018(1):9839641, 2018.
- [29] David S Sholl and Janice A Steckel. *Density functional theory: a practical introduction*. John Wiley & Sons, 2022.
- [30] Mike C Payne, Michael P Teter, Douglas C Allan, TA Arias, and ad JD Joannopoulos. Iterative minimization techniques for ab initio total-energy calculations: molecular dynamics and conjugate gradients. *Reviews of modern physics*, 64(4):1045, 1992.
- [31] journal=Journal of computational chemistry volume=29 number=13 pages=2044–2078 year=2008 publisher=Wiley Online Library Hafner, Jurg. Ab-initio simulations of materials using vasp: Density-functional theory and beyond.
- [32] Xavier Gonze, Francois Jollet, F Abreu Araujo, Donat Adams, Bernard Amadon, Thomas Applencourt, Christophe Audouze, J-M Beuken, Jordan Bieder, A Bokhanchuk, et al. Recent developments in the abinit software package. *Computer physics communications*, 205:106–131, 2016.
- [33] Paolo Giannozzi, Stefano Baroni, Nicola Bonini, Matteo Calandra, Roberto Car, Carlo Cavazzoni, Davide Ceresoli, Guido L Chiarotti, Matteo Cococcioni, Ismaila Dabo, et al. Quantum espresso: a modular and open-source software project for quantum simulations of materials. *Journal of physics: Condensed matter*, 21(39):395502, 2009.

Chapter 3:

Displacement damage in GaN and comparison with Si and Ge

Contents

3.1	Introduction	86
3.2	State of the Art on Collision Cascades in GaN and Other Semiconductors	86
3.3	Preliminary Analysis and Neutron-Displacement Damage Cross Section of GaN	88
3.3.1	Introductory Investigations	88
3.3.2	Neutron Displacement Damage Cross Section in GaN	89
3.3.2.1	Lindhard–Robinson Method	90
3.3.2.2	Threshold Displacement Energy Method	90
3.3.2.3	SRIM/TRIM Method	91
3.3.2.4	Non-Ionising Energy Loss	91
3.3.2.5	PKA distributions to Displacement damage (DD)	92
3.4	Collisions cascade and resulting displacement damage in GaN, Si and Ge	95
3.4.1	Computational details	95
3.4.2	Methodological Insights	97
3.4.2.1	Defect Quantification Using Wigner-Seitz Method	97
3.4.2.2	Understanding Maximum Penetration Depth	98
3.4.3	Results & Discussion	99
3.4.3.1	State of damage at the end of the simulations	99
3.4.3.2	Collision cascade dynamics and clustering	103
3.4.3.3	Morphology of Cascades and Interstitials Atom Displacements	107
3.4.3.4	Concluding Remarks	110
3.5	Conclusion	112

3.1 Introduction

This chapter presents our investigation into displacement damage effects in GaN, with particular emphasis on comparing its behavior with that of conventional semiconductors such as Si and Ge.

Our work is structured in three main sections: In the first section, we present a comprehensive review of the current literature on displacement damage (DD) in GaN, focusing on simulation-based studies and their key findings. In the second section, we discuss our preliminary results obtained using Monte Carlo (MC) simulations, which provide insights into the general characteristics of collision cascades and inform the parameters for subsequent molecular dynamics (MD) simulations. This section also includes a comparative analysis of neutron displacement damage cross-sections between GaN and Si. Finally in the third section, we present detailed results from our MD simulations of collision cascades, offering deeper insights into GaN's radiation resistance at various energy levels.

Within the investigated time and energy scales, our findings reveal that GaN exhibits superior resistance to radiation compared to its counterparts, Si and Ge. Notably, we observe a significant "healing" or "recrystallization" phase following collision cascades in GaN, with 93% and 83% of defects returning to equilibrium sites for Ga and N Primary Knock-on Atoms (PKAs), respectively. In contrast, this recrystallization is around 50% for Si PKAs in Si and Ge PKAs in Ge. This enhanced recrystallization in GaN is attributed to the compact nature of the wurtzite structure, where the atoms surrounding the displaced atoms act as a barrier for their diffusion.

3.2 State of the Art on Collision Cascades in GaN and Other Semiconductors

The field of radiation effects in materials has been extensively explored over the past decades, with a particular focus on well-known semiconductors such as Si and Ge. Driven by growing interest in its unique properties, a significant number of studies on GaN have emerged. However, several questions remain open, particularly concerning its radiation resistance. In this section, we review the main studies addressing this topic, identifying their major contributions and limitations.

In recent years, aiming at improving the efficiency of power and radio-frequency Si-based devices, interest has grown for GaN, which exhibits remarkable properties [1] for these applications, such as a large band gap of 3.4 eV compared to 1.1 eV in Si, a high breakdown field of 3.3 MV/cm, compared to 0.3 MV/cm in Si. GaN also shows a remarkable temperature resistance [2]. Some studies reported that GaN devices can be very sensitive to DD, indeed [3–5] show significant degradation of the electrical characteristics of AlGaIn/GaN HEMT for irradiations, respectively, with neutrons and Au⁴⁺ ions at different fluences. However, the majority of studies investigating the response of

GaN devices to DD have observed low sensitivity of the devices [6] and even improved electrical characteristics on an AlGaIn/GaN HEMT under electrical stress.

At the material level, the few studies conducted have proposed that the resistance of the devices could find its origin in the intrinsic properties of the GaN material. Atomic scale simulations of displacement cascades can then bring an in-depth understanding of phenomena at stake. In [7, 8], Nord *et al.* used MD to investigate the accumulation of damage during ion beam irradiation of GaN. Collision cascades initiated by Ga and N PKA between 200 eV and 10 keV are simulated. The findings revealed that few thermally equilibrated defects are created in GaN. Furthermore, the number of defects created in the GaN increases with temperature. At 10 K, the average number of primary defects per PKA was 5.5, while at 900 K it increased to 38.5. These defects include gallium and nitrogen vacancies and interstitials, with gallium vacancies being more likely to form than nitrogen vacancies. For example at 300 K, the probability of creating a gallium vacancy was about 2.5 times higher than that of a nitrogen vacancy. Overall this study indicates that temperature significantly influences the creation of primary defects in GaN.

Chen *et al.* have also performed MD simulations [9] with Ga PKAs ranging from a few hundreds of eV to 40 keV. They observed a large number of atoms displaced during the defect peak of collision cascades, followed by a self-healing within the cascades, resulting in a small quantity of defects remaining only 20 ps after the beginning of the cascade. This drastic picosecond scale in-cascade self-healing observed in GaN is similar to what can be observed in metals, and contrasts sharply with the longer timescales of defect recombination in materials such as Si, Ge, or GaAs [10]. This self-healing has also been observed very recently, both in MD simulations and via transmission electron microscopy (TEM), in the case of defects created following Swift Heavy Ion (SHI) irradiation [11].

However, it has never been experimentally observed for collision cascades. Actually, there are very few TEM studies devoted to the structural analysis of collision cascades in semiconductors [12, 13], especially in GaN. Indeed, if the ion tracks produced by SHI irradiation are not large enough to be imaged [11], due to the inherent thickness of the samples, the color contrast difference due to small clusters of defects produced in collision cascades are hard to identify even in high resolution TEM images. It is to attain this atomic scale description necessary to investigate the presumed intrinsic resistance of GaN material to DD that we employ MD simulations.

To our knowledge, only one study has considered N PKAs [7] in GaN, though N PKAs form a significant part of the created PKAs following neutron irradiation [14]. In the published literature on GaN collision cascades, a detailed analysis of the dynamics of the cascades in terms of defect creation and clustering is also lacking. Moreover, most studies do not include statistical studies, as collision cascades are very random events and it is important to study a large number of events. As highlighted in [15], studying a large number of events is essential. Therefore, we study collision cascades in GaN initiated with both Ga and N PKAs based on a larger number of simulations than previously done at three energy levels: 1 keV, 10 keV and 25 keV. Cascade dynamics are closely tracked

and analyzed. Additionally, to comprehensively assess the relative sensitivity of GaN to non-ionizing radiation compared to other standard microelectronic materials, results obtained in GaN are compared to those obtained in Si and Ge.

The work conducted in this chapter is part of a larger effort to increase the fidelity of our understanding of DD effects, bridging atomic-scale modeling and experimental findings with device-level observations. The methodology employed for achieving this has already been extensively described and applied to Si [16–19] and to some extent to Ge and Si-Ge alloys [20, 21].

3.3 Preliminary Analysis and Neutron-Displacement Damage Cross Section of GaN

The first step of our study focused on a preliminary parametric analysis using the Monte Carlo (MC) method. Indeed, it is crucial to properly prepare and optimize the parameters of MD simulations to ensure that the simulations are neither too long nor overly computationally intensive.

3.3.1 Introductory Investigations

In MD, the number of atoms is proportional to the volume of the simulation box. A larger number of atoms results in more equations of motion to solve and potentially more data to write in the outputs, which can lead to significantly larger output files. It is therefore necessary to optimise the size of the simulation box according to the material and energy being studied. The box must be large enough to fully contain the cascade while preventing atoms from escaping the inner part of the box. For more details, refer to Section 2.4.3 of Chapter 2. One key parameter that can be used to estimate the size of the collision cascade is the penetration depth, *i.e.*, the distance traveled by highly energetic atoms during the collision cascade. This is often the primary knock-on atom (PKA), although in very rare cases, it may be a secondary knock-on atom (SKA). Accordingly, the size of the simulation box is selected to be proportional to the penetration depth of the PKA within the material.

To estimate the penetration depth of PKAs in GaN, Si, and Ge for the three studied energies: 1 keV, 10 keV, and 25 keV, we then used TRIM. SRIM tables provide “projected range”, while TRIM provides trajectories and longitudinal range (see Figure 3.1).

Based on these values, it is possible to estimate the penetration depth of the PKA and, consequently, to select appropriately sized simulation boxes. This penetration depth depends on the material and the type of PKA used, in GaN, N PKAs tend to travel further than a Ga PKAs because N atoms are lighter than Ga. For each energy, a margin, of a certain number of angstroms chosen according to the energy of the PKA, is added in order to contain certain cascades whose PKA penetration depth exceeds the average found, *i.e.*,

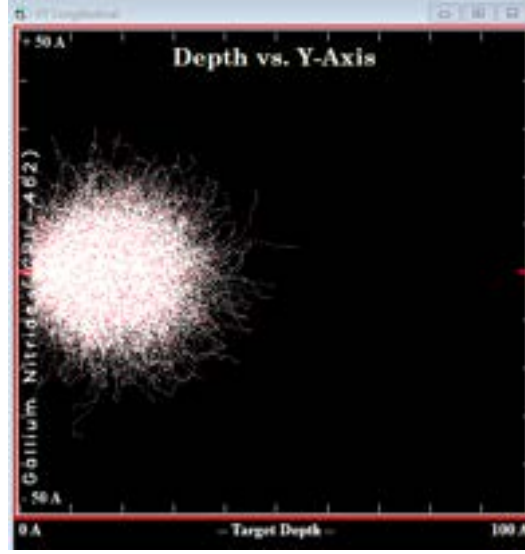


Figure 3.1: Program window TRIM showing the trajectories of 10,000 Ga in GaN, along with the dimensions of the GaN box.

the extreme cases. For collision cascades of 1 keV, the penetration depths being lower, the simulation boxes are 150 Å for the Ga and Ge PKAs and 200 Å for the N and Si PKAs. For 10 keV collision cascades, the penetration depth values range from 65 Å to 181 Å, and the simulation box sizes are 300 Å for Ga and Ge PKAs, 434 Å for Si PKAs and 600 Å for N PKAs. Finally, for cascades of 25 keV collisions, the box sizes are 500 Å for Ga PKAs, 534 Å for Ge PKAs and 1000 Å for Si and N PKAs. In addition to preparing the molecular dynamics study, data obtained with SRIM/TRIM can also serve as comparisons with those obtained via MD, notably regarding the average number of defects remaining after collision cascades (see Section 3.4.3.1).

3.3.2 Neutron Displacement Damage Cross Section in GaN

We also used the MC method to study the neutron displacement damage cross-section in GaN with SRIM/TRIM and GEANT4. Experimenters use NIEL (Non-Ionizing Energy Loss) curves for various materials and particles to evaluate the effects of displacement damage across different irradiation platforms. This helps determine whether an equivalence exists between the effects of different particle types [22]. In the absence of data specific to GaN device technology, researchers are using the well-established silicon data [23], [24], either out of habit, convenience, or lack of alternatives. However, this approach is not ideal, as neutron–nuclear interaction cross-sections can vary significantly between materials. Our complete results are presented in this article [14]. This approach quantifies the NIEL during neutron–GaN interaction. More specifically, as shown in studies [25, 26], the formula is:

$$D(E_n) = \sum_R \int_0^\infty E_r \cdot n(R, E_r) \cdot \frac{d\sigma_R(E_n, E_r)}{dE_r} dE_r, \quad (3.1)$$

where $D(E_n)$ is the displacement damage cross-section expressed in $(\text{MeV} \cdot \text{mb})$, E_n is the incident neutron energy in MeV, R is the type of secondary particle (PKA), E_r is the recoil particle energy expressed in MeV, and $n(R, E_r)$ is the energy partition function of the recoil particle as a function of E_r . The two main parameters are as follows:

- **Production Cross Sections:** can be estimated through the study of secondary particles from the neutron–atom interaction.
- **Energy Partition Function:** defines the part of energy transferred into displacement damage or equivalently the displacement energy:

$$E_{\text{displacement}} = E_r \times n(R, E_r). \quad (3.2)$$

It is thus possible to calculate the energy distribution function using different methods, which we present in the following subsections.

3.3.2.1 Lindhard–Robinson Method

The Lindhard–Robinson (LR) model is one of four methods we examined to estimate the energy partition function. This model uses the formula:

$$LR(E_r) = \frac{1}{1 + F_L (3.4008\epsilon^{1/6} + 0.40244\epsilon^{3/4} + \epsilon)}, \quad (3.3)$$

where:

$$\epsilon = \frac{E_r}{E_L}, \quad E_L = 30.724 \frac{Z_R Z_L}{Z_R^{2/3} + Z_L^{2/3}} \frac{A_R + A_L}{A_L}, \quad (3.4)$$

and:

$$F_L = 0.0793 \frac{Z_R^{2/3} Z_L^{1/2} (A_R + A_L)^{3/2}}{(Z_R^{2/3} + Z_L^{2/3})^{3/4} A_R^{3/2} A_L^{1/2}}. \quad (3.5)$$

The Lindhard model applies to ion energies below $(24.8 \times Z^{4/3} \times A[\text{keV}])$, which corresponds to ~ 4.6 MeV for N and ~ 170 MeV for Ga . Note that this formula applies only to monatomic systems.

3.3.2.2 Threshold Displacement Energy Method

The second type of formula, referred to as " LT_{Ed} ", builds upon the original Robinson formula by incorporating the Kinchin–Pease [27] approach to account for the threshold energy required for lattice displacement, known as the displacement threshold energy (E_d).

$$LT_{Ed}(E_r) = \begin{cases} 0, & \text{si } E_r < E_d, \\ 0.23 \left(\frac{E_r - E_d}{E_d} \right) LR(E_r), & \text{si } E_d \leq E_r < 2 \cdot E_d^{0.8} \\ LR(E_r), & \text{si } E_r \geq 2 \cdot E_d^{0.8} \end{cases} \quad (3.6)$$

This formula is almost the same as the one described in [28]. In our case, between E_d and $(2 \cdot E_d)/0.8$, we neglect the energy transmitted to the electrons. As illustrated in the following figures, for this study, this approximation has little significant influence on the results. It gives good results for silicon even if improvements are still in progress for electron irradiations [29].

3.3.2.3 SRIM/TRIM Method

The third method is based on the SRIM database. The displacement energy is estimated by integrating the nuclear stopping power for each ion (Z) type in a target material (Si or GaN for this study). This method uses a binary collision approximation (BCA).

The fourth method is based on the transport of ions in matter (TRIM) program included in the SRIM software. This Monte Carlo tool allows obtaining precise data on the course of the collision cascades. With a significant number of Monte Carlo events, it is possible to obtain the average percentage of recoil energy.

For this study, simulations were performed for ions from $Z = 1$ to $Z = 32$ at energies ranging from a few electronvolts to 100 MeV (or up to 1 GeV for some ions, depending on the energy of the secondary particles in n-GaN). The layer thickness of gallium nitride was adapted to the PKA range. We observed a stabilization of the data around 4000 simulations, leading to accurate results.

Thus, 4000 ion-runs were performed for each ion type and each energy level. The calculation method “detailed calculation with full damage cascades” was used. This method, although slower than the “ion distribution and quick calculation of damage” option (which provides the SRIM database results), accounts for every collision of the recoil particle until the energy drops below the lower energy thresholds.

For the energy partitioning, the two methods give the same result. However, for the defect number estimation, it has been demonstrated that the full cascade option is less accurate than the quick calculation [30].

3.3.2.4 Non-Ionising Energy Loss

The NIEL values resulting from the different methods for calculating the energy distribution function are available in Figure 3.2. A striking point can be observed: The Non-Ionizing Energy Loss (NIEL) values of Si are larger than those of GaN between ~ 0.1 and ~ 10 MeV.

Using Si data for GaN components results in underestimated displacement levels: between 0.1 and 10 MeV, the error is less than 100%; between 100 eV and 100 keV, the error is roughly one order of magnitude; between 10 MeV and 1 GeV, the error varies between two and ten; below 10 eV, the error is approximately two orders of magnitude. We strongly recommend using the NIEL *n*-GaN values instead of those for Si when characterizing

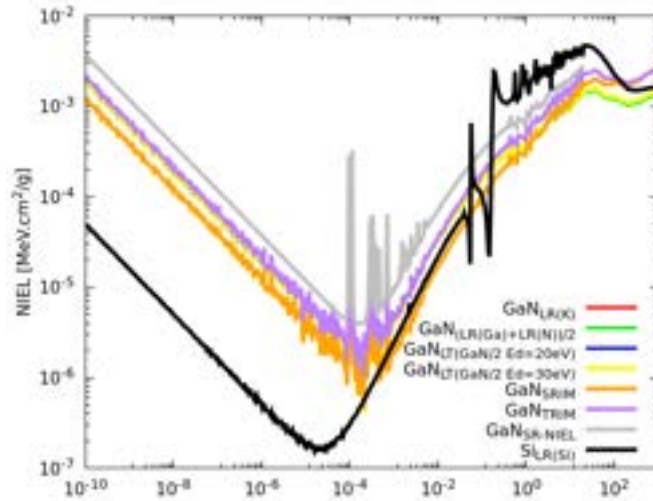


Figure 3.2: NIEL data calculated in Si and GaN [14].

displacement effects in GaN components.

3.3.2.5 PKA distributions to DD

An important piece of information to collect is the type of PKA created depending on the energy of the incident neutrons. These data are illustrated in Figure 3.3 for GaN and Figure 3.4 for Si.

For GaN, the contributions of Primary Knock-on Atoms (PKAs) varies depending on the energy range:

1. **Below 10 eV:** The C ion is the primary contributor, followed by H. These ions originate from the $n + {}^{14}\text{N} \rightarrow p + {}^{14}\text{C}$ reaction.
2. **Between ~ 1 and 100 keV:** The N ion contributes more than 70% and Ga is the second contributor.
3. **Around 1 MeV:** The contributions of N and Ga ions are nearly equal.
4. **Around 10 MeV:** The Ga ion contributes more than 70%, followed by N.
5. **Near 1 GeV:** Heavy ions (e.g., Ga, Zn, Cu, Ni, Co, Fe, Mn, Cr, V, Ti, Sc, Ca, K) dominate, while lighter ions ($Z < 7$) contribute minimally.

The PKA contributions differ significantly between n-Si and n-GaN:

- For silicon, the Si PKA dominates across most of the energy range.
- For GaN, multiple PKA types with varying masses must be considered, with lighter ions such as N and C differing from heavier ions like Ga and Zn.

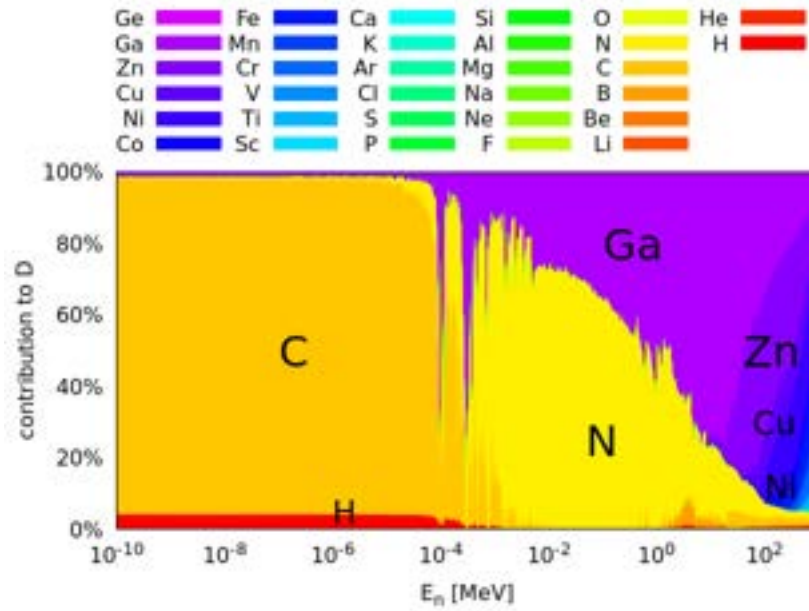


Figure 3.3: PKA contributions to the n-GaN displacement damage cross-section (with TRIM energy partition function)[14].

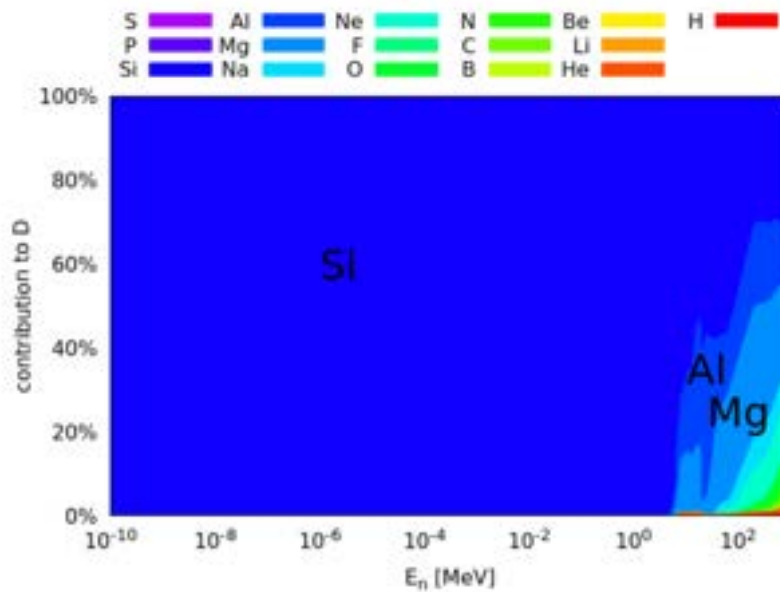


Figure 3.4: PKA contributions to the n-Si displacement damage cross-section (with TRIM energy partition function)[14].

As observed in SiGe [20], it is likely that light and heavy PKAs exhibit different responses.

The results of this section demonstrate that, unlike in silicon (Si), the contributions of primary knock-on atoms (PKAs) in gallium nitride (GaN) varies significantly with energy. At very low energies, below 10 eV, carbon (C) is the dominant PKA. In the intermediate energy range, between approximately 1 and 100 keV, nitrogen (N) becomes the primary PKA. At medium energies, gallium (Ga) takes precedence as the dominant contributor. At higher energies, a mixture of heavy ions contributes significantly to the PKA distribution, reflecting a more complex dynamic at elevated energy levels.

3.4 Collisions cascade and resulting displacement damage in GaN, Si and Ge

Once the parametric study is completed, we examine the dynamics of collision cascades and defects using MD. Through MD simulations of collision cascades, we want to accurately simulate the ballistic aspects of the cascades, and also the structure and global properties of the material, since they have a major influence on the collision cascade, and on the resulting state of damage [31]. This is what makes MD more complete than the Binary Collision Approximation (BCA), in which only ballistic aspects are considered. For this purpose, 100 different directions, *i.e.*, collision cascades, are studied in GaN, as well as in Si and Ge for comparative purposes, as these materials have existing studies on this topic.

3.4.1 Computational details

As described in Chapter 2, for the sake of simulating collision cascades as rigorously as possible, an interatomic potential, calibrated according to experimental data, and able to reproduce at the same time general equilibrium properties of the material, such as structure, cohesive energy, melting temperature among other properties, and highly nonequilibrium high energy ion-ion collisions must be employed. In previous studies focused on Si [17], [21], the Stillinger-Weber (SW) potential was used. However, for GaN, its use was very limited and confined to structural studies [32]. Given that our objective is to compare the results obtained for GaN, Si and Ge starting from the same theoretical grounds, we choose to employ Tersoff potentials coupled to repulsive ZBL potentials [33] for Si [34], [35], GaN [7], [8], [9] and Ge [36]. For Ge, we derived ourselves the parameters ensuring a smooth transition between the ZBL and Tersoff potentials. The Fermi function parameters we employed for Ge are $r_F = 0.97 \text{ \AA}$ and $b_F = 10.0 \text{ \AA}^{-1}$. More details are given in Section 2.4.3.2 of Chapter 2.

Before presenting all the parameters guiding our simulations, it is important to mention that this work stems from a large number of tests conducted on each material, including some that were not successful, such as the integration of non-adiabatic electronic effects using the Two-Temperature Model [37]. This model describes the interaction between electrons and the atomic lattice in a material, assuming that the electrons and the lattice have distinct temperatures that evolve differently over time due to their thermal coupling and respective heat capacities. Unfortunately, using this model for the GaN wurtzite structure posed challenges. It is necessary to include nonadiabatic electronic effects to have a complete picture of the process involved in the collision cascade, we then opted to use an available command within LAMMPS [38] in our simulations. It incorporates the electronic stopping power by the insertion of a friction force to the Newton's equation of motion.

Our MD collision cascade simulations take place in boxes created from non-primitive orthorhombic unit cells composed of 8 sites (4 Ga and 4 N) for which the lattice parameters

are $a = 3.18 \text{ \AA}$, $b = 5.52 \text{ \AA}$ and $c = 5.17 \text{ \AA}$. Positions of atoms are presented in Table 3.1

Atom type	x	y	z
Ga	0	1.86	0
Ga	0	0	2.62
Ga	1.61	4.65	0
Ga	1.61	2.79	2.62
N	0	1.86	1.97
N	0	0	4.59
N	1.61	4.65	1.97
N	1.61	2.79	4.59

Table 3.1: Positions of Ga and N atoms in the GaN unit cell.

To create the Si and Ge simulation boxes, we use a diamond unit cell composed of 8 atoms and for which the lattice parameters are $a_{Si} = 5.43 \text{ \AA}$ and $a_{Ge} = 5.66 \text{ \AA}$. Different types of PKAs are employed (both Ga and N in GaN, Si in Si, Ge in Ge), with energies of 1, 10 and 25 keV. We chose these energies because they correspond to those studied in the state of the art, but also because they remain reasonable for the simulations. However energies of 25 keV marks the point where the energy starts generating significantly large outputs. As the energy increases, the cascade grows larger, resulting in a larger simulation box, more atoms, and ultimately higher output levels. This has become our limiting factor, and as a result, we do not go beyond 25 keV.

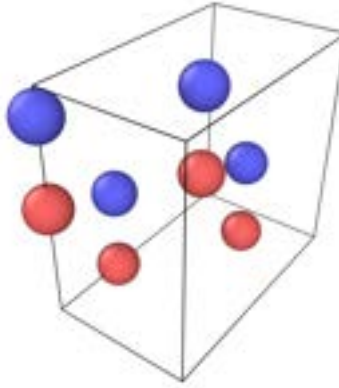


Figure 3.5: MD input file corresponding to the initial mesh of GaN, visualised using the Ovito software [39]. Ga atoms are red and N atoms are blue.

Figure 3.5 illustrates the modeling of the GaN system using visualization software. We can see gallium atoms (in red) and nitrogen atoms (in blue), as well as the simulation box (the outlined area). This is the basic "brick" with which the simulation box is built, simply by duplicating it along the x, y and z axes. Due to the large difference in the size of the cascades depending on the PKA types, we use simulation boxes of different sizes according to results obtained with TRIM, see Section 3.3.1. For 1 keV PKAs, box sidelengths range

from 150 Å to 200 Å, *i.e.*, from 294 408 to 659 680 atoms, for 10 keV PKAs, box sidelengths range from 300 Å to 600 Å, *i.e.*, from 2 398 880 to 19 016 576 atoms, for 25 keV PKAs, boxes sidelengths range from 400 Å to 1000 Å, *i.e.*, from 4 096 000 to 88 031 160 atoms. The system is equilibrated for 20 ps at 300 K with a timestep of 1 fs before the initiation of the collision cascade. Collision cascades are started by attributing to an atom, chosen as the PKA, a certain velocity vector corresponding to the desired PKA energy.

For collision cascades initiated at 1 keV, the primary knock-on atom (PKA) is positioned at the center of the simulation box. At higher energies, the size of the cascade depends on the type of PKA, necessitating adjustments to its position. For energies of 10 keV and 25 keV, Ga and Ge PKAs can still be placed at the center of the box since the resulting cascades remain contained. In contrast, the positions of N and Si PKAs need to be optimized based on the direction of their initial velocity vectors to ensure PKAs do not leave the simulation box. For each PKA type and each energy, 100 simulations are run, each one with a different direction in order to obtain statistically relevant results [15]. The timestep is chosen based on the distance covered by the PKA between two timesteps, which does not exceed 0.025 Å in our simulations.

Additional detail about the chosen integration ensembles and thermostat can be found in Section 2.4.2.3 of Chapter 2. The maximum penetration depth of the PKA, the number of created defects and the spatial distribution, diffusion and clustering of defects are analyzed. The number of defects is defined as the number of Frenkel pairs (number of interstitial-vacancy pairs created). There exists different methods for counting defects, for example the Lindemann criterion [40], previously used [20]. For Si and Ge materials, the Lindemann and Wigner-Seitz methods are known to give different absolute results but to scale very well [31]. In this article, we chose to calculate the number of defects with the Wigner-Seitz criterion [41], implemented in OVITO. Data processing is performed using OVITO visualization software and its analysis tools [39].

3.4.2 Methodological Insights

To fully understand the various terms used throughout the description and interpretation of the results, it is necessary to clarify certain points, such as the definition of the maximum penetration depth, why it was chosen, and the method used to count defects.

3.4.2.1 Defect Quantification Using Wigner-Seitz Method

The Wigner-Seitz method, illustrated in Figure 3.6, involves analyzing defects in a material by associating each crystalline site with a geometric cell called the Wigner-Seitz cell, defined by the median planes between a given site and its nearest neighbors. It is necessary to define the size of a cell to proceed with defect counting. By comparing the lattice in its initial state, *i.e.*, before the cascade, with its state at the end of the simulation, misoccupied cells can be identified: those that are empty correspond to vacancies, while those containing multiple atoms indicate interstitials. In materials composed of multiple types of atoms, it is possible to associate a cell with a specific type of atom to identify

antisites. This method allows for precise localization and quantification of defects, but it requires detailed atomic position data, which can be readily obtained through MD.

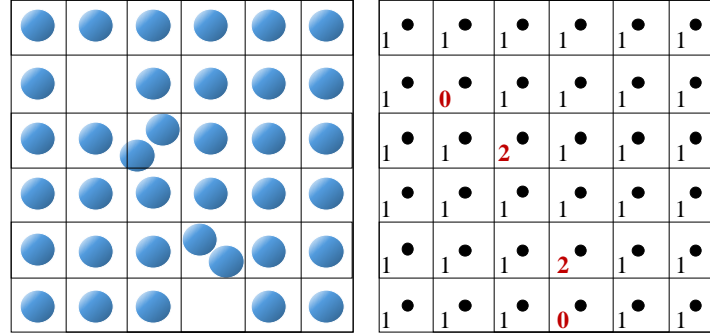


Figure 3.6: Schematic representation of the lattice created from Wigner-Seitz cells at the end of a cascade, with visible atoms (left) and the count of atoms within the cells (right). The number 1 indicates an atom on its equilibrium site (no defect), 0 indicates the absence of an atom in the cell (vacancy), and 2 indicates the presence of two atoms in a cell (hence, one interstitial atom).

3.4.2.2 Understanding Maximum Penetration Depth

Figure 3.7 schematically illustrates the different distances traveled by the PKA. It shows:

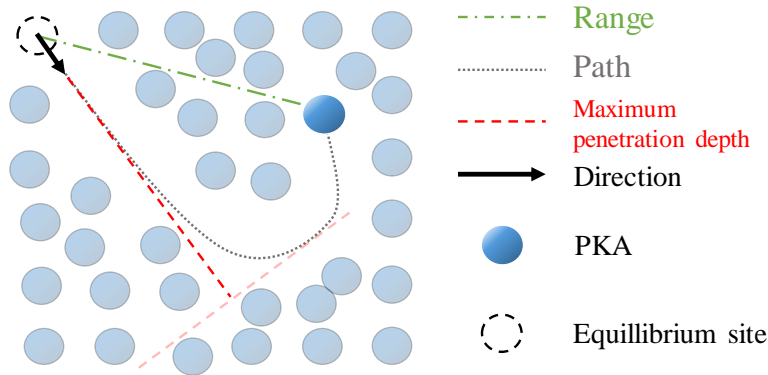


Figure 3.7: Schematic representation of the range, path, and maximum penetration depth at the end of a cascade.

- The range, which represents the distance between the equilibrium site of the PKA and its final position.
- The path, which corresponds to the trajectory of the PKA at each timestep of the simulation.

- The maximum penetration depth which represents the distance between the equilibrium site of the PKA and the farthest point on its trajectory along its initial direction.

The choice to study the maximum penetration depth was motivated by the need for comparison with TRIM and supported by observations of the trajectories of nitrogen in GaN, which can sometimes undergo drastic changes in direction.

3.4.3 Results & Discussion

Considering that a quantitative comparison of our results with experimental results is difficult to achieve, in the following, our results are compared with simulations performed with the Transport and Range of Ions in Matter (TRIM) program [33], which is part of the Stopping and Range of Ions in Matter (SRIM) tool. TRIM simulations are based on the BCA, and matter is described as a continuous medium. Therefore, certain effects that can be captured with MD (for example temperature influences), and structure related information (clustering of defects for example) are not accessible with TRIM. Therefore, all our results cannot be compared to TRIM. However, extensive calibration and comparison of TRIM/SRIM with experimental stopping power and ion range results makes it a trustworthy comparison point and a reliable reference for MD simulations, especially for the range of the ions in matter, which are compared to the maximum penetration depth we report.

For all the studied materials, and all the investigated energies, cascades are simulated for 22.6 ps. In the following, the term "end" refers to the material structure at the end of the simulations, *i.e.*, after 22.6 ps. The peak of the cascade designates the moment of the simulation at which the maximum number of defects is attained. The number of defects represents the number of interstitial-vacancy pairs. The size of a cluster designates the number of vacancies, interstitials and/or antisites (for GaN only) it contains. Two constituents (interstitials, vacancies or antisites) belong to the same cluster if they are separated by less than twice the nearest neighbor distance. In this section, results for all energies are included in Table 3.2 and 3.3 but for the sake of conciseness, only graphs with PKAs of 10 keV are shown here. Graphs for the other studied PKA energies, *i.e.*, 1 keV and 25 keV, are given in appendices.

3.4.3.1 State of damage at the end of the simulations

Figure 3.8 shows the maximum penetration depth distribution of PKAs at 10 keV for Ga and N PKAs in GaN, Si PKAs in Si and Ge PKAs in Ge based on 100 MD simulations for each case. The average values of both the maximum penetration depth and the number of defects for 10 keV cascades are summarized in Table 3.2, alongside the average values for 1 keV and 25 keV cascades as well.

Following Figure 3.8, for Ga PKAs in GaN, the penetration depth distribution is very homogeneous, with more than 90% of the simulated cascades having a depth between 10

and 100 Å. On the contrary, for N PKAs, the distribution seems very dispersed, ranging from a few Å to more than 400 Å, with an average depth of 234 Å, much deeper than that of Ga PKAs (56 Å). In agreement with our previous studies on the subject, Si PKAs penetrate deeper than Ge PKAs [20]. Figure 3.8 reveals that Si PKAs also penetrate a lot deeper than Ga PKAs, but far less than N PKAs. Ge and Ga PKAs display a similar distribution of their range of penetration.

The average values of Table 3.2 show that the same trend can be observed at 1 keV and 25 keV. This is also confirmed by figures A.1 and A.2, showing the same data as Figure 3.8 but for 1 keV and 25 keV PKAs. These wide differences in penetration can be explained by the difference in terms of mass and size of PKA but also in terms of disparities in the density of each materials, *i.e.*, $\rho_{\text{GaN}} = 6.15 \text{ g/cm}^3$, $\rho_{\text{Si}} = 2.33 \text{ g/cm}^3$ and $\rho_{\text{Ge}} = 5.32 \text{ g/cm}^3$.

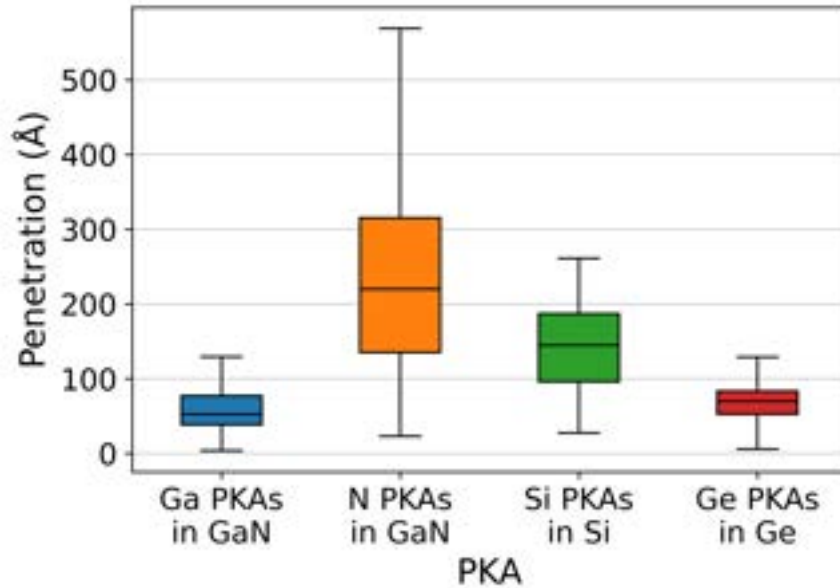


Figure 3.8: Box plots of the maximum penetration depth of Ga PKAs in GaN (blue), N PKAs in GaN (orange), Si PKAs in Si (green) and Ge PKAs in Ge (red) for 10 keV collision cascades. From lowest to highest, the horizontal lines of a box plot represent the minimum value of the set, the first quartile value, the median, the third quartile, and the maximum value of the set.

Figure 3.9 shows the distribution of the number of defects obtained at the end of simulations of 10 keV collision cascades initiated by Ga and N PKAs in GaN, Si PKAs in Si and Ge PKAs in Ge. Large differences between the three materials can be also observed here.

The distributions of the number of defects in GaN are considerably lower than in Si and Ge: between 30 and 60 for Ga PKAs in GaN, 20 and 50 for N PKAs in GaN compared to between 150 and 230 for Si PKAs in Si and between 180 and 320 for Ge PKAs in Ge. The drastic difference between the three materials is made even clearer in Table 3.2: the mean

3.4. Collisions cascade and resulting displacement damage in GaN, Si and Ge

Table 3.2: Comparison table of average maximum penetration depth and average number of defects after 1 keV, 10 keV and 25 keV collision cascades initiated by Ga PKAs in GaN, N PKAs in GaN, Si PKAs in Si and Ge PKAs in PKA. Standard deviations are shown in parenthesis. TRIM displacement energy thresholds are : Ed_{Ga} : 25 eV, Ed_N : 28 eV, Ed_{Si} : 15 eV, Ed_{Ge} : 15 eV.

Energy	Data	Method	Ga	N	Si	Ge
5*1 keV	2*Penetration depth (Å)	MD	20 (8)	26 (15)	29 (16)	22 (12)
		TRIM	19	30	36	23
	2*Interstitials	MD	5 (2)	4 (2)	22 (3)	22 (3)
		TRIM	12	9	19	22
5*10 keV	2*Penetration depth (Å)	MD	65 (32)	177 (106)	133 (38)	65 (40)
		TRIM	63	180	181	84
	2*Interstitials	MD	42 (7)	36 (8)	185 (18)	243 (35)
		TRIM	116	84	171	208
5*25 keV	2*Penetration depth (Å)	MD	112 (55)	413 (183)	323 (140)	129 (56)
		TRIM	118	393	402	160
	2*Interstitials	MD	105 (11)	71 (12)	403 (45)	640 (106)
		TRIM	281	178	384	502

number of defects in Ge (243) and Si (185) is about five times and four times that in GaN for Ga and N PKAs (42 and 36 respectively).

In addition to the observed discrepancies, it is also striking that cascades initiated by Ga PKAs and N PKAs tend to generate very similar numbers of defects (mean values of 45 for Ga PKAs and 36 for N PKAs). Indeed, previous studies showed that the numbers of defects after a collision cascade in binary materials can vary greatly depending on the type of PKA, notably in Si-Ge alloys [20, 42].

In appendices, figures A.3 and A.4 which show the box plots of the number of defects for 1 keV and 25 keV cascades confirm the trends derived from Figure 3.9. Also, at all the considered energies, Ga and N PKAs tend to generate very similar numbers of defects.

To analyze in more detail the created defects in GaN, Table 3.3 displays for all the considered PKA energies the average number of each defect type (interstitial, vacancy, antisite), as a function of the atom type. At all energies, antisites are the minority defects. We find no clear trends regarding the dominance of Ga interstitials or N interstitials (or vacancies). Indeed, we observe that for N PKAs, at 1 keV and 10 keV, more Ga interstitials are created, whereas the inverse is observed for Ga PKAs at all energies. Also, at 10 keV and 25 keV, regardless of the PKA type, there are more Ga vacancies.

Alongside the mean values derived from MD, Table 3.2 contains the average maximum

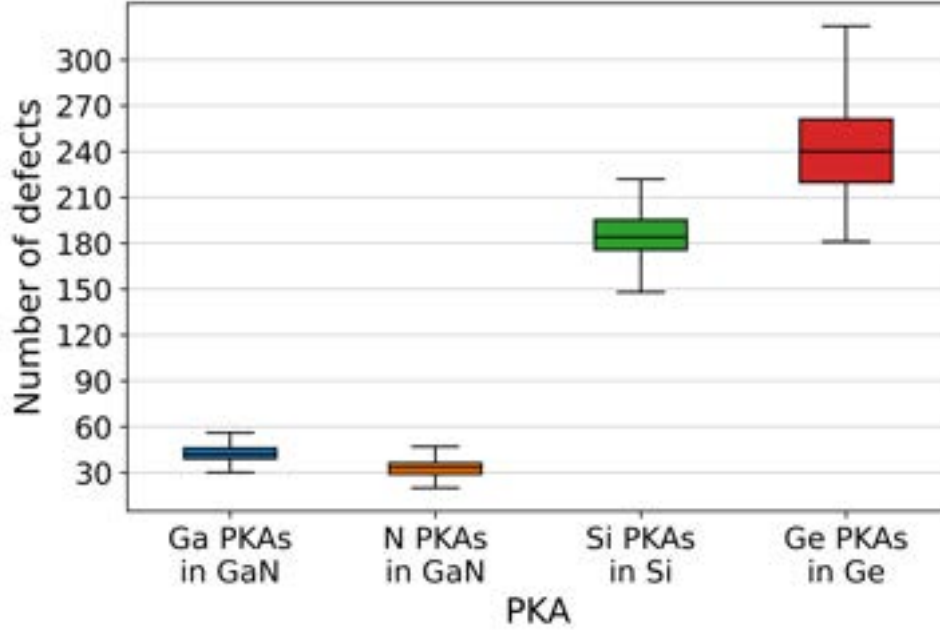


Figure 3.9: Box plots of the number of defects after 10 keV collision cascades initiated by Ga PKAs in GaN (blue), N PKAs in GaN (orange), Si PKAs in Si (in green) and Ge PKAs in Ge (in red). From lowest to highest, the horizontal lines of a box plot represent the minimum value of the set, the first quartile value, the median, the third quartile, and the maximum value of the set. One hundred simulations are run for each type of PKA.

penetration depth and average number of defects obtained from TRIM after 1 keV, 10 keV and 25 keV collision cascades initiated by Ga and N PKAs in GaN, Si PKAs in Si and Ge PKAs in Ge. The averages obtained using TRIM are calculated based on the results of 5000 simulations. Absolute values of penetration depth are in very good agreement between MD and TRIM for Ga and Ge PKA. For N and Si PKA penetration depths, quite important discrepancies are observed (about 50 Å). The trends identified with MD are verified with TRIM, except in the case of Si and N PKAs, for which MD predicts a 40 Å discrepancy at 10 keV between the two mean penetration depth values, whereas TRIM predicts nearly no difference between the two, whatever the energy.

Concerning the total number of defects, the absolute values are hardly comparable between the two methods. Indeed, both methods are so different in their nature, that the values given by the method for counting defects in both cases cannot really be set side by side.

However, the trends in the evolution in the number of defects depending on the PKA types and materials can be analyzed and compared. On the whole, for all energies, the average number of defects globally follows the same trends between the two simulation methods, a Si PKA in Si or a Ge PKA in Ge generates more defects than Ga and N PKAs in GaN, with slightly more defects in GaN in a collision cascade initiated by a Ga PKA. In

Table 3.3: Per atom type average number of interstitials (I_{Ga} and I_{N}), vacancies (V_{Ga} and V_{N}) and antisites (Ga_{N} and N_{Ga}) in 1 keV, 10 keV and 25 keV GaN collision cascades initiated with N and Ga PKAs. Standard deviations are given in parenthesis.

	I_{Ga}	I_{N}	V_{Ga}	V_{N}	Ga_{N}	N_{Ga}
<i>N PKA in GaN</i>						
1 keV	2 (1)	2 (1)	2 (1)	2 (1)	1 (1)	1 (1)
10 keV	19 (4)	18 (4)	21 (4)	15 (4)	5 (3)	3 (2)
25 keV	33 (12)	36 (13)	42 (12)	27 (13)	10 (5)	7 (4)
<i>Ga PKA in GaN</i>						
1 keV	2 (1)	4 (1)	1 (1)	5 (1)	2 (1)	0 (1)
10 keV	20 (4)	23 (4)	23 (4)	19 (4)	8 (2)	6 (2)
25 keV	47 (6)	59 (9)	57 (6)	49 (8)	18 (4)	13 (4)

more detail, with MD, at 10 keV it is observed that about 5 times fewer defects are created by a Ga PKA in GaN and a N PKA in GaN than a Si PKA in Si and about 6 times fewer defects created than a Ge PKA in Ge.

With TRIM, at 10 keV, only about 2 times fewer defects are observed for Ga and N PKAs in GaN compared to Si and Ge. The trends thus are not completely similar, as TRIM tends to overestimate the number of defects created in GaN and underestimates the number of defects in Si and Ge compared to MD simulations. The reasons for this underestimation will be discussed in Section 3.4.3.3.

3.4.3.2 Collision cascade dynamics and clustering

We focused in the previous paragraph on the final state of the cascades only, but MD allows us to explore not only static pictures but also the dynamic evolution of the cascades. Figure 3.10 shows the evolution of the number of defects over the entire MD simulation time, for 10 keV collision cascades initiated by Ga and N PKAs in GaN, Si PKAs in Si and Ge PKAs in Ge. Each data point in Figure 3.10 results from an average over the 100 performed MD simulations.

A collision cascade can be divided in multiple steps. First, the ballistic phase occurs, during which fast moving Secondary Knock-On Atoms (SKAs) are created following collisions with the PKA. Those SKAs then create slow moving atoms and defects in the materials. Those steps correspond to the increasing part of Figure 3.10.

After a peak at which the maximum number of defects is reached, heat excess is evacuated and the material starts to recrystallize/heal. This step is sometimes also called annealing. In all four cases, the cascades reach their maximum number of defects after a few tenths of a picosecond. The peak is reached more quickly in Si cascades (0.25 ps), then a little bit later for the N in GaN PKAs (0.30 ps) and the Ge in Ge PKAs (0.38 ps), and after-

wards for the Ga in GaN PKAs (0.43 ps). However, we observe very distinct behaviours in terms of the evolution of the number of defects between the different materials and PKAs.

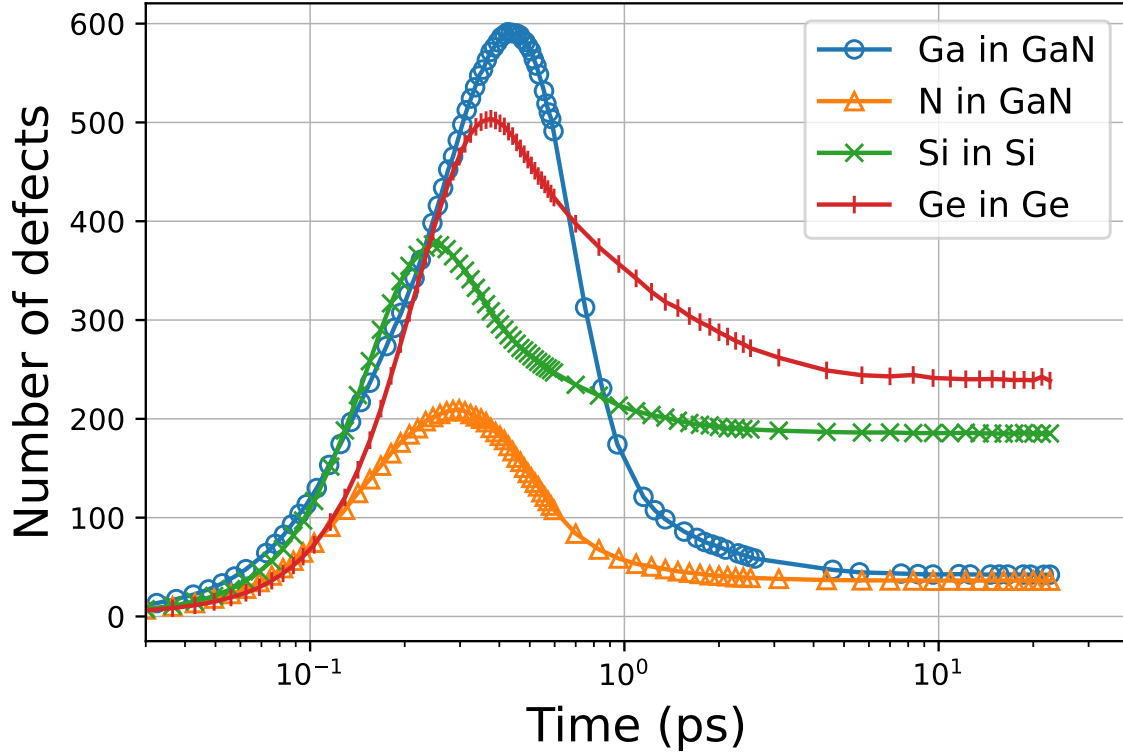


Figure 3.10: Defects number evolution profile during 22.6 ps for 10 keV collision cascades initiated by Ga PKAs in GaN (blue o), N PKAs in GaN (orange Δ), Si PKAs in Si (green x) and Ge PKAs in Ge (red |). Defect data are derived from averaging results across 100 simulations for each respective case.

For 10 keV cascades, in GaN, the N PKAs produce cascades with a peak of less than 200 defects, in contrast to the Ga PKAs cascades which have a considerably higher peak of more than 575 defects. At the end of the simulations, the number of defects at 10 keV is only about 50 in Ga PKAs cascades, compared with 575 at the peak of those same cascades, *i.e.*, a reduction of 93%. For N PKAs, the reduction is 83% (from 208 to 36 defects). In GaN, cascades initiated by both Ga PKAs and N PKAs tend to almost entirely heal on their own.

In Si, at 10 keV, the peak number of defects is of nearly 400 and that for Ge cascades is of about 500 defects. Although at the peak of the cascades in Si and Ge a lower number of defects is created than in GaN with Ga PKAs, the Si and Ge cascades end with a far greater number of defects (about 200 for Si and 250 for Ge, compared to 50 for GaN at 10 keV). The recrystallization is a lot more efficient and faster in GaN than in Si and Ge. This is what explains the very low number of defects found in GaN. The same trend can be observed for the other studied energies, and is even made more blatant in Figure A.6 which displays the evolution of the number of defects at 25 keV.

Figure 3.11 shows the distribution of the number of clusters as a function of their size (number of defects) at the peak of 10 keV collision cascades and at the end of same collision cascade simulations in GaN (PKAs Ga and N), Si and Ge. In Si and Ge, clusters are defined as aggregates of vacancies and interstitials, and in GaN, as aggregates of vacancies, interstitials and antisites.

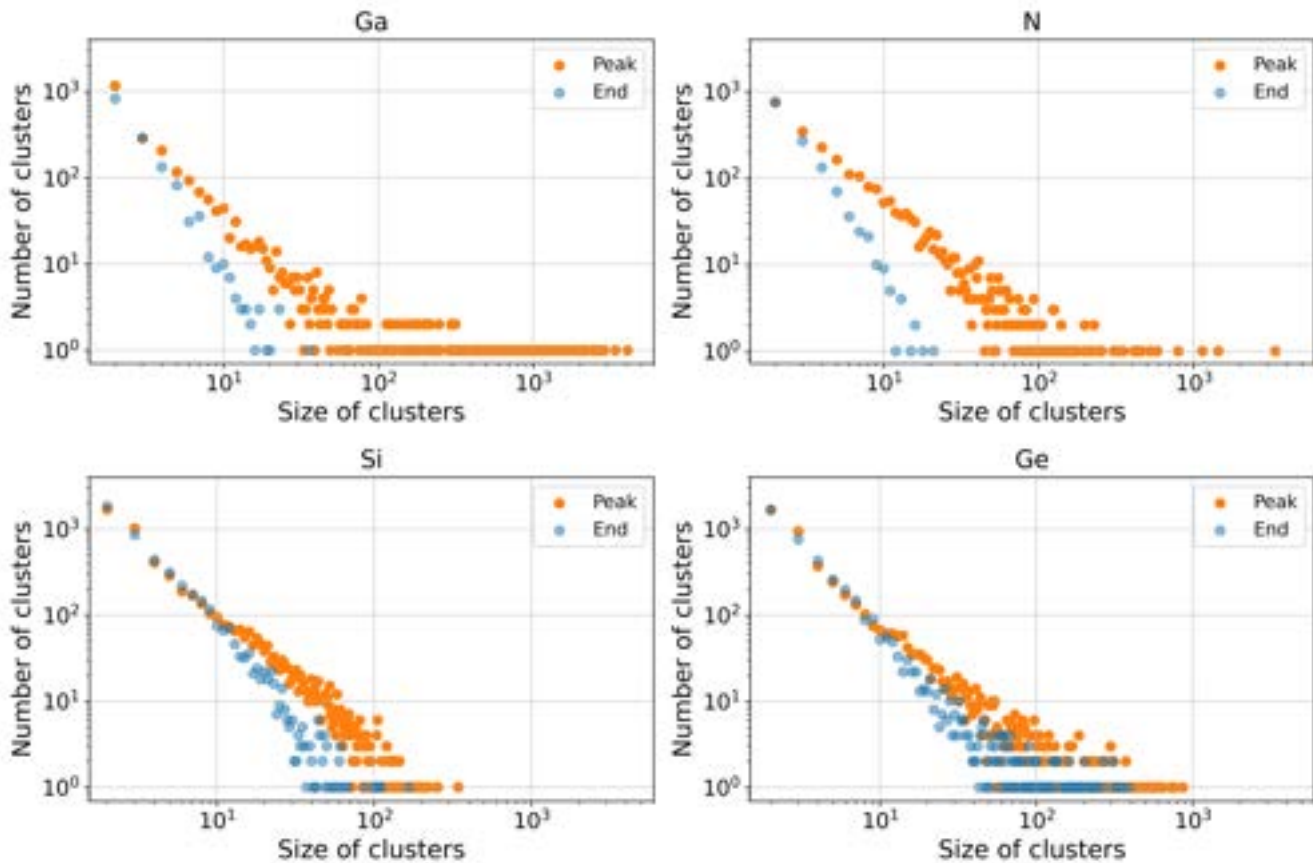


Figure 3.11: Distribution of the number of clusters as a function of their size at the peak of the 10 keV collision cascade (orange dots) and at the end of the same collision cascade simulation (blue dots). Ga PKAs in GaN (top left), N PKAs in GaN (top right), Si PKAs in Si (bottom left) and Ge PKAs in Ge (bottom right). Data are obtained from 100 simulations in each case.

At the peak of the cascades, very large clusters are present in Ge, and even more in GaN in which regardless of the PKA type, clusters of more than 10^3 defects are observed. In Si, the clusters are smaller, not exceeding 500 defects. For all materials, at the peak of the cascade and at the end, the point defects are the dominant type of defects. Also, the smaller the size of the cluster, the more frequently it is observed. The largest cluster sizes mentioned above are rarely observed.

The most interesting features of Figure 3.11 are the evolutions between the distribution of clusters between the peak and the end. For all materials, a recrystallization is observed, as already shown Figure 3.10. From the cluster point of view, it is characterized by a reduction of the number of clusters, and a reduction of the size of the clusters, with the end distributions of Figure 3.11 shifting to the left compared to the peak ones.

The average number of clusters at the peak of a cascade in GaN initiated by a Ga PKA is 26, which reduces to an average of 15 at the end of the same cascade simulation. Similarly, for N PKAs in GaN, the average cluster number is 26 at the peak, decreasing to an average of 13 clusters at the end of the same cascade simulations. In Ge, the average number of clusters at the peak of a cascade reaches 50, dropping to an average of 43 at the end of the same cascades. For Si, the peak cluster count is 55, which averages at 47 clusters at the end of the simulation of the same cascades. Those numbers tell us that a lot more clusters are formed in Si and Ge compared to GaN.

Moreover, it can be easily noticed in figure 3.11 that the recrystallization and cluster number decrease is far more important in GaN than in Si and Ge. Indeed, the peak and end distributions of clusters are still overlapping for Si and Ge, while they are almost completely distinct in the case of GaN, regardless of the PKA, meaning that the clusters have considerably healed. At the peak of the cascade, the bigger clusters are observed in GaN, whereas at the end, the bigger are found in Ge (above 100 in size) and Si (nearly 100 in size). At the end of the simulations, in GaN, clusters do not exceed 20 in size. This highlights the nature of the strong recrystallization in GaN: big clusters disappear and turn into small ones.

Figure 3.12 exhibits a visual representation of defects clusters at the peak and at the end of a 10 keV collision cascade simulation, initiated by a Ga PKA in GaN, a N PKA in GaN, a Si PKA in Si and a Ge PKA in Ge. The selected cascades in figure 3.12 are representative of average cascades for each PKA. They have been chosen because their average penetration depth and average number of defects closely align with the data provided in Table 3.2. Notably, all four cascades share the same direction.

Figure 3.12 provides a complementary visual representation of the cascades at 10 keV in the different materials. It is made clear that in GaN, the defects present at the peak have almost all disappeared at the end, whereas a lot more remain in Si and Ge. Also, it can be seen that for the Ga PKA case, the remaining clusters are of small size, whereas big clusters are still present in Si and Ge.

The cascades shown in Figure 3.12 correspond to average cascades; therefore, they do not encompass the full diversity of all possible cascade natures. This is for example why in the case of N PKAs in GaN, no big clusters can be seen though some are present in the pool of the 100 simulations carried out according to Figure 3.11. However, it gives a fairly good visual representation of the cascade nature in each material and of the evolution of the created clusters of defects: at the peak, cascades are dense and localized in Ge and in GaN with Ga PKA, with many defects; dispersed in Si with clusters of all sizes; dispersed

with mainly small clusters in GaN with N PKAs, whereas at the end, only small clusters remain in GaN; dispersed medium clusters in Si and dense big clusters in Ge.

3.4.3.3 Morphology of Cascades and Interstitials Atom Displacements

In the Results section, we have observed that the quantity and the characteristics of the defects formed can significantly vary depending on the material and the PKA types. As evidenced in figure 3.11 and Table 3.2, in GaN, only a small number of defects remain at the end of cascade simulations, regardless of the PKA type. Also, the type of PKA has nearly no influence on the total number of defects created at the end. However, the spatial distribution of the defects varies depending on the PKA type, lighter and smaller PKAs tend to result in more dispersed cascades. In the cases of Si and Ge, defects are sometimes contained in very large amorphous clusters, and the number of defects surpasses that in GaN.

On a macroscopic scale, the much higher melting temperature in GaN ($T_{\text{GaN}} \approx 2800$ K) than in silicon ($T_{\text{Si}} \approx 1700$ K) and germanium ($T_{\text{Ge}} \approx 1200$ K) [43], may explain those discrepancies. Indeed the low melting temperatures of Si and Ge allows the formation of amorphous zones of defects, well known in semiconductors after irradiation [44], whereas in GaN, it protects the material from the development of such amorphous pockets. This aspect is enhanced by the high thermal conductivity of GaN (1.3 W/cm·K[45]). However, following figure 3.10, the peak number of defects for a Ga PKA in GaN is even higher than in the case of Ge, meaning that the difference between the two materials comes from the recrystallization stage.

This aspect can also be linked to the thermal properties. Lots of atoms are displaced by a Ga PKA in GaN, in a dense area (Table 3.2), but the temperature attained may not be high enough or does not hold for a sufficient time to melt the material and create amorphous pockets.

Going deeper in the atomic scale analysis, Figure 3.13 displays the distribution of the distance the interstitials identified at the peak of the cascade are displaced from their initial equilibrium position (called displacement), at the peak of the cascade and at the end of the simulation. Therefore, the displacements plotted at the end are not all coming from interstitial atoms as many of the atoms identified as interstitials at the peak of the cascade are back to their initial position at the end of the simulation. The comparison of the peak curves of Figure 3.13 reveals interesting features. In GaN, only one very strong peak arises at about 1.2 Å. In Si (Ge), two peaks can be clearly identified, at about 2.3 Å (2.4 Å) and 4.9 Å (5.4 Å); At the peak of the cascade, interstitials have traveled further in Si and Ge than in GaN. Looking at the end (blue) curves of Figure 3.13 tells us about the evolution of the atoms identified as interstitials.

In Si and Ge, several peaks are clearly visible. The first peak near 0 Å corresponds to the part of the interstitials that healed and went back to their equilibrium position. A second peak can be identified, at the first nearest neighbour distance (2.35 Å for Si, 2.45

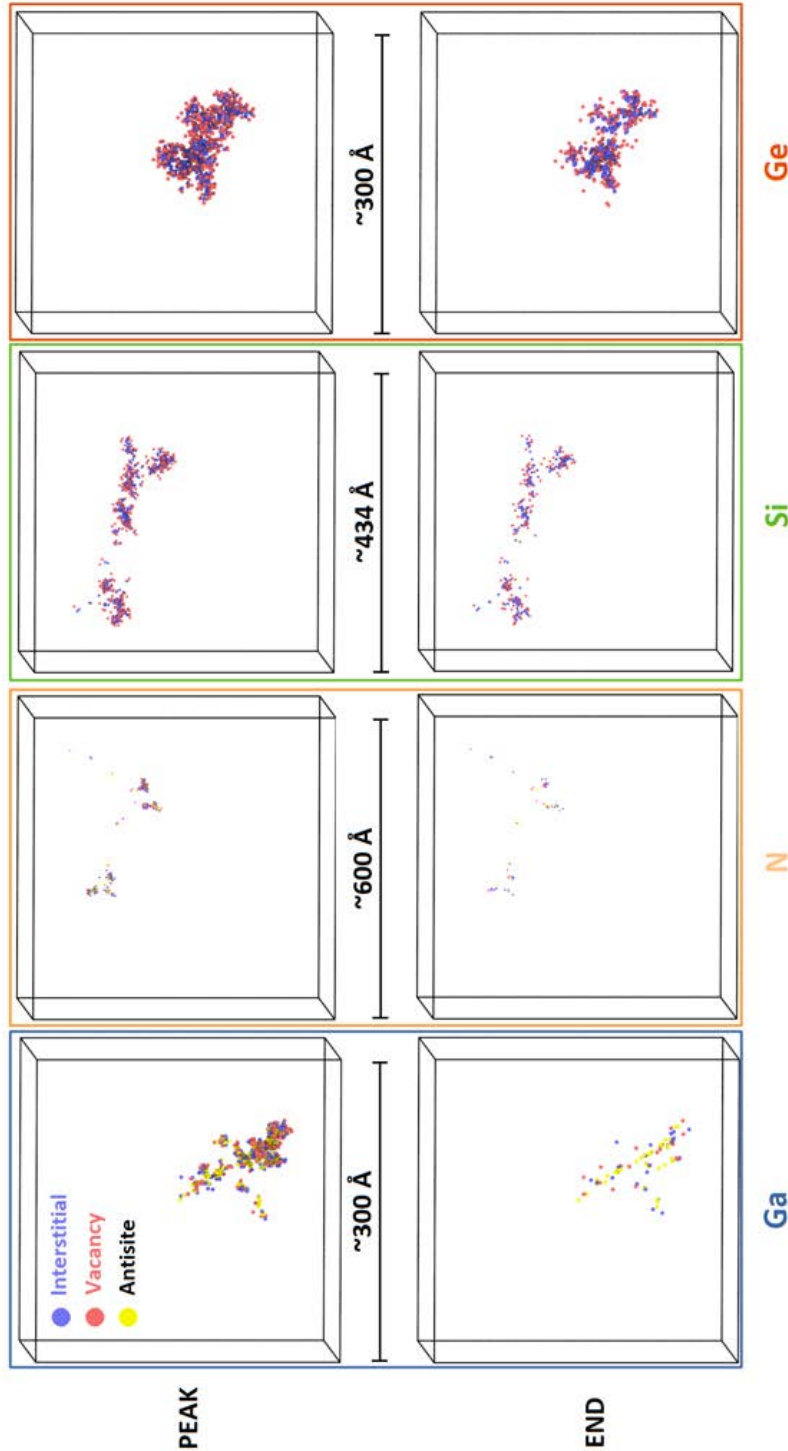


Figure 3.12: Visual representation of defect clusters at the peak of a 10 keV collision cascade (top images) and at the end of the same 10 keV collision cascade simulation (bottom images) in GaN (PKAs Ga and N), Si and Ge. The blue spheres represent interstitial atoms, the red spheres represent vacancies and the yellow spheres represent antisites without specifying the type (Ga in an N site or N in a Ga site).

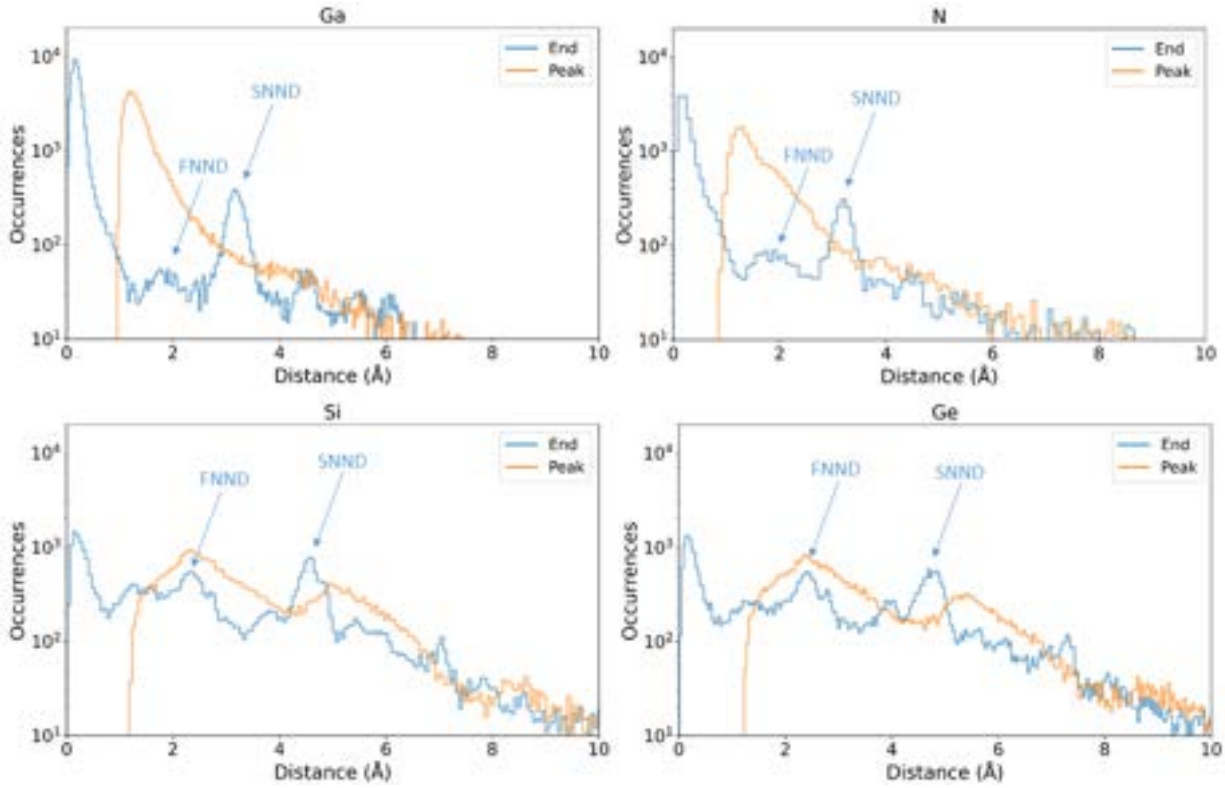


Figure 3.13: Distributions of the distance the interstitials identified at the peak of the 10 keV cascades in GaN, Si and Ge are displaced from their initial equilibrium position (called displacement), at the peak of the cascades and at the end of the simulations. The first blue arrow represents the first nearest neighbour distance (FNND), the second represents the second nearest neighbour distance (SNND). Data are obtained from the average of 100 simulations in each case. At the peak of the cascades, the atoms selected to plot the displacements are all interstitials, whereas at the end, atoms identified as interstitials at the peak may have healed back to their initial position, and are thus not all interstitials.

Å for Ge). A peak at the second-neighbor distance is almost noticeable. Those peaks correspond to interstitial atoms that found their place in the crystal in ejecting other atoms from their equilibrium position.

In GaN, two very large peaks are clearly visible. The first one by 0 Å, just like for Si and Ge. The second one corresponds to the second nearest neighbour distance of the GaN material, which indicates that a proportion of the displaced atoms have shifted to the distance of the second nearest atom.

The largest peak is close to 0 Å, indicating that a large proportion of the displaced atoms have returned to their original crystal sites, *i.e.*, healing the material. This peak is much more prominent in GaN than in Si and Ge, which justifies the greater recrystallization.

Finding precise atomic displacement distances corresponding to the distance between the first neighboring atom and the second neighboring atom links the displacement dy-

namics to the crystallography of the material. The manner in which Ga and N atoms are ordered in GaN, and the way they move in the crystal, explains the high degree of recrystallization present in this material, in contrast to Si and Ge. The atoms making up the clusters formed in GaN are thus displaced close to their original crystalline site, promoting healing, *i.e.*, their return to their crystalline site, thus reducing the number of defects and the number/size of clusters (Refer to Figure 3.11)).

The overestimation by TRIM of the number of defects created in GaN compared to in Si and Ge (see part 3.2) can also be explained by the recrystallization characteristics of GaN. TRIM uses the BCA, which simplifies the picture of collision cascades by considering only two-body interactions (collisions). Atoms are represented as hard spheres that cannot interact directly with other atoms outside of collisions. On the contrary, MD, as it takes into account manybody interactions between all the atoms in the system can be used to simulate complex behaviors such as melting, amorphization and defect and clusters reordering.

Therefore, it is no surprise to observe discrepancies between MD and TRIM results when studying collision cascades in GaN, where complex recrystallization phenomena taking their origin in the thermal properties as well as in the crystal structure of GaN occur.

3.4.3.4 Concluding Remarks

Our results provide a snapshot in time of the dynamic displacement damage effects that occur during collision cascades. Beyond this moment, at the end of the cascades, the ensemble of defects continues to evolve as a result of atomic diffusion and drift over an extended period of time. Those longer time effects are not included in this analysis.

To better understand the effects of radiation-induced displacement damage in GaN, we ran 100 simulations for each collision cascade, at three different energies, 1 keV, 10 keV and 25 keV, in GaN, Si and also in Ge, for comparison. The behavior of the different PKAs and the three materials proved to be very different. N PKAs penetrate deeper into GaN than Ga PKAs and create a lot fewer defects at the peak of the cascade, *i.e.*, at the moment of the cascade when the maximum number of defects is reached.

However, at the end of the simulations, a very similar number of defects is obtained with Ga and N PKAs in GaN. In Si and especially in Ge, a lot of defects are formed at the peak, but less than in GaN with Ga PKAs. Nonetheless, at the end, more defects remain in Si and Ge than in GaN, regardless of the PKA type. The clustering of the defects is also very different between the materials and the PKAs employed. In Ge, and in GaN with Ga PKAs, the concentration of defects is very dense at the peak.

Nevertheless, at the end, only a few defects remain in small clusters in GaN, while Ge exhibits lot of defects mostly contained in large amorphous pockets. In Si, defects are contained in clusters of various sizes, including amorphous pockets, and dispersed along the trajectory of the PKA, which is longer than in Ge and in GaN with Ga PKAs. In GaN

with N PKAs, the resulting clusters obtained at the end are very few in number, very small in size and widely dispersed along the N PKA trajectories.

These intriguing observations come from the remarkable self-healing properties of the GaN material. The number of defects in GaN decreases dramatically and rapidly after the peak. Also, the distribution of the cluster size changes a lot between the peak and the end of the cascades, compared to Si and Ge. Although large clusters may form initially in GaN, they heal quickly, leaving only small clusters at the end of the process.

Our study thus confirms, at the considered energies, the enhanced intrinsic resistance of GaN to displacement damage, compared to other semiconducting materials. We attribute the strong dynamic self-healing of GaN to its thermal properties, less favorable than Si and Ge for the formation of amorphous pockets, and also to very compact atomic structure of wurtzite GaN. Indeed, due to the short interatomic distance in GaN, interstitials rarely travel far from their equilibrium site, and are thus able to easily return to their initial site, thus healing the structure. As part of our research initiative, we have planned irradiation experiments on bulk materials (Si and later GaN) and their characterization using a transmission electron microscope. The aim will be to compare the results of our simulations with the defects observed under the microscope in the samples tested, providing a robust validation of our findings.

3.5 Conclusion

This chapter provides a comprehensive analysis of collision cascades in GaN, complemented by a comparative study with Si and Ge. The investigation begins with a preliminary parametric study using the Monte Carlo (MC) method to optimize and design molecular dynamics (MD) simulations. These simulations offer a deeper understanding of the dynamics and ballistic processes of collision cascades. Key simulation parameters, such as the size of the simulation box and the choice of primary knock-on atom (PKA), are carefully tailored to the material and PKA type, ensuring accurate and meaningful results.

A comparative study of neutron displacement damage cross-sections reveals that GaN experiences lower energy loss from non-ionizing interactions within the energy range of approximately 1 keV to 10 keV, outperforming Si. Furthermore, MD simulations underscore GaN's remarkable resilience to displacement damage (DD) over the investigated timescales and energy ranges. Notably, a post-cascade recrystallization phase is observed, driven by the limited atomic displacement characteristic of GaN's dense wurtzite structure. Unlike Si and Ge's diamond structures, the higher density of GaN minimizes atomic displacement, enabling displaced atoms to remain close to their equilibrium positions and facilitating rapid structural recovery. Although simulations at higher energies become increasingly complex to manage, extending this analysis to greater energy levels will be crucial to validate whether GaN's superior performance persists under more extreme conditions.

Building on these findings, the next phase of this study will focus on investigating the threshold displacement energy—a fundamental parameter representing the minimum energy required to permanently displace an atom from its equilibrium position. This exploration aims to deepen our understanding of GaN's intrinsic resistance to radiation-induced damage and further establish its potential as a robust material for applications in radiation-intensive environments.

Bibliography

- [1] I Vurgaftman and J R n Meyer. Band parameters for nitrogen-containing semiconductors. *Journal of applied physics*, 94(6):3675–3696, 2003.
- [2] David Maier, Mohammed Alomari, Nicolas Grandjean, Jean-Francois Carlin, Marie-Antoinette Diforte-Poisson, Christian Dua, Andrey Chuvilin, David Troadec, Christophe Gaquière, Ute Kaiser, et al. Testing the temperature limits of gan-based hemt devices. *IEEE Transactions on device and materials reliability*, 10(4):427–436, 2010.
- [3] Fanny Berthet, Sebastien Petitdidier, Yannick Guhel, Jean Lionel Trolet, Philippe Mary, Christophe Gaquiere, and Bertrand Boudart. Influence of neutron irradiation on electron traps existing in gan-based transistors. *IEEE Transactions on Nuclear Science*, 63(3):1918–1926, 2016.
- [4] Ling Lv, Xiaoyao Yan, Yanrong Cao, Qing Zhu, Ling Yang, Xiaowei Zhou, Xiaohua Ma, and Yue Hao. Significant degradation of algan/ gan high-electron mobility transistors with fast and thermal neutron irradiation. *IEEE Transactions on Nuclear Science*, 66(6): 886–891, 2019.
- [5] Md Abu Jafar Rasel, Ryan Schoell, Nahid Sultan Al-Mamun, Khalid Hattar, C Thomas Harris, Aman Haque, Douglas E Wolfe, Fan Ren, and Stephen J Pearton. Heavy ion irradiation induced failure of gallium nitride high electron mobility transistors: effects of in-situ biasing. *Journal of Physics D: Applied Physics*, 56(30):305104, 2023.
- [6] Stephen J Pearton, Richard Deist, Fan Ren, Lu Liu, Alexander Y Polyakov, and Jihyun Kim. Review of radiation damage in gan-based materials and devices. *Journal of Vacuum Science & Technology A*, 31(5), 2013.
- [7] J Nord, K Nordlund, J Keinonen, and K Albe. Molecular dynamics study of defect formation in gan cascades. *Nuclear Instruments and Methods in Physics Research Section B: Beam Interactions with Materials and Atoms*, 202:93–99, 2003.
- [8] J Nord, K Albe, P Erhart, and KJoPCM Nordlund. Modelling of compound semiconductors: analytical bond-order potential for gallium, nitrogen and gallium nitride. *Journal of Physics: Condensed Matter*, 15(32):5649, 2003.
- [9] Nanjun Chen, Erich Rasch, Danhong Huang, Eric R Heller, and Fei Gao. Atomic-scale simulation for pseudometallic defect-generation kinetics and effective niel in gan. *IEEE Transactions on Nuclear Science*, 65(5):1108–1118, 2018.
- [10] Kai Nordlund, Steven J Zinkle, Andrea E Sand, Fredric Granberg, Robert S Averback, Roger E Stoller, Tomoaki Suzudo, Lorenzo Malerba, Florian Banhart, William J Weber, et al. Primary radiation damage: A review of current understanding and models. *Journal of Nuclear Materials*, 512:450–479, 2018.
- [11] Miguel C Sequeira, Jean-Gabriel Mattei, Henrique Vazquez, Flyura Djurabekova, Kai Nordlund, Isabelle Monnet, Pablo Mota-Santiago, Patrick Kluth, Clara Grygiel, Shuo

- Zhang, et al. Unravelling the secrets of the resistance of gan to strongly ionising radiation. *Communications physics*, 4(1):51, 2021.
- [12] MO Ruault and W Jäger. Transmission electron microscope investigations of defects produced by individual displacement cascades in si and ge. *Journal of Microscopy*, 118(1):67–73, 1980.
- [13] LM Howe and MH Rainville. Features of collision cascades in silicon as determined by transmission electron microscopy. *Nuclear Instruments and Methods*, 182:143–151, 1981.
- [14] Damien Lambert, Julien Parize, Nicolas Richard, Melanie Raine, Olivier Duhamel, Claude Marcandella, Arthur Losquin, Anne Hemeryck, Christophe Inguibert, and Philippe Paillet. Neutron displacement damage cross section in gan: Numerical evaluations and differences with si. *IEEE Transactions on Nuclear Science*, 70(8):1870–1877, 2023.
- [15] Coping with the stochasticity of collision cascades in molecular dynamics simulations. *Nuclear Instruments and Methods in Physics Research Section B: Beam Interactions with Materials and Atoms*, 500-501:1–9, 2021. ISSN 0168-583X. doi: <https://doi.org/10.1016/j.nimb.2021.02.015>. URL <https://www.sciencedirect.com/science/article/pii/S0168583X21001683>.
- [16] Melanie Raine, Antoine Jay, Nicolas Richard, Vincent Goiffon, Sylvain Girard, Marc Gaillardin, and Philippe Paillet. Simulation of single particle displacement damage in silicon—part i: global approach and primary interaction simulation. *IEEE Transactions on Nuclear Science*, 64(1):133–140, 2016.
- [17] Antoine Jay, Melanie Raine, Nicolas Richard, Normand Mousseau, Vincent Goiffon, Anne Hemeryck, and Pierre Magnan. Simulation of single particle displacement damage in silicon—part ii: Generation and long-time relaxation of damage structure. *IEEE Transactions on Nuclear Science*, 64(1):141–148, 2016.
- [18] Antoine Jay, Anne Hemeryck, Nicolas Richard, Layla Martin-Samos, Melanie Raine, Alexandre Le Roch, Normand Mousseau, Vincent Goiffon, Philippe Paillet, Marc Gaillardin, et al. Simulation of single-particle displacement damage in silicon—part iii: First principle characterization of defect properties. *IEEE Transactions on Nuclear Science*, 65(2):724–731, 2018.
- [19] G Herrero-Saboya, L Martin-Samos, Antoine Jay, Anne Hemeryck, and N Richard. A comprehensive theoretical picture of e centers in silicon: From optical properties to vacancy-mediated dopant diffusion. *Journal of Applied Physics*, 127(8), 2020.
- [20] Thomas Jarrin, Antoine Jay, Melanie Raine, Normand Mousseau, Anne Hemeryck, and Nicolas Richard. Simulation of single particle displacement damage in si ge alloys—interaction of primary particles with the material and generation of the damage structure. *IEEE Transactions on Nuclear Science*, 67(7):1273–1283, 2020.

- [21] Thomas Jarrin, Antoine Jay, Anne Hemeryck, and Nicolas Richard. Parametric study of the two-temperature model for molecular dynamics simulations of collisions cascades in si and ge. *Nuclear Instruments and Methods in Physics Research Section B: Beam Interactions with Materials and Atoms*, 485:1–9, 2020.
- [22] Damien Lambert, Olivier Riant, Didier Thouvenot, Eric Feuilleux, and Thierry Coladant. Evaluation of the displacement damage equivalent fluence from different facilities and devices. In *2018 18th European Conference on Radiation and Its Effects on Components and Systems (RADECS)*, pages 1–4. IEEE, 2018.
- [23] U. Lowell. Neutron facilities. [online] Available: <https://www.um1.edu/Research/RadLab/Neutron-Facilities.aspx/>, December 2022. Accessed on [2022, Dec].
- [24] Calculator of 1-mev equivalent neutron fluences. [online] Available: <https://www.triumf.ca/pif-nif/calculator-1-mev-equiv>, December 2022. Accessed on [2022, Dec].
- [25] C Inguibert and R Gigante. Nemo: a code to compute niel of protons, neutrons, electrons and heavy ions. In *2005 8th European Conference on Radiation and Its Effects on Components and Systems*, pages PG2–1. IEEE, 2005.
- [26] M.J. Boschini, P.G. Rancoita, and M. Tacconi. Sr-niel-7 calculator: Screened relativistic (sr) treatment for niel dose, nuclear and electronic stopping power calculator (version 10.16). <https://www.sr-niel.org/>, 2014. Accessed on [2022, Dec].
- [27] GH Kinchin and RS Pease. The displacement of atoms in solids by radiation. *Reports on progress in physics*, 18(1):1, 1955.
- [28] Kai Nordlund, Andrea E Sand, Fredric Granberg, Steven J Zinkle, Roger Stoller, Robert S Averback, Tomoaki Suzudo, Lorenzo Malerba, Florian Banhart, William J Weber, et al. Primary radiation damage in materials. review of current understanding and proposed new standard displacement damage model to incorporate in cascade defect production efficiency and mixing effects. 2015.
- [29] Christophe Inguibert. Including a distribution of threshold displacement damage energy on the calculation of the damage function and electron’s non ionizing energy loss. *Journal of Nuclear Materials*, 559:153398, 2022.
- [30] S Agarwal, Y Lin, C Li, RE Stoller, and SJ Zinkle. On the use of srim for calculating vacancy production: Quick calculation and full-cascade options. *Nuclear Instruments and Methods in Physics Research Section B: Beam Interactions with Materials and Atoms*, 503:11–29, 2021.
- [31] K. Nordlund et al. Defect production in collision cascades in elemental semi-conductors and FCC metals. *Phys. Rev. B*, 57(13):7556–7570, Apr 1998. doi: 10.1103/PhysRevB.57.7556.
- [32] Antoine Béré and Anna Serra. Atomic structure of dislocation cores in GaN. *Phys. Rev. B*, 65, May 2002. doi: 10.1103/PhysRevB.65.205323. Art. no. 205323.

- [33] J. F. Ziegler, M. D. Ziegler, and J. P. Biersack. SRIM - The stopping and range of ions in matter (2010). *Nucl. Instr. Meth. Phys. R. B*, 268:1818–1823, Jun 2010. doi: 10.1016/j.nimb.2010.02.091.
- [34] J. Tersoff. New empirical approach for the structure and energy of covalent systems. *Phys. Rev. B*, 37:6991–7000, Apr 1988. doi: 10.1103/PhysRevB.37.6991.
- [35] R. Devanathan et al. Displacement threshold energies in β -SiC. *J. Nucl. Mat.*, 253(1):47–52, Mar 1998. ISSN 0022-3115. doi: [https://doi.org/10.1016/S0022-3115\(97\)00304-8](https://doi.org/10.1016/S0022-3115(97)00304-8).
- [36] J. Tersoff. Modeling solid-state chemistry: Interatomic potentials for multicomponent systems. *Phys. Rev. B*, 39:5566–5568, Feb 1989. doi: 10.1103/PhysRevB.39.5566.
- [37] DM Duffy and AM Rutherford. Including the effects of electronic stopping and electron-ion interactions in radiation damage simulations. *Journal of Physics: Condensed Matter*, 19(1):016207, 2006.
- [38] Sandia Corporation. fix electron/stopping command, 2023. URL https://docs.lammps.org/fix_electron_stopping.html Accessed on: July 2023.
- [39] Alexander Stukowski. Visualization and analysis of atomistic simulation data with OVITO-the Open Visualization Tool. *MODELLING AND SIMULATION IN MATERIALS SCIENCE AND ENGINEERING*, 18(1), JAN 2010. ISSN 0965-0393. doi: {10.1088/0965-0393/18/1/015012}.
- [40] H Hensel and H M Urbassek. Implantation and damage under low-energy Si self-bombardment. *Phys. Rev. B*, 57, Feb 1998. doi: 10.1103/PhysRevB.57.4756. Art. no. 4756.
- [41] P. F. Zou and R. F. W. Bader. A topological definition of a Wigner-Seitz cell and the atomic scattering factor. *Acta Crist. A*, 50(6):714–725, Nov 1994. doi: 10.1107/S0108767394003740.
- [42] P. Lopez *et al.* *J. App. Phys.*, 111:033519, 2012. doi: 10.1063/1.3682108.
- [43] W.M. Haynes. *CRC Handbook of Chemistry and Physics*. CRC Press, Boca Raton, USA. ISBN 9781315380476. doi: <https://doi.org/10.1201/9781315380476>.
- [44] J R Srour and J W Palko. Displacement damage effects in irradiated semiconductor devices. *IEEE Trans. Nucl. Sci.*, 60:1740–1766, Jun 2013. doi: 10.1109/TNS.2013.2261316.
- [45] A. Jezowski et al. Thermal conductivity of GaN crystals in 4.2–300 K range. *Sol. St. Comm.*, 128(2):69–73, Jan 2003. ISSN 0038-1098. doi: [https://doi.org/10.1016/S0038-1098\(03\)00629-X](https://doi.org/10.1016/S0038-1098(03)00629-X).

Chapter 4:

Quantifying Threshold Displacement Energy in GaN

Contents

4.1	Introduction	118
4.2	State of the Art	120
4.3	Simulation Parameters and Configuration	122
4.3.1	AIMD Computational details	122
4.3.2	MD Computational details	123
4.4	Exploration of TDE in GaN	124
4.4.1	Threshold Displacement Energy Values for 5 Directions in AIMD and MD at 0 K and 300 K	125
4.4.2	Defect Configuration	129
4.5	Large-Scale study of TDE in GaN	131
4.5.1	Raw TDE Data Section	131
4.5.2	Spatial Distribution of Directions Based on TDE	135
4.5.3	Temperature Effect on TDE in GaN	139
4.6	Discussion	141
4.7	Conclusion	143

4.1 Introduction

This chapter presents a comprehensive investigation of the TDE in GaN using advanced numerical simulations that combine AIMD and classical MD approaches. The TDE is a fundamental property in materials science, that represents the minimum energy threshold required to displace an atom from its original lattice position, thereby initiating defect formation. Its significance extends beyond fundamental physics, as it is also a key input parameter for Monte Carlo tools that model particle-material interactions and predict defect generation mechanisms. A TDE value specific to the material must be entered by the user before the particle-material simulations, and this value influences the number of defects obtained at the end of these simulations.

This chapter is divided into four main sections. The first section provides a state of the art review of numerical TDE simulation methods and its application to GaN. The second section details the parametrization of numerical simulations. The third section presents the results obtained through AIMD and classical MD simulations along five crystallographic directions and at two temperatures (0 K and 300 K), highlighting the significant influence of temperature on the TDE. Finally, the fourth section expands this study to include quantitative results obtained with classical MD for a broader set of directions and at various temperatures, offering an unprecedented exploration of atomic displacement mechanisms.

Results reveal large variations in TDE values between nitrogen and gallium primary knock-on atoms (PKAs), demonstrating complex defect generation mechanisms that are intrinsically dependent on the atomic species involved. The results show that TDE values can reach extremely high energy levels for N PKAs compared to Ga PKAs. The range of TDE values is also significantly wider for N PKAs than for Ga PKAs. At 0 K, very high TDE values are observed for both types of PKAs. The defect configurations range from simple atomic vacancies to intricate multi-site displacements and depend on the type of PKA. Ga PKAs, being much heavier than N PKAs, can generate different type of defects. Typically, Ga PKAs result in the creation of an N vacancy and an N-N dumbbell. However, in some cases, an N vacancy, an N-N dumbbell, a Ga interstitial, and a Ga vacancy are observed simultaneously. The MD statistical study reveals several trends. Little difference is observed in TDE values between 0 K and 300 K for both PKA types, although extreme TDE values are more commonly seen at 0 K for N PKAs. The directional study highlights the anisotropy of TDE. When PKAs are directed towards nearby neighboring atoms, the TDE is high, whereas it is lower when PKAs are directed towards "voids", *i.e.* channeling. In GaN wurtzite structure that the space surrounding Ga atoms is less dense compared to that around N atoms. Finally, the temperature study highlights the unique behavior of GaN compared to other semiconductors, such as GaAs. With increasing temperature, for Ga and N PKAs, we observe a spreading of the TDE distribution, which is in line with the expected behaviour, however, we observe an unusual trend, which is the appearance of two peaks at non-zero temperatures.

The investigation not only quantifies the threshold displacement energy but also high-

lights the intricate interplay between atomic structure, thermal effects, and energy transfer in semiconductor materials. It represents a significant step forward in understanding the fundamental mechanisms of radiation-induced damage and atomic rearrangement in advanced semiconductor systems.

4.2 State of the Art

Many studies focus on evaluating the TDE, particularly on the influence of factors such as temperature or material doping. A critical aspect to consider is the anisotropy of the TDE, which arises from the energy required to displace an atom, being highly dependent on its local atomic environment.

Despite the fact that our study is primarily based on numerical simulations, it is essential to compare the simulation results with experimental data whenever possible. Experimental measurements of TDE are available for gallium in the orthorhombic base-centered structure of monatomic Ga. In [1], TDE was experimentally determined by monitoring changes in electrical resistivity of materials during electron irradiation at a temperature of 4.2 K. The minimum TDE value found was 12 eV, consistent with the results in [2]. However, the average TDE value was not reported in either study. Additionally, these works highlight the anisotropy of TDE, such as in copper, where a 50 eV difference exists between "open" directions (*i.e.* free of direct neighboring atom collisions) and constrained crystallographic directions (*i.e.* aligned with neighboring atoms). In directions with the lowest TDE, the phenomenon of "focusing" occurs: the PKA moves into the position of the displaced atom, which in turn displaces the next atom, and so on. This chain reaction continues until the energy dissipates sufficiently, creating a Frenkel pair.

Although the study in [3] focuses exclusively on metals, the observed TDE anisotropy associated with different crystal lattice configurations can be put parallel to semiconductors. The work presents TDE "surfaces", representing average displacement energy mapped onto a chart based on the studied material's crystallographic directions (see Figure 4.1). It also discusses the importance of accounting for the Frenkel pair resistivity during the irradiation of monatomic crystals. This resistivity reflects the spontaneous recombination volume of Frenkel pairs.

The emergence of computational techniques, particularly molecular dynamics (MD) and ab initio molecular dynamics (AIMD), has revolutionized TDE investigations. Nordlund *et al.* [4] demonstrated the pivotal role of interatomic potentials in accurately modeling displacement mechanisms and TDE in iron using classical molecular dynamics simulations. Their work compares results obtained with 11 different interatomic potentials. In the Methods section, they address the impact of thermal vibrations on the choice of the PKA and the consistency of simulating a large number of TDEs. To ensure the uniqueness of each simulation and incorporate the stochastic effects of thermal vibrations, two approaches are presented: generating unique thermal displacements for each simulation or randomly selecting the PKA within the lattice.

Molecular dynamics simulations have also been employed to study the influence of temperature on the TDE in TiO₂. In their work, [5] performed an extensive series of simulations to account for thermal vibrations across a range of temperatures. Rather than identifying a single fixed TDE value, they introduced the concept of a "TDE probability," which reflects

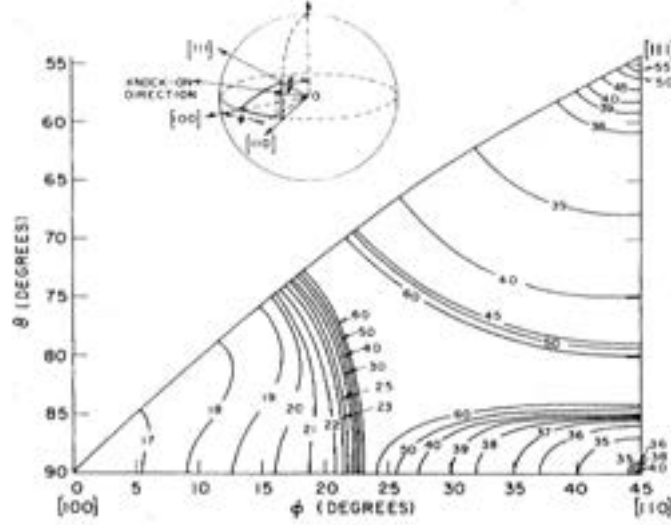


Figure 4.1: Threshold energy surface in α -iron in the fundamental triangle [3].

the likelihood of defect creation under specific conditions. This approach acknowledges the complexity of defect formation, which is influenced by numerous factors. Interestingly, their results reveal an increase in the TDE with rising simulation temperatures. The study also emphasizes the importance of comprehensive sampling to capture these variations reliably. It acknowledges the probabilistic nature of defect formation rather than treating it as a deterministic process.

Building on this work, Robinson et al.[6] proposed a systematic methodology for calculating TDE in molecular dynamics simulations, using TiO_2 as a case study. Their approach details the step-by-step process required to accurately estimate the TDE values, highlighting key considerations such as the need for extensive sampling of crystallographic directions and the inclusion of temperature effects. This methodological framework provides a robust foundation for future studies, ensuring that simulations capture the inherent variability of displacement phenomena across different conditions.

Previous studies primarily employed classical molecular dynamics (MD) to investigate TDE. However, an alternative approach, *ab initio* molecular dynamics (AIMD), offers a more detailed description of atomic interactions by explicitly accounting for electronic interactions. This method was utilized by P. Olsson, C. S. Becquart, and C. Domain [7] to study the TDE in iron. Due to the computational intensity of AIMD simulations, the analysis was limited to high-symmetry crystallographic directions. Nevertheless, the results obtained were found to be in good agreement with available experimental data.

Several studies have investigated semiconductors using molecular dynamics. For instance, Miller [8] examined different directions in Si and associated them with TDE values, a methodology also applied to -SiC [9]. Lucas *et al.* [10] employed AIMD to determine TDE values for four directions in SiC, while also characterizing the resulting defects. Similarly, Chen *et al.* [11] mapped TDE values in GaAs for Ga and As PKAs. Their

study, based on classical MD, evaluated both TDE values and the types of defects produced.

For the TDE in GaN, only two studies are available to date. The first, conducted by Xiao et al. [12], employed AIMD to calculate TDE values. As with the study on iron, the computational cost of AIMD restricted the investigation to a few crystallographic directions. TDE values for Ga and N primary knock-on atoms were presented at a temperature of 100 K. The results indicate a general trend of higher TDE for Ga PKAs compared to N PKAs. Additionally, the study detailed the defect configurations generated by PKAs. N PKAs predominantly formed N vacancies and N-N dumbbells, while Ga PKAs produced a wider variety of defects, including Ga and N vacancies, N-N dumbbells, Ga interstitials, and octahedral Ga configurations. The second study, conducted by S. Hauck et al. [13], included a broader sampling of crystallographic directions by employing classical molecular dynamics. Their investigation focused on the TDE for GaN at 0 K, specifically for Ga primary knock-on atoms. This MD study is complemented by density functional theory (DFT) calculations for the electronic characterization of the identified defects. These investigations laid critical groundwork for understanding GaN's displacement mechanisms.

Our study detailed in this chapter advances this body of knowledge by providing a more comprehensive exploration of TDE in GaN, investigating both Ga PKA and N PKA in addition of a broader range of crystallographic directions taking advantage of the symmetry of the GaN lattice.

The next sections will detail the simulation methodologies, presenting the thorough parametrization process that is needed for the computational investigations using MD and AIMD into GaN's threshold displacement energy characteristics.

4.3 Simulation Parameters and Configuration

Despite sharing the common goal of determining TDE, the AIMD and classical MD simulation methods employ significantly different underlying mechanisms and parametrization strategies. Two separate sections detail the parameters and methodology for each simulation method.

4.3.1 AIMD Computational details

AIMD simulations were performed using the *Quantum Espresso* [14] software. The pseudopotentials used in the calculations were based on the Perdew-Burke-Ernzerhof (PBE) exchange-correlation functional, specifically the ultrasoft potential, $[Ar]3d^{10}4s^24p^1$ for gallium and $[He]2s^22p^3$ for nitrogen [15]. Before starting the main simulations, preliminary tests were conducted to stabilize a GaN lattice containing 300 atoms (150 Ga atoms and 150 N atoms) at a temperature of 300 K over a duration of 10 seconds, ensuring the equilibrium and reliability of the initial system.

The studied system was defined using a tetragonal lattice, with a primary lattice parameter of $a = 30.42$ Bohr and a ratio of $c/a = 0.98$. Following several preliminary tests, the wavefunctions were calculated using a plane-wave energy cutoff of 80 Ry. Electronic occupations were described using a Gaussian smearing method with a smearing parameter of 0.001 Ry. To account for dynamic effects without imposing geometric constraints, crystalline symmetries were disabled, and a total of 1 400 electronic bands were included to ensure convergence. The k -point grid used was limited to the Gamma point. The electronic minimization process was conducted using the Davidson diagonalization algorithm. A mixing parameter of 0.7 was applied, combined with an energy convergence threshold of 1.0×10^{-8} Ry.

The *ab initio* molecular dynamics parameters included a time step of 20 a.u. (1 a.u. corresponding to 4.8378×10^{-17} seconds), with a total of 1500 simulation steps, corresponding to a total simulated time of 1.5 picoseconds.

AIMD simulations are time-consuming, and this limitation significantly influenced our methodology for investigating the TDE. We restricted our study to the five directions previously explored by Xia et al., examining them at two temperatures: 0 K and 300 K.

The method for determining the TDE in a given direction is as follows:

- The primary knock-on atom (PKA) is placed at the center of the simulation box.
- Three initial energies are tested: 20 eV, 50 eV, and 80 eV, representing the energy imparted to the PKA.
- The simulation is run for over 1 ps.
- After the simulation, the lattice is analyzed:
 - If a defect persists, the energy is decreased.
 - If no defect is observed, the energy is increased.

This iterative process continues to refine, with the increment or decrement reduced to 1 eV, at which point the TDE is determined for each studied direction.

4.3.2 MD Computational details

As explained in Section 3.4.1 in Chapter 3, we used the LAMMPS tool [16] for the collision cascade simulation. We employ Tersoff potentials coupled to repulsive ZBL potentials [17–19]. Nonadiabatic electronic effects were included to have a complete picture of the process involved in the event using an available command within LAMMPS [20]. It incorporates the electronic stopping power via friction force insertion into Newton's equation of motion.

Our TDE simulations take place in boxes created from non-primitive orthorhombic unit cells composed of 8 sites (4 Ga and 4 N) for which the lattice parameters are $a = 3.18$ Å,

$b = 5.52 \text{ \AA}$ and $c = 5.17 \text{ \AA}$. The positions of atoms are presented in Table 3.1 in the Chapter 3.

The energies studied for TDE are much lower than those for collision cascades, which allows for significantly smaller simulation boxes. The box side lengths are 100 \AA , corresponding to 90,440 atoms. The system is equilibrated for 15 ps at the desired temperature with a timestep of 1 fs before the initiation of the TDE. It is important to note that simulations at strictly 0 K are not feasible; instead, they are conducted at 0.01 K.

For each PKA type and each energy, 100 simulations are run, each one with a different direction in order to obtain statistically relevant results [21]. Also, to address the issue of thermal vibrations discussed in Section 4.2, 100 simulations were performed for each direction, each using a different equilibration seed to ensure the uniqueness of each simulation. The seed number guarantees a distinct equilibration, *i.e.* unique atomic positions for every simulation. The PKA is positioned at the center of the simulation box. TDE simulations are started by attributing to an atom, chosen as the PKA, a certain velocity vector corresponding to the desired PKA energy.

The timestep is chosen based on the distance covered by the PKA between two timesteps, which does not exceed 0.025 \AA in our simulations. Additional detail about the chosen integration ensembles and thermostat can be found in Section 2.4.2.3 of Chapter 2.

Data processing is performed using OVITO visualization software and its analysis tools [22]. Notably, the number of defects is defined as the number of Frenkel pairs (number of interstitial-vacancy pairs created). We chose to calculate the number of defects with the Wigner-Seitz criterion [23], as implemented in OVITO.

The method for determining the threshold displacement energy (TDE) is as follows:

- The primary knock-on atom (PKA) is placed at the center of the simulation box.
- Three initial energies are tested, depending on the type of PKA:
 - For Ga PKAs: 40 eV, 50 eV, and 90 eV.
 - For N PKAs: 90 eV, 150 eV, and 200 eV.
- The simulation is run, and the resulting configuration is analyzed using OVITO:
 - If a defect is observed, the energy is decreased.
 - If no defect is detected, the energy is increased.

This iterative process continues, with the increment or decrement reduced to 1 eV, at which point the TDE is determined for each studied direction.

4.4 Exploration of TDE in GaN

We present the results of TDE investigations in GaN, performed using AIMD and MD simulations. Our study examines TDE values along five crystallographic directions for Ga

PKAs and N PKAs, see Figure 4.2, at 0 K and 300 K, providing insight into temperature dependence, defect generation and types of created defects, and the directional anisotropy of atomic displacements in GaN.

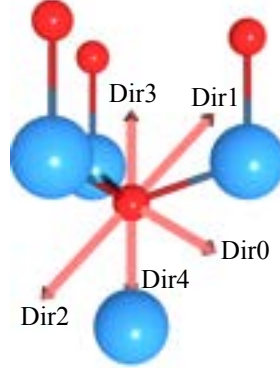


Figure 4.2: Schematic representation of the 5 selected directions. The directions are defined as Dir0 ($x:-1, y:0, z:1$), Dir1 ($x:-1, y:2, z:-1$), Dir2 ($x:1, y:0, z:-1$), Dir3 ($x:0, y:0, z:1$), and Dir4 ($x:0, y:0, z:-1$). For N PKAs, the nearest neighbors along these directions are Ga atoms, while for Ga PKAs, the nearest neighbors are N atoms. Dir4 corresponds to the direction pointing toward the closest neighbor for N PKAs, whereas Dir3 corresponds to the direction pointing toward the closest neighbor for Ga PKAs.

In the following analysis, we define the TDE as the minimum energy required to generate a defect that remains stable after a simulation time specific to each method. Due to numerical constraints, for AIMD simulations, a defect is considered "persistent" if it remains after 1 ps, while for MD simulations, the threshold is 5 ps. The resulting defects may include interstitials, vacancies, or antisites, depending on the energy imparted and the crystallographic direction. Due to the computational intensity and time required for AIMD simulations, only a single simulation is performed to determine the TDE for each direction. In contrast, for MD simulations, the TDE is averaged over 100 simulations, each equilibrated using a different random seed.

4.4.1 Threshold Displacement Energy Values for 5 Directions in AIMD and MD at 0 K and 300 K

Table 4.1 presents the data obtained from TDE simulations at 300 K using AIMD for Ga PKAs in GaN and N PKAs in GaN. These tables also show the distance between the equilibrium position of the PKAs and their final position, *i.e.* after 1 ps, as well as the defects created and the type of the first atom impacted by the PKA.

At 300 K, for Ga PKAs, there is a significant disparity in TDE values, ranging from 28 to 145 eV, across the five directions. In contrast, for N PKAs, the TDEs range from 50 eV to 68 eV for the five directions. For Ga PKAs, the TDEs are lowest in directions Dir3 and Dir4, while in direction Dir2, the TDE reaches 145 eV. Such a high energy value within a

4.4. Exploration of TDE in GaN

300-atoms cell might suggest potential issues related to energy redistribution and thermal dissipation. The distances between the equilibrium site and the final position of the PKAs range from 2.4550 Å to 4.970 Å for Ga PKAs and from 3.190 Å to 5.459 Å for N PKAs. N PKAs tend to travel farther than Ga PKAs, likely because N PKAs are lighter than Ga PKAs. Finally, for all five directions, the first atom impacted by the PKAs is always of the opposite type.

Data at 300 K

Ga PKA	TDE AIMD (eV)	Defects	PKA Distance (Å)	Neighbour atom type
Dir0 (-1 0 1)	100	V_N - N-N	3.599	N
Dir1 (-1 2 -1)	77	V_{Ga} - I_{Ga}	4.970	N
Dir2 (1 0 -1)	145	V_{Ga} - I_{Ga} - V_N - N-N	4.544	N
Dir3 (0 0 1)	28	V_N - N-N	4.091	N
Dir4 (0 0 -1)	34	V_N - N-N	2.450	N

N PKA	TDE AIMD (eV)	Defects	PKA Distance (Å)	Neighbour atom type
Dir0 (-1 0 1)	50	V_N - N-N	3.190	Ga
Dir1 (-1 2 -1)	53	V_N - N-N	3.850	Ga
Dir2 (1 0 -1)	57	V_N - N-N	5.459	Ga
Dir3 (0 0 1)	56	V_N - N-N	4.989	Ga
Dir4 (0 0 -1)	68	V_N - N-N	4.616	Ga

Table 4.1: Tables summarizing the TDEs, the distances between the equilibrium site and the final positions of the PKAs, defects created and the type of the first neighboring atom impacted by the PKAs, for Ga PKAs in GaN (top table) and N PKAs in GaN (bottom table) at 300 K as obtained from AIMD simulations for the 5 directions. With V_N a nitrogen vacancy, N-N nitrogen dumbbell, V_{Ga} a gallium vacancy and I_{Ga} an interstitial gallium.

We identify four types of defects: V_N , a nitrogen vacancy; N-N, a nitrogen dumbbell (i.e. two nitrogen atoms occupying the same equilibrium site); V_{Ga} , a gallium vacancy; and I_{Ga} , a gallium interstitial. It is observed that Ga PKAs can produce all these defects. In contrast, in our study, N PKAs exclusively generated nitrogen vacancies and nitrogen dumbbells. The following section provides a more detailed analysis of these defects (see Section 4.3).

The Table 4.2 presents data obtained from TDE simulations at 0 K using AIMD for Ga PKAs in GaN and N PKAs in GaN. It also includes the distances between the equilibrium positions of the PKAs and their final positions, *i.e.* after 1 ps, as well as the defects created and the type of the first atom impacted by the PKA.

Data at 0 K

Ga PKA	TDE AIMD (eV)	Defects	PKA Distance (Å)	Neighbour atom type
Dir0 (-1 0 1)	>120	N/A	N/A	N
Dir1 (-1 2 -1)	81	V_N - N-N	4.569	N
Dir2 (1 0 -1)	103	V_N - N-N	4.703	N
Dir3 (0 0 1)	Limit size effect	N/A	N/A	N
Dir4 (0 0 -1)	Limit size effect	N/A	N/A	N

N PKA	TDE AIMD (eV)	Defects	PKA Distance (Å)	Neighbour atom type
Dir0 (-1 0 1)	>120	N/A	N/A	Ga
Dir1 (-1 2 -1)	>120	N/A	N/A	Ga
Dir2 (1 0 -1)	>120	N/A	N/A	Ga
Dir3 (0 0 1)	>120	N/A	N/A	Ga
Dir4 (0 0 -1)	>120	N/A	N/A	Ga

Table 4.2: Tables summarizing the TDEs, the distances between the equilibrium site and the final positions of the PKAs, defects created and the type of the first neighboring atom impacted by the PKAs, for Ga PKAs in GaN (top table) and N PKAs in GaN (bottom table) at 0 K as obtained from AIMD simulations for the 5 directions. With V_N a nitrogen vacancy and N-N nitrogen dumbbell.

At 0 K, no TDE was identified for Ga PKAs in directions Dir0, Dir3, and Dir4. In direction Dir0, the energy exceeds 120 eV, we choose not to exceed this energy because of the problem explained below. For directions Dir3 and Dir4, a ‘focusing’ effect, as described in [1], is observed. In this phenomenon, the PKA displaces a neighboring atom, which in turn displaces another neighboring atom in the same direction, and so on. This effect causes issues in our periodic simulation boxes at 0 K. At this temperature, the atoms are arranged in a perfect crystal lattice, and when the PKA collides with a neighboring atom aligned along the same direction, this chain reaction can lead to an atom exiting the simulation box. Due to the periodic boundary conditions, the atom re-enters from the opposite boundary, which is a non-physical event that causes the simulation to crash.

However, for directions Dir1 and Dir2, TDEs were successfully identified, at 81 eV and 103 eV, respectively. The distances between the equilibrium sites and the final positions of the PKAs are 4.569 Å and 4.703 Å for these directions, respectively. For N PKAs, no specific TDEs were identified. In all five directions, the TDEs exceed 120 eV. At 0 K, we observe only nitrogen vacancies and nitrogen dumbbells for both Ga PKAs and N PKAs. For a more detailed analysis of the defects, refer to Section 4.3.

Table 4.3 presents the data obtained from TDE simulations at 0 K and 300 K using AIMD and MD for Ga PKAs and N PKAs in GaN. For Ga PKAs at 0 K, the TDE values obtained with MD are lower than those from AIMD for directions Dir0 to Dir2. However,

4.4. Exploration of TDE in GaN

for directions Dir3 and Dir4, the TDE values in MD are significantly higher, reaching 291 eV. In AIMD, no TDEs were identified for these two directions due to the ‘focusing’ problem, which led to simulation crashes.

At 300 K, for Ga PKAs, the TDE values in MD vary widely, ranging from 9 eV for direction Dir1 to 75 eV for direction Dir3. Standard deviations are also reported and are larger for directions Dir3 and Dir4 compared to directions Dir0, Dir1, and Dir2. The trends observed between AIMD and MD differ: in AIMD, the highest TDEs are found for directions Dir0, Dir1, and Dir2, while in MD, the opposite is true.

TDE (eV) for AIMD & MD at 0 K & 300 K

Ga PKA	TDE AIMD 0 K	TDE MD 0 K	TDE AIMD 300 K	TDE MD 300 K
Dir0 (-1 0 1)	>120	22 (<1)	100	23 (3)
Dir1 (-1 2 -1)	81	15 (<1)	77	9 (1)
Dir2 (1 0 -1)	103	34 (<1)	145	22 (3)
Dir3 (0 0 1)	Limit size effect	291 (<1)	28	75 (11)
Dir4 (0 0 -1)	Limit size effect	291 (<1)	34	70 (13)

N PKA	TDE AIMD 0 K	TDE MD 0 K	TDE AIMD 300 K	TDE MD 300 K
Dir0 (-1 0 1)	>120	36 (<1)	50	51 (16)
Dir1 (-1 2 -1)	>120	22 (<1)	53	19 (5)
Dir2 (1 0 -1)	>120	73 (<1)	57	63 (8)
Dir3 (0 0 1)	>120	188 (<1)	56	126 (23)
Dir4 (0 0 -1)	>120	129 (<1)	68	134 (33)

Table 4.3: Comparative tables of TDEs for AIMD and MD simulations, for Ga PKAs in GaN (top table) and N PKAs in GaN (bottom table) for the 5 directions. For MD, the mean values of TDE are the average of 100 simulation. Standard deviations are shown in parentheses.

For N PKAs at 0 K, comparison is challenging as the TDE values in AIMD exceed 120 eV in all directions. In MD, directions Dir3 and Dir4 show much higher TDE values, at 188 eV and 129 eV, respectively, compared to the other directions. At 300 K, for N PKAs, the TDEs obtained in MD span a wide energy range, from 19 eV for direction Dir1 to 134 eV for direction Dir4. The highest TDEs are observed in directions Dir3 and Dir4. The standard deviations for N PKAs are much larger than those for Ga PKAs, ranging from 5 eV to 33 eV. The TDE values obtained in MD for N PKAs are higher than those found in AIMD.

Several general trends are observed:

1. **Higher TDE values at 0 K:** Regardless of the PKA type or simulation method, TDEs are higher at 0 K.

2. **High TDE directions:** Directions Dir3 and Dir4 consistently exhibit the highest TDEs, regardless of PKA type or simulation method.
3. **Challenges in AIMD at 0 K:** In AIMD, it is difficult to find TDEs below 120 eV at 0 K, and the 'focusing' problem occurs for Ga PKAs.
4. **PKA type influence:** TDEs are higher for N PKAs than for Ga PKAs, irrespective of temperature or simulation method.

4.4.2 Defect Configuration

Defects were observed after 1 ps for each TDE value in the directions where TDEs were identified. Four types of defects were detected, as illustrated in Figure 4.3: vacancies and interstitials, which form Frenkel pairs, as well as N dumbbells, where two nitrogen atoms form a dumbbell structure at the equilibrium site of an N atom.

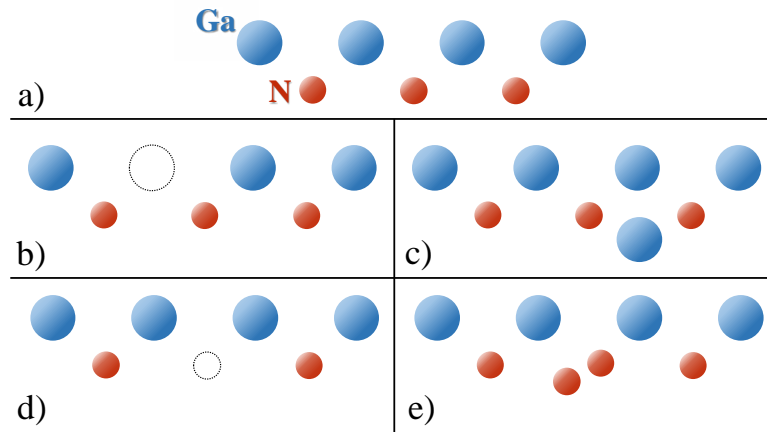


Figure 4.3: Schematic representation of defects observed after AIMD simulations: a) No defect b) Ga vacancy, c) Ga interstitial, d) N vacancy, e) N-N dumbbell.

For Ga PKAs, all four defect types can be created: a Ga vacancy and a Ga interstitial, as well as an N vacancy and an N dumbbell. In contrast, for N PKAs, only N vacancies and N dumbbells are formed. This limitation is due to the smaller size and lighter mass of N atoms, making it difficult for them to displace Ga atoms.

Two primary mechanisms are observed for Ga PKAs:

1. **Collision with a neighboring N atom:** The Ga PKA returns to its equilibrium site, but the impacted N atom is ejected from its position, creating an N dumbbell and an N vacancy.
2. **Deflection by a neighboring atom:** The Ga PKA is sufficiently deflected, moving far enough from its equilibrium site that it does not return, resulting in the formation of a Ga vacancy and a Ga interstitial.

The difficulty for an N atom to displace a Ga atom lies in their difference in size and weight. Specifically, a Ga atom is nearly twice as large ($r_{Ga} = 1.3 \text{ \AA}$ vs. $r_N = 0.85 \text{ \AA}$) and almost five times heavier ($m_{Ga} = 69.7 \text{ u}$ vs. $m_N = 14.0 \text{ u}$) than an N atom. The neighboring atoms of an N atom are Ga atoms, which act as a cage. By effectively shielding the nitrogen atom, they block the trajectory of the N PKA, leaving the only viable path for the nitrogen atom to pass through a gap between two Ga atoms. At very high TDE energies, *i.e.* above 150 eV, it is theoretically possible for an N PKA to displace a neighboring Ga atom. However, the creation of a Ga vacancy and interstitial has not been observed. For both PKAs, the most common defect pair is the combination of an N vacancy and an N dumbbell. Notably, no N interstitials were observed.

4.5 Large-Scale study of TDE in GaN

In this section, we present the results of studying the TDE in GaN using classical Molecular Dynamics simulations for Ga and N Primary Knock-on Atoms at various temperatures. The study considers 105 directions chosen based on the symmetry of the wurtzite GaN crystal, with additional details available in Chapter 2, Section 2.4.6. For each direction, 100 simulations are performed, each with unique atomic positions. These 100 distinct atomic positions are created by employing a random seed during the equilibration process. This extensive number of simulations enables a rigorous statistical analysis. The first subsection focuses on the raw TDE data, while the second explores the directional dependence of the results. Finally, the last subsection presents TDE results at different temperatures along a single direction, supported by a large number of simulations.

4.5.1 Raw TDE Data Section

Figure 4.4 displays a histogram of TDE data at 0 K across 105 directions for Ga PKAs (blue) and N PKAs (orange) in GaN with 100 seeds for each direction. The dataset includes 10,000 TDE values for each PKA type. Several observations can be made. First, TDE values for Ga PKAs are generally lower than those for N PKAs. Specifically, most TDEs for Ga PKAs fall between 15 eV and 85 eV, while TDEs for N PKAs range from 15 eV to 215 eV, with some reaching up to 290 eV. As the standard deviations for each direction are negligible or zero, they are not displayed.

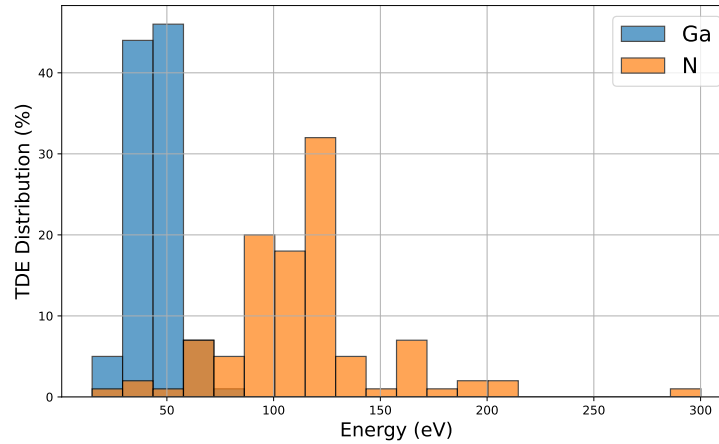


Figure 4.4: Histogram of TDEs at 0 K across 105 directions for Ga PKAs (blue) and N PKAs (orange) in GaN. The data represent 10,000 TDEs obtained for each PKA.

Figure 4.5 shows the TDE data at 300 K across 105 directions for Ga PKAs (blue) and N PKAs (orange) in GaN with 100 seeds for each direction. Like the data at 0 K, a similar trend is observed: TDEs for Ga PKAs are lower than those for N PKAs. Ga PKA TDEs range from approximately 15 eV to 75 eV, while those for N PKAs span from about 80 eV to 160 eV, with a few values falling below 80 eV.

Figure 4.6 presents the standard deviations of TDE data at 300 K for Ga PKAs (blue) and N PKAs (orange) in GaN. The data are the standard deviations for each direction. It reveals

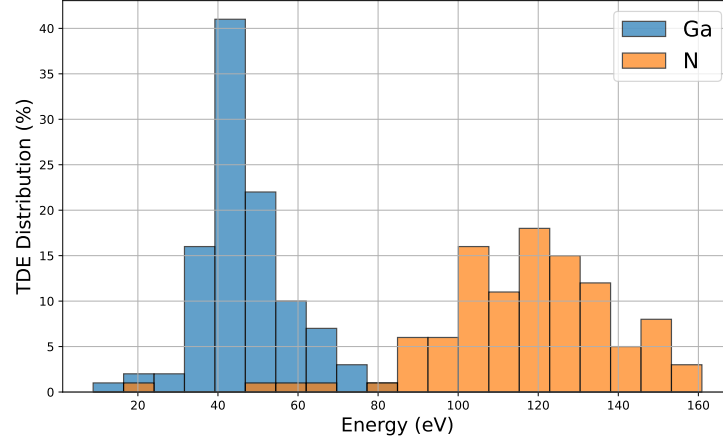


Figure 4.5: Histogram of TDEs at 300 K across 105 directions for Ga PKAs (blue) and N PKAs (orange) in GaN. The data represent 10,000 TDEs obtained for each PKA.

a notable difference between the two types of PKAs. For Ga PKAs, standard deviations range from about 2 eV to 20 eV, whereas for N PKAs, they range from approximately 4 eV to 45 eV. These larger standard deviations indicate significant variability in TDE values for N PKAs within the same direction.

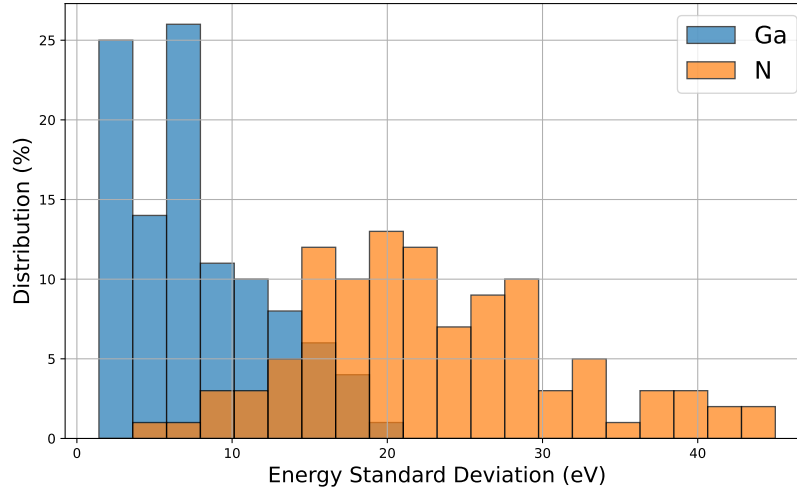


Figure 4.6: Histogram of standard deviations of TDE data at 300 K for Ga PKAs (blue) and N PKAs (orange) in GaN. Data are the standard deviations for each direction.

Figure 4.7 depicts TDE data for Ga PKAs at 0 K (blue) and 300 K (orange) in GaN. At 0 K, TDEs range between approximately 15 eV and 75 eV, with most values concentrated between 30 eV and 60 eV. At 300 K, TDEs span from about 8 eV to 78 eV, which is more or less the same dispersion as at 0 K.

Figure 4.8 shows TDE data for N PKAs at 0 K (blue) and 300 K (orange) in GaN. Each dataset includes 10,000 TDE values per PKA type. At 0 K, most TDE values for N PKAs fall between 40 eV and 160 eV, while at 300 K, the range narrows slightly to 50 eV to 155 eV. High TDE values are observed at 0 K, with some reaching between 200 eV and 300 eV.

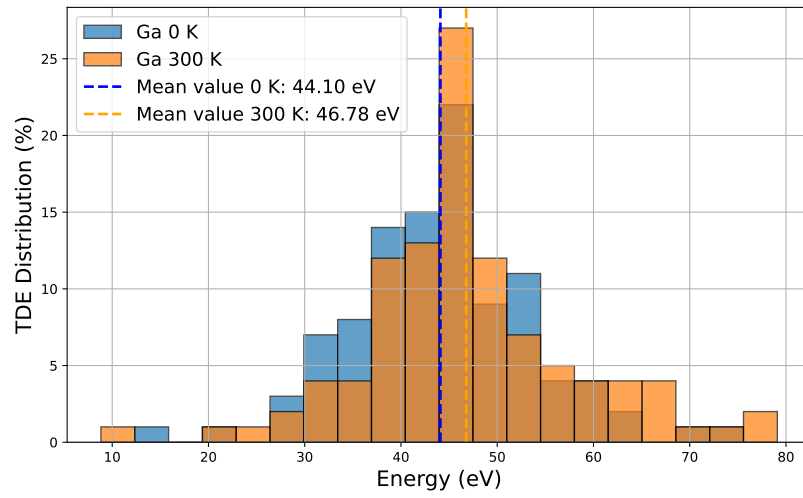


Figure 4.7: Histogram of TDE data for Ga PKAs at 0 K (blue) and Ga PKAs at 300 K (orange) in GaN. With the average total value at both temperatures represented by dotted lines.

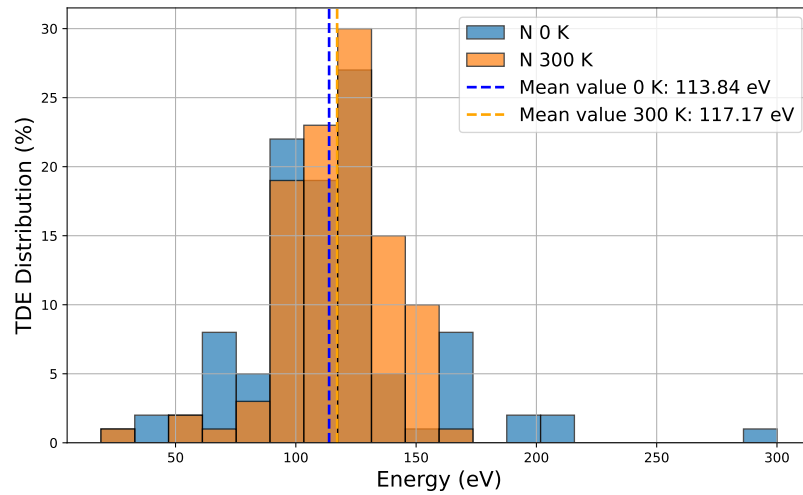


Figure 4.8: Histogram of TDE data for N PKAs at 0 K (blue) and N PKAs at 300 K (orange) in GaN. With the average total value at both temperatures represented by dotted lines.

in specific directions.

The total mean values of the TDEs are also shown in Figures 4.7 and 4.8. For both PKAs, the total mean value is larger at 300 K than at 0 K. It is of ~ 44 eV at 0 K and ~ 47 eV at 300 K for Ga PKAs; ~ 114 eV at 0 K and ~ 117 eV at 300 K for N PKAs. For Ga PKAs it increases by about 2.5 eV while for N PKAs it increases by about 3 eV. At 0 K, we obtain 44 eV for Ga PKAs and 113 eV for N PKAs, which coincides well with the results of [24], which find 45 ± 1 eV for Ga PKAs and 109 ± 1 eV for N PKAs.

In summary, TDE values for N PKAs are generally higher than those for Ga PKAs, regardless of temperature. For Ga PKAs, TDE values remain relatively consistent across temperatures. However, for N PKAs, TDE values are slightly higher at 300 K, although the maximum values are more prominent at 0 K. Finally, the average value increases by a few eV between 0 K and 300 K for both temperatures.

4.5.2 Spatial Distribution of Directions Based on TDE

Figure 4.9 shows a GaN unit cell with Ga atoms (red) and N atoms (blue), along with 100 directions represented as a point cloud surrounding a nitrogen atom. Each point corresponds to the extremity of a unit vector whose origin is the N atom. The 3D point cloud can be described as resembling an orange segment, covering one-sixth of an imaginary sphere centered on the N PKA. This sphere can be divided into six equivalent parts due to the wurtzite GaN symmetry. The purpose of this subsection is to illustrate the TDE distribution across the directions studied for collision cascades in Chapter 3.

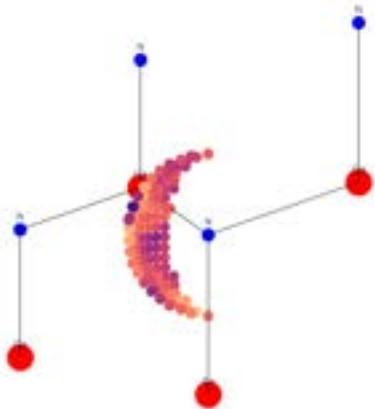


Figure 4.9: Schematic representation of a GaN unit cell with Ga atoms (red) and N atoms (blue), along with 100 directions represented as a point cloud surrounding a nitrogen atom. Each point corresponds to the extremity of a unit vector whose origin is the N atom.

Figure 4.10 presents the spatial distribution of directions for Ga PKAs based on their average TDE values (color gradient) at different temperatures. TDEs of 20 eV are shown in black, while values of 80 eV and above are displayed in yellow. Each point represents the average of 100 simulations. Additionally, the figure includes a map of the distances to the nearest neighbor in each direction, effectively a neighbor map for Ga PKAs. Below each figure, the same plot is shown with density zones.

Also observed for Figure 4.7 in Section 4.5.1, very little difference is observed between the two temperatures, except for a few directions at 0 K where high TDEs occur. On the right, the neighbor map shows that directions with the highest TDEs correspond to those pointing toward the nearest neighbors—specifically, in the lower left, very top, and very bottom regions. Conversely, directions toward sparsely dense areas on the neighbor map (white regions without nearby atoms) show very low TDE values when compared with the TDE point cloud.

Figure 4.11 displays the spatial distribution of directions for N PKAs based on their average TDE values (color gradient) at different temperatures. TDEs of 20 eV are represented

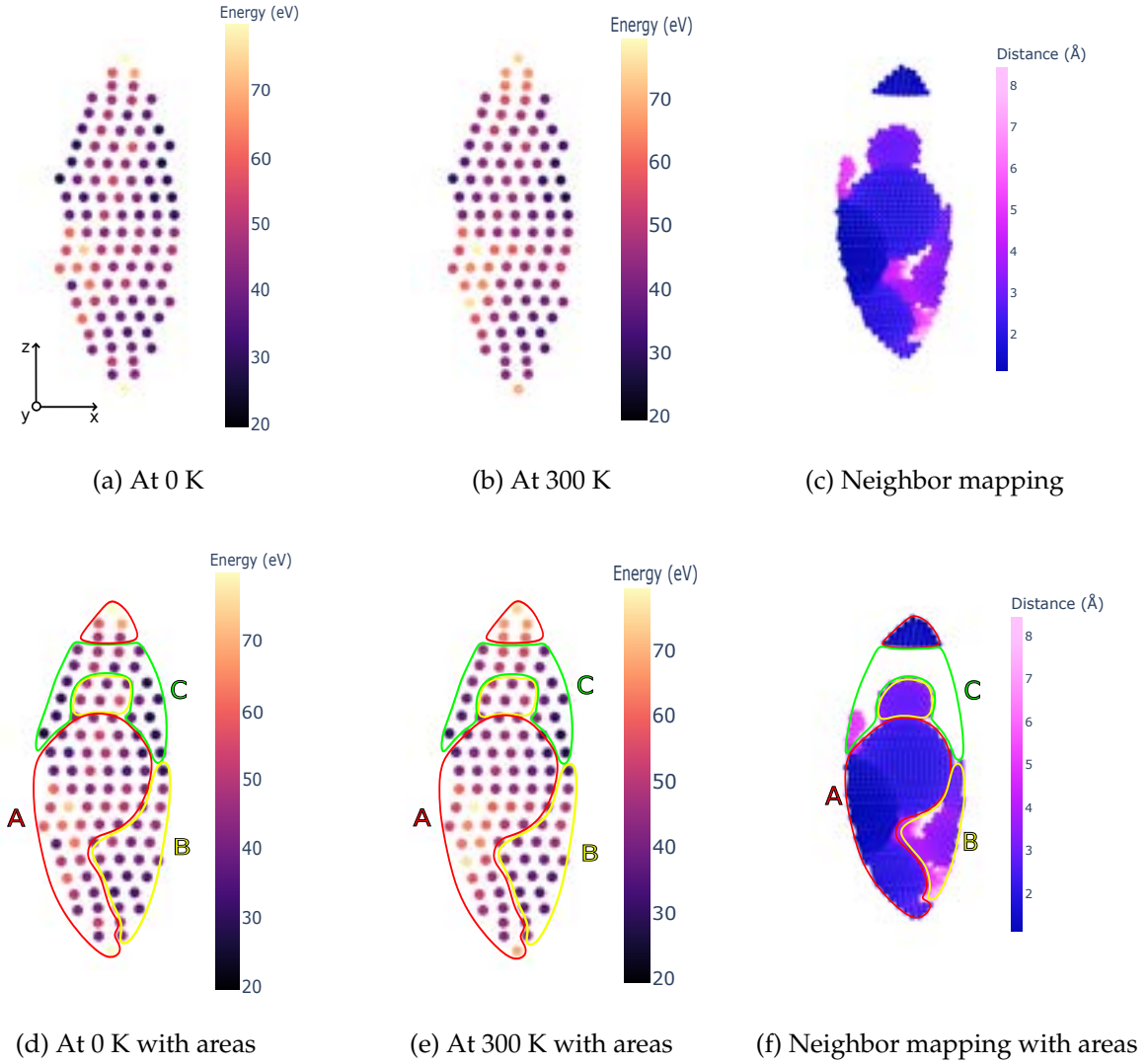


Figure 4.10: On the left and middle panels, spatial distribution of points representing directions based on their average TDE (color gradient) for Ga PKAs at different temperatures. A TDE of 20 eV is represented in black, while 80 eV and above are represented in yellow. Each point represents the average of 100 simulations. On the right, a spatial distribution of points shows the distance to the nearest neighbor in the associated direction, also referred to as a neighbor mapping for Ga PKAs based on their distances. The origin of the directions is the Ga PKA. Below each figure, the same plot is shown with density zones labeled A, B, and C to aid explanation. These zones are defined based on the neighboring atom map. Zone A (red): "Dense" regions where neighboring atoms are very close. Zone B (yellow): "Moderately dense" regions, where neighboring atoms are at a moderate distance (< 3.5 Å) and some void space is present. Zone C (green): "Sparsely dense" regions with significant void space, where neighboring atoms are at distances > 4 Å. The lighter the color, the greater the distance to neighboring atoms.

in black, while values of 180 eV and above are shown in yellow. Each point represents the average of 100 simulations. This figure also includes a neighbor map illustrating the distance to the nearest atom for each direction, originating from the N PKA. Below each figure, the same plot is shown with density zones.

A noticeable difference between 0 K and 300 K can be observed. At 0 K, high TDE values are observed, while at 300 K, the energy distribution appears more homogeneous. The tendency can also be seen in Figure 4.8. For both temperatures, in Zone A (dense), the lightest points (highest TDE values) dominate. In Zones B (moderately dense) and C (sparsely dense), darker points (lower TDE values) are more frequent.

For N PKAs, at both temperatures, the lightest points (highest TDE values) are concentrated in Zone A (dense). In contrast, darker points are more prevalent in Zones B (moderately dense) and C (sparsely dense). Notably, Zone A for N PKAs is larger than for Ga PKAs, as are the sparsely dense Zone C areas. This can be attributed to N PKAs having neighboring Ga atoms, which are twice as large as N atoms, resulting in a more obstructed environment around N PKAs. For both temperatures, in Zone A (dense), the lightest points (highest TDE values) dominate. In Zones B (moderately dense) and C (sparsely dense), darker points (lower TDE values) are more frequent.

This subsection highlights that at 0 K, TDE sometimes reach high values, particularly in directions pointing toward nearby neighbors. At both 0 K and 300 K, for both Ga and N PKAs, high TDEs are consistently observed in directions toward close neighbors, while lower TDEs are found in directions toward distant neighbors or voids.

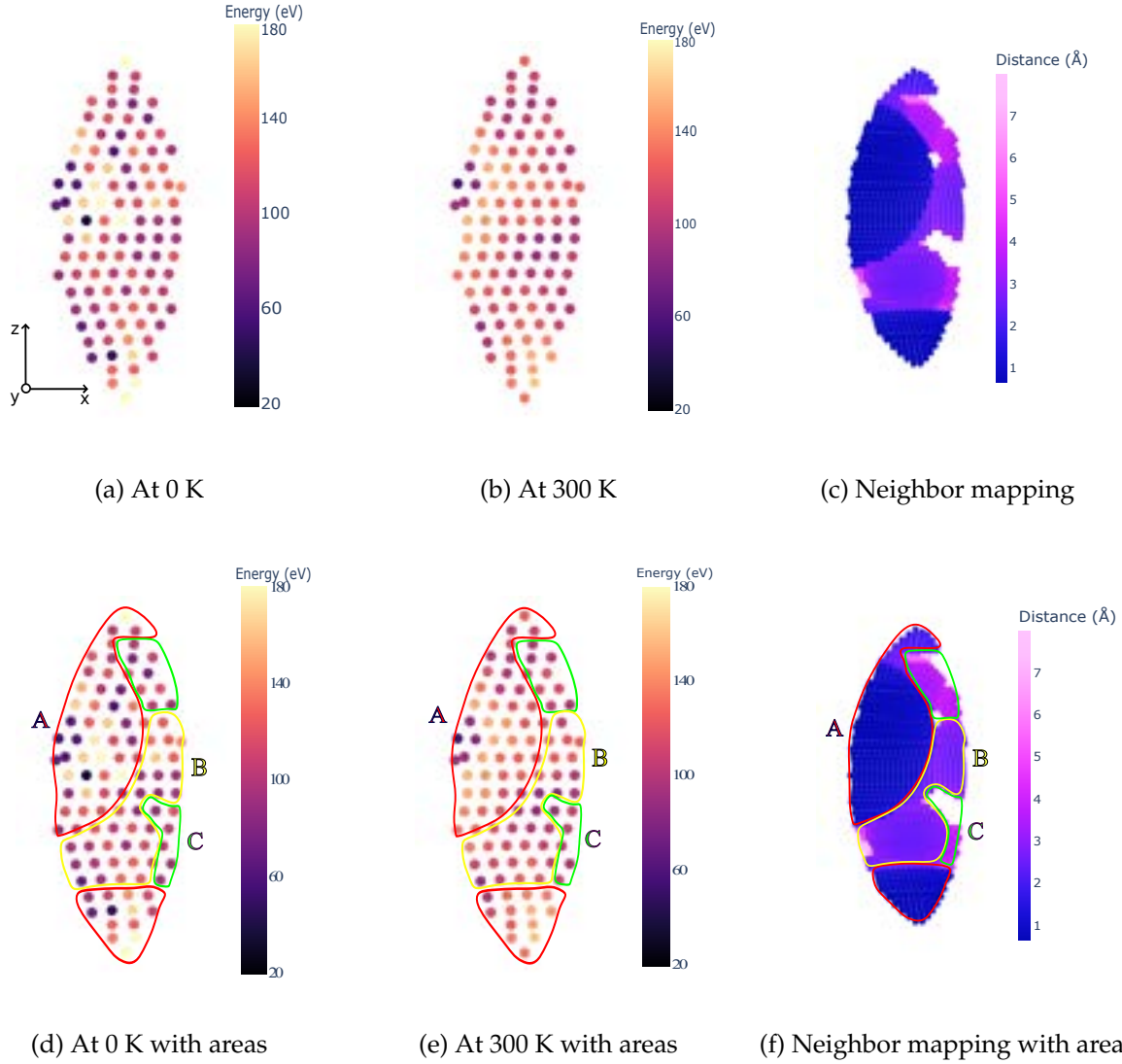


Figure 4.11: On the left and middle panels, spatial distribution of points representing directions based on their average TDE (color gradient) for N PKAs at different temperatures. A TDE of 20 eV is represented in black, while 180 eV and above are represented in yellow. Each point represents the average of 100 simulations. On the right, a spatial distribution of points shows the distance to the nearest neighbor in the associated direction, also referred to as a neighbor mapping for N PKAs based on their distances. The origin of the directions is the N PKA. Below each figure, the same plot is shown with dense zones labeled A, B, and C to aid explanation. These zones are defined based on the neighboring atom map. Zone A (red): "Dense" regions where neighboring atoms are very close. Zone B (yellow): "Moderately dense" regions, where neighboring atoms are at a moderate distance ($< 3.5 \text{ \AA}$) and some void space is present. Zone C (green): "Sparsely dense" regions with significant void space, where neighboring atoms are at distances $> 4 \text{ \AA}$. The lighter the color, the greater the distance to neighboring atoms.

4.5.3 Temperature Effect on TDE in GaN

This subsection aims to highlight the differences in TDE values in one direction for Ga and N PKAs in GaN at temperatures of 0 K, 200 K, 300 K, and 500 K. A total of 1 000 simulations initiated with distinct atomic positions were conducted for each temperature. In my third year, I had the opportunity to co-supervise a postgraduate student who worked on collision cascades and the study of TDE in GaAs. To enrich the discussion, some of his results are included in this section.

Figure 4.12 shows the histograms of TDE values for one direction of Ga PKAs in GaN at temperatures of 0 K, 200 K, 300 K, and 500 K. At 0 K we obtained a very precise distribution, with only 6 TDE values showing peaks of varying sizes. A majority of the distribution of TDE values is nevertheless located in a peak at 36 eV. At all four temperatures, a peak is observed around 35 eV. As the temperature increases, a second peak emerges and grows near 46 eV. At 0 K, a prominent peak is visible at approximately 36 eV, along with five smaller peaks between 35 eV and 50 eV. At 200 K, broadening around the 36 eV peak is observed, and a second significant peak grows at 46 eV. Additionally, TDE values around 90 eV are detected, which also appear at 300 K and 500 K. At 300 K and 500 K, the peaks at 36 eV and 46 eV remain present, but their intensity decreases, and the distribution becomes broader. With increasing temperature, the distribution of higher peaks diminishes, while the distribution for other values becomes more pronounced.

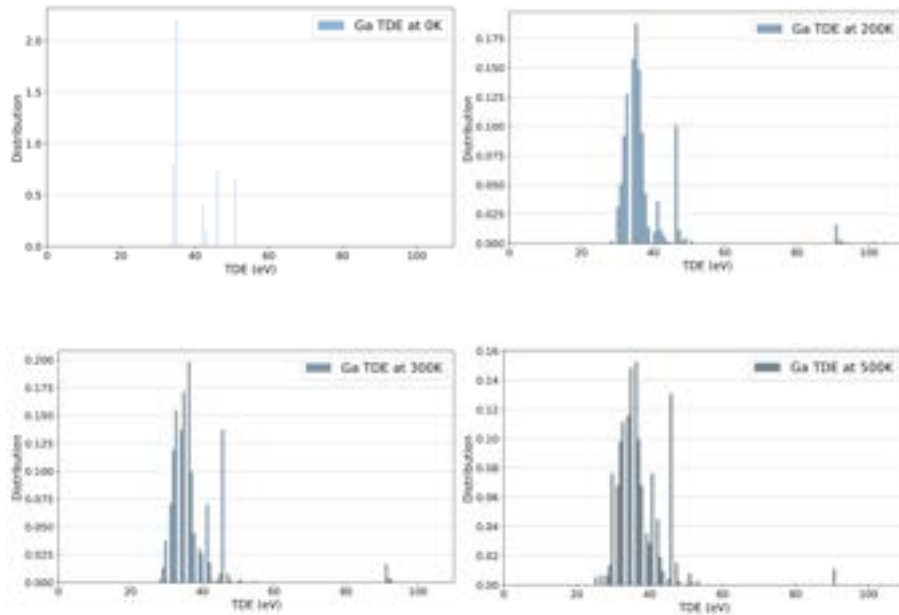


Figure 4.12: Histogram of TDE values of one direction for Ga PKAs in GaN at temperatures of 0 (top left) K, 200 K (top right), 300 K (bottom left), and 500 K (bottom right). For each temperature, 1,000 simulations are performed along a single direction.

Figure 4.13 illustrates the histograms of TDE values for one direction of N PKAs in

4.5. Large-Scale study of TDE in GaN

GaN at temperatures of 0 K, 200 K, 300 K, and 500 K. At 0 K, a prominent peak appears around 76 eV, accompanied by two much smaller peaks. At 200 K, the TDE values spread across a wider range, from 50 eV to 160 eV. A major peak emerges near 90 eV, followed by another significant one at approximately 150 eV. At 300 K, both peaks remain visible, with the addition of TDE values reaching 200 eV. By 500 K, the overall trends persist, but a higher number of TDE values are observed around 90 eV.

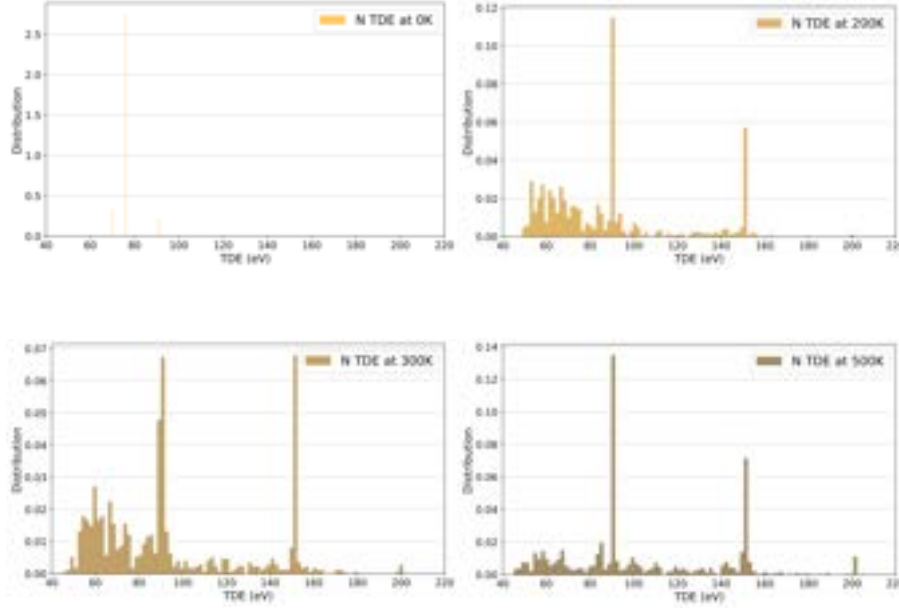


Figure 4.13: Histogram of TDE values of one direction for N PKAs in GaN at temperatures of 0 K (top left), 200 K (top right), 300 K (bottom left), and 500 K (bottom right). For each temperature, 1,000 simulations are performed along a single direction.

Figure 4.14 is the histogram of TDE values in four directions for Ga (blue) and As (red) PKAs in GaAs at various temperatures shows that TDE values in GaAs (3–35 for Ga and As PKAs) are much lower than in GaN (30–50 for Ga PKAs and 40–160 for N PKAs). In GaAs, TDE values at 0 K often align with the mean TDE values at higher temperatures. This is evidenced by a sharp peak at 0 K, whereas at higher temperatures, the peak broadens, indicating greater variability. In contrast, in GaN, TDE values do not show this behavior. Moreover, in the studied directions, GaAs never exhibited distributions with multiple peaks similar to those observed in GaN for the analyzed direction. The TDE distribution in GaN deviates from a Gaussian shape, suggesting the need for further exploration in more directions or simulations for GaAs.

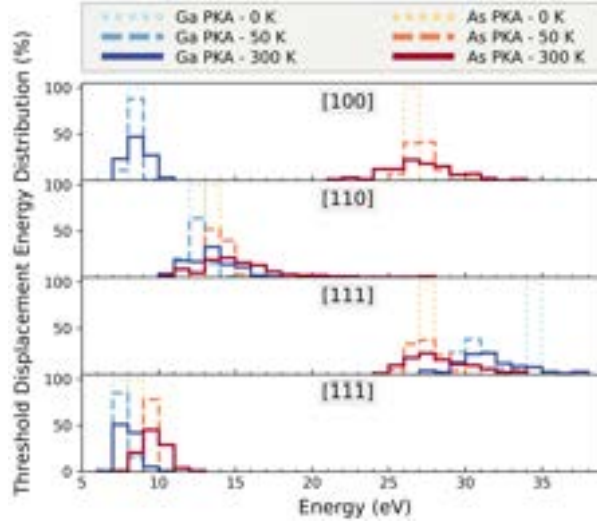


Figure 4.14: Histogram of TDE values for four directions, comparing Ga PKAs (blue) and As PKAs (red) in GaAs at various temperatures, provides valuable insights. Each bar represents a range of values, where the right-hand value corresponds to a displacement, while the left-hand value does not. These results are extracted from the final report by Khelladi Lilian.

4.6 Discussion

An important factor in understanding TDE is the PKA's environment in GaN's complex crystallographic structure. As explained in Section 4.3, the two types of atoms in GaN have vastly different properties that generate different implications for atomic displacement mechanisms. A Ga atom is five times heavier and twice larger than N atom, which imposes different constraints on the PKAs. This is illustrated in Figures 4.10c and 4.11c, showing neighboring atom maps. Large obstruction zones surround N PKAs due to the size of neighboring Ga atoms. As a result, N PKAs experience spatial confinement within Ga atom "cages". This confinement likely contributes to the high TDE values observed for N PKAs. If an N atom manages to escape the Ga cage, it struggles to return to its equilibrium site. Consequently, escape mechanisms of primary defects created by N PKAs result in N vacancies and N-N dumbbells due to limited displacements.

Generally, as temperature increases, thermal vibrations progressively broaden TDE value distributions. Higher temperatures lead to greater thermal vibrations, leading to an increase of atomic deviation from their equilibrium positions. This enhances atoms to leave their sites, increases random displacement trajectories reducing precise linear collision predictability, and favors defect creation.

At 0 K, a focusing phenomenon is observed for both Ga and N PKAs, but only at very high energies. At 0 K, precise linear collisions emerge where PKAs generate chain displacement events: atoms occupy perfect lattice positions, enabling collisions to occur in a precise linear fashion. The PKA strikes a neighboring atom, which then impacts its

own neighbor in the same direction, and so on. However, insufficient energy causes atoms to return to equilibrium, rendering defect creation extremely challenging. This effect is particularly pronounced in specific directions, such as Dir3 (x:0, y:0, z:-1) and Dir4 (x:0, y:0, z:1). At slightly higher temperatures, the perfect collision path is disrupted, PKAs follow imperfect and random trajectories, increasing the probability of deviation. However, if the direction remains obstructed, it can still be challenging for a PKA to leave its equilibrium site. For example, an N PKA moving toward a neighboring Ga atom may be deflected. If the deflection directs the PKA toward an unobstructed region, it has a higher chance of creating a defect compared to being deflected toward another obstructed zone, typically containing another Ga atom. These random processes explain why TDE spans a wide range of values and cannot be summarized by a single value, even for a specific direction. Regarding the differences in TDE values between GaN and GaAs, several avenues can be explored, such as examining additional directions in both materials under identical temperature conditions.

4.7 Conclusion

In this final chapter, we conducted a study of the Threshold Displacement Energy (TDE), defined as the minimum energy required to permanently displace an atom from its lattice site, using two simulation methods: *Ab initio* Molecular Dynamics (AIMD) and classical Molecular Dynamics (MD). After reviewing the existing literature on TDE studies in GaN, we presented results obtained through AIMD and MD for five crystallographic directions at 0 K and 300 K, including the configurations of the resulting defects. Subsequently, we performed a large-scale MD study across approximately 100 directions, analyzing raw TDE data, considering the influence of neighboring atoms on directional TDE values, and investigating the effect of temperature at various levels.

This comprehensive investigation of TDE in GaN represents a sophisticated exploration of atomic displacement mechanisms using advanced simulation methodologies. Several key findings emerge from this study. The most significant observation is the wide variability in TDE values for the same type of PKA. The dominant created defects are N vacancies and N dumbbells. TDE values are consistently higher for N PKAs compared to Ga PKAs. We deduce fundamental displacement principles. Neighboring atom configurations and environment critically determine TDE values: directional alignment with close neighboring atoms increases displacement thresholds higher than in directions pointing toward distant neighbors or voids. Finally, temperature progressively broadens displacement energy distributions.

The research not only quantifies threshold displacement energies but illuminates the intricate probabilistic mechanisms governing atomic displacement in GaN structures.

Bibliography

- [1] M Nastasi. *Ion-solid Interactions: Fundamentals and Applications*. Cambridge University Press, 1996.
- [2] HH Andersen. The depth resolution of sputter profiling. *Applied physics*, 18:131–140, 1979.
- [3] Peter Vajda. Anisotropy of electron radiation damage in metal crystals. *Reviews of Modern Physics*, 49(3):481, 1977.
- [4] K. Nordlund, J. Wallenius, and L. Malerba. Molecular dynamics simulations of threshold displacement energies in fe. *Nuclear Instruments and Methods in Physics Research Section B: Beam Interactions with Materials and Atoms*, 246(2):322–332, 2006. ISSN 0168-583X. doi: <https://doi.org/10.1016/j.nimb.2006.01.003>. URL <https://www.sciencedirect.com/science/article/pii/S0168583X06000243>.
- [5] Marc Robinson, NA Marks, and GR Lumpkin. Sensitivity of the threshold displacement energy to temperature and time. *Physical Review B—Condensed Matter and Materials Physics*, 86(13):134105, 2012.
- [6] Marc Robinson, NA Marks, KR Whittle, and GR Lumpkin. Systematic calculation of threshold displacement energies: Case study in rutile. *Physical Review B—Condensed Matter and Materials Physics*, 85(10):104105, 2012.
- [7] Pär Olsson, CS Becquart, and C Domain. Ab initio threshold displacement energies in iron. *Materials Research Letters*, 4(4):219–225, 2016.
- [8] LA Miller, DK Brice, AK Prinja, and ST Picraux. Displacement-threshold energies in si calculated by molecular dynamics. *Physical Review B*, 49(24):16953, 1994.
- [9] J.M Perlado, L Malerba, A Sánchez-Rubio, and T Diaz de la Rubia. Analysis of displacement cascades and threshold displacement energies in -sic. *Journal of Nuclear Materials*, 276(1):235–242, 2000. ISSN 0022-3115. doi: [https://doi.org/10.1016/S0022-3115\(99\)00183-X](https://doi.org/10.1016/S0022-3115(99)00183-X). URL <https://www.sciencedirect.com/science/article/pii/S002231159900183X>.
- [10] G Lucas and L Pizzagalli. Comparison of threshold displacement energies in β -sic determined by classical potentials and ab initio calculations. *Nuclear Instruments and Methods in Physics Research Section B: Beam Interactions with Materials and Atoms*, 229(3-4):359–366, 2005.
- [11] Nanjun Chen, Sean Gray, Efrain Hernandez-Rivera, Danhong Huang, Paul D LeVan, and Fei Gao. Computational simulation of threshold displacement energies of gaas. *Journal of Materials Research*, 32(8):1555–1562, 2017.
- [12] HY Xiao, Fei Gao, Xiaotao T Zu, and William J Weber. Threshold displacement energy in gan: Ab initio molecular dynamics study. *Journal of Applied Physics*, 105(12), 2009.

- [13] Alexander S Hauck, Miaomiao Jin, and Blair R Tuttle. Atomic displacement threshold energies and defect generation in gan, aln, and algan: A high-throughput molecular dynamics investigation. *Applied Physics Letters*, 124(15), 2024.
- [14] Paolo Giannozzi, Stefano Baroni, Nicola Bonini, Matteo Calandra, Roberto Car, Carlo Cavazzoni, Davide Ceresoli, Guido L Chiarotti, Matteo Cococcioni, Ismaila Dabo, et al. Quantum espresso: a modular and open-source software project for quantum simulations of materials. *Journal of physics: Condensed matter*, 21(39):395502, 2009.
- [15] DR Hamann. Optimized norm-conserving vanderbilt pseudopotentials. *Physical Review B—Condensed Matter and Materials Physics*, 88(8):085117, 2013.
- [16] "A. P. Thompson, H. M. Aktulga, R. Berger, D. S. Bolintineanu, W. M. Brown, P. S. Crozier, P. J. in 't Veld, A. Kohlmeyer, S. G. Moore, T. D. Nguyen, R. Shan, M. J. Stevens, J. Tranchida, C. Trott, and S. J. Plimpton". "lammmps - a flexible simulation tool for particle-based materials modeling at the atomic, meso, and continuum scales". *Comp. Phys. Comm.*, 271:108171, 2022. doi: 10.1016/j.cpc.2021.108171.
- [17] J. F. Ziegler, M. D. Ziegler, and J. P. Biersack. SRIM - The stopping and range of ions in matter (2010). *Nucl. Instr. Meth. Phys. R. B*, 268:1818–1823, Jun 2010. doi: 10.1016/j.nimb.2010.02.091.
- [18] J Nord, K Nordlund, J Keinonen, and K Albe. Molecular dynamics study of defect formation in gan cascades. *Nuclear Instruments and Methods in Physics Research Section B: Beam Interactions with Materials and Atoms*, 202:93–99, 2003.
- [19] J Nord, K Albe, P Erhart, and KJJoPCM Nordlund. Modelling of compound semiconductors: analytical bond-order potential for gallium, nitrogen and gallium nitride. *Journal of Physics: Condensed Matter*, 15(32):5649, 2003.
- [20] Sandia Corporation. fix electron/stopping command, 2023. URL https://docs.lammps.org/fix_electron_stopping.html Accessed on: July 2023.
- [21] Coping with the stochasticity of collision cascades in molecular dynamics simulations. *Nuclear Instruments and Methods in Physics Research Section B: Beam Interactions with Materials and Atoms*, 500-501:1–9, 2021. ISSN 0168-583X. doi: <https://doi.org/10.1016/j.nimb.2021.02.015>. URL <https://www.sciencedirect.com/science/article/pii/S0168583X21001683>.
- [22] Alexander Stukowski. Visualization and analysis of atomistic simulation data with OVITO-the Open Visualization Tool. *MODELLING AND SIMULATION IN MATERIALS SCIENCE AND ENGINEERING*, 18(1), JAN 2010. ISSN 0965-0393. doi: {10.1088/0965-0393/18/1/015012}.
- [23] P. F. Zou and R. F. W. Bader. A topological definition of a Wigner–Seitz cell and the atomic scattering factor. *Acta Cris. A*, 50(6):714–725, Nov 1994. doi: 10.1107/S0108767394003740.

- [24] J Nord, K Nordlund, J Keinonen, and K Albe. Molecular dynamics study of defect formation in gas cascades. *Nuclear Instruments and Methods in Physics Research Section B: Beam Interactions with Materials and Atoms*, 202:93–99, 2003.

Concluding remarks and perspectives

The overarching aim of this thesis is to understand the radiation resistance of gallium nitride (GaN) to displacement damage (DD) using numerical simulation methods. This semiconductor, renowned for its exceptional properties in power and high-frequency applications, has been studied concerning its resistance to displacement damage (DD)—a recurring phenomenon resulting from interactions between radiation particles and materials. By employing simulation techniques such as molecular dynamics and *ab initio* molecular dynamics, we simulated collision cascades and evaluated the threshold displacement energy (TDE) of atoms in GaN.

We began by researching the state of the art regarding the characteristics of GaN, particularly its behavior under non-ionizing radiation. This lead us to investigate its response to collision cascades. Although a few existing studies had explored this topic, they often overlooked important details, such as N type primary knock-on atoms (PKAs), and typically involved a limited number of simulations, which is insufficient for obtaining statistically robust results.

We decide to conduct a comprehensive simulation study on the displacement damage effects in GaN, focusing on both Ga and N PKAs. For comparison, we include simulations of Si and Ge, two well-studied semiconductors. The simulation method chosen is molecular dynamics, which allows tracking atomic dynamics over time. This method provides insight into cascade morphology and enables the analysis of the entire sequence of events: the ballistic phase, where atoms are displaced; the heat spike phase, where the number of crystalline defects peaks; and the recrystallization phase, during which some of the defects are annealed. Collision cascades with energies of 1 keV, 10 keV, and 25 keV are initiated in GaN with Ga and N PKAs, in Si with Si PKAs, and in Ge with Ge PKAs. The observed behaviors varied significantly across materials and between the two PKA types in GaN. First, during the heat spike phase, the number of defects is much higher for heavier PKAs (Ga and Ge), while lighter PKAs (N and Si) travel significantly farther. This suggests that heavy PKAs create localized but highly dense defect regions, whereas light PKAs produce larger but less dense cascades. The temporal tracking reveal a significantly higher recrystallization rate in GaN compared to Si and Ge, particularly for Ga-induced cascades. In GaN, 93% of defects are annealed for Ga PKAs, and 83% for N PKAs, with most of the defects disappearing within picoseconds of the cascade. In contrast, the recrystallization rate for Si and Ge is only about 50%. Another key factor to consider is defect clustering within the material. Defects often aggregate into clusters, which can negatively impact the

electronic properties of the material. In GaN, following the recrystallization phase, large defect clusters are eliminated, unlike in Si and Ge. To understand why recrystallization is more pronounced in GaN, we analyze defect motion in the three materials. It was found that during the heat spike phase, displaced atoms in GaN typically traveled shorter distances compared to those in Si and Ge. As a result, defective atoms in GaN have an easier time returning to their equilibrium sites, facilitating recrystallization. This limited defect displacement is attributed to GaN's wurtzite structure, where neighboring atoms are closer together than in the diamond structures of Si and Ge.

To further explore the potential resistance of GaN to displacement damage, we focus on the TDE. This is a critical input parameter for particle-matter simulation codes, representing the minimum energy required to displace an atom and create a permanent defect. We use two methods to evaluate this energy in GaN: classical MD, which enables statistical studies, and *ab initio* molecular dynamics (AIMD), which is more precise but computationally intensive. A review of the literature reveals that very few studies consider the TDE for N atoms, and those that do often lack statistical rigor. Additionally, the TDE depends on the direction along which the atom is displaced, making it crucial to sample a wide range of directions, an aspect often neglected in prior studies. Furthermore, because the energy values are low and displacements minimal, it is imperative to account for the effects of thermal vibrations, i.e., temperature, on the TDE. We evaluate the TDE in two stages: first, using AIMD for five specific directions in GaN due to computational constraints, and then using classical MD for 100 directions, with 100 different initial positions per direction to simulate thermal vibrations. These studies are conducted at various temperatures. The atoms selected for TDE evaluation are also referred to as PKAs.

For the initial five directions, we observe that TDE values for N PKAs are higher than for Ga PKAs. Two of these five directions pose challenges, particularly at 0 K, where atoms are in their ideal positions, and collisions occur perfectly between the PKA and a neighboring atom, leading to a "spring effect." In these directions, the required energy is significantly higher for both types of PKAs at all temperatures studied, with the effect being most pronounced at 0 K. Four types of defects can form: a Ga vacancy, a Ga interstitial, an N vacancy, or an N-N dumbbell (where two N atoms occupy an equilibrium site). Ga PKAs tend to produce all four defect types, although N vacancies and N-N dumbbells are the most common. In contrast, N PKAs only generate N vacancies and N-N dumbbells. This discrepancy can likely be attributed to the mass difference between the two atoms. The analysis of 100 directions further confirms the trend of higher TDEs for N PKAs. Only slight differences are observed between 0 K and 300 K for both types of PKAs. At 0 K, extreme TDE values are noted. Instead of a precise value, a range of TDE values emerges. To better understand the anisotropy of the TDE, we attempt to link specific directions and their TDE values to the local atomic environment. In general, obstructed zones exhibit higher TDE values compared to less obstructed zones (where neighboring atoms are more than 4 Å away) or non-obstructed zones. Finally, we study the effect of temperature on a single direction. We observe that increasing temperature tends to broaden the distribution of TDE values for both types of PKAs. These varied behaviors can be explained by the differences in the properties of the two atoms composing GaN. A nitrogen atom, being five

times lighter than a gallium atom, struggles to displace a Ga atom. It becomes effectively "trapped" in a kind of cage, where only very high energies allow it to break free. Once it escapes this cage, it is challenging for the N atom to return to its equilibrium site, making the formation of an N-N dumbbell more likely. Thermal vibrations facilitate this escape by slightly displacing atoms from their equilibrium positions, making deviations, particularly for N atoms, easier.

Following these extensive studies, the avenues for future exploration are equally promising. Revisiting the idea of using TDE ranges as input for particle-matter simulation software, implementing directional and temperature-dependent TDE ranges would be more accurate than relying on a single value. Developing a TDE database for studied materials could further enhance the rigor of simulations involving particle-matter interactions.

During our research, we encountered challenges related to computational time. The extensive MD simulations required to obtain statistically rigorous data are inherently time-consuming. However, the primary bottleneck lies in AIMD simulations, which are computationally intensive and demand significant resources. A potential solution could involve the development of a machine learning (ML)-based interatomic potential for GaN. The idea is to accurately simulate GaN's electronic properties using *ab initio* and then train an ML model to create an interatomic potential for use in classical MD simulations. This approach could provide DFT-level accuracy in faster MD simulations. Although ML-based interatomic potentials often increase computational time compared to conventional MD, the overhead is negligible compared to the prolonged durations required for AIMD simulations. Such an approach could also be extended to other materials.

Other perspectives can be explored, such as investigating higher energies. It is worth questioning whether recrystallization at the end of collision cascades also occurs at higher energies. One might expect to observe complete amorphization, as it could become more challenging for atoms to recrystallize. For N PKAs, the cascade size was close to a nanometer at 25 keV. Will the size stop increasing at a certain PKA energy? Does the morphology of the cascade change as well? Unfortunately, computational constraints have prevented us from answering these questions. However, with advancements in computational power and storage capabilities, it may become feasible to explore those higher energies. Another interesting aspect would be the investigation of complex defects and their long-term evolution. Using DFT calculations, we could examine the electronic properties of radiation-induced defects and their diffusion mechanisms, providing insights into material degradation over extended periods. This approach would bridge the gap between our current picosecond-scale simulations and the operational lifetime of GaN devices. Additionally, studying the impact of dopants and impurities on radiation resistance is crucial for practical applications, as real devices rarely use pure GaN. The interaction between radiation-induced defects and intentional dopants could either enhance or compromise radiation hardness—a critical aspect that remains unexplored. Another promising direction is irradiation experiments on GaN components. Using transmission electron microscopy (TEM) imaging, it would be possible to observe the aftermath of GaN after irradiation, validating our simulation results.

From a materials perspective, expanding our investigation to GaN-based alloys such as AlGaIn and InGaIn could reveal strategies to further enhance radiation resistance through compositional engineering. In fact, AlGaIn/GaN HEMTs (High Electron Mobility Transistors) already show promising properties for various applications, and understanding their radiation response could open new avenues for radiation-hardened devices. This investigation would involve simulating collision cascades in AlGaIn using classical molecular dynamics (MD), followed by studying the threshold displacement energy (TDE). Ultimately, it would be crucial to evaluate the heterojunction of AlGaIn and GaN under radiation, shedding light on their combined behavior in such conditions. Moreover, a comparative study with other wide-bandgap semiconductors like SiC and diamond would provide valuable insights into the fundamental mechanisms of radiation resistance in these material classes. Of particular interest is the behavior of GaN/substrate interfaces under irradiation, as these regions often serve as nucleation sites for defects and could significantly impact device reliability. Such interfaces, whether with silicon, sapphire, or SiC substrates, merit detailed investigation as they represent potential weak points in real devices exposed to radiation.

Appendices

Maximum penetration depth

Figures A.1 and A.2 show the maximum penetration depth distribution of PKAs at 1 keV and 25 keV for Ga and N PKAs in GaN, Si PKAs in Si and Ge PKAs in Ge.

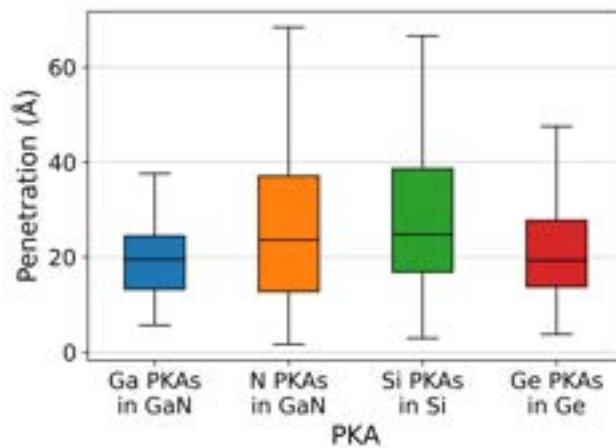


Figure A.1: Box plots of the maximum penetration depth of Ga PKAs in GaN (blue), N PKAs in GaN (orange) , Si PKAs in Si (green) and Ge PKAs in Ge (red) for 10 keV collision cascades. From lowest to highest, the horizontal lines of a box plot represents the minimum value of the set, the first quartile value, the median, the third quartile, and the maximum value of the set.

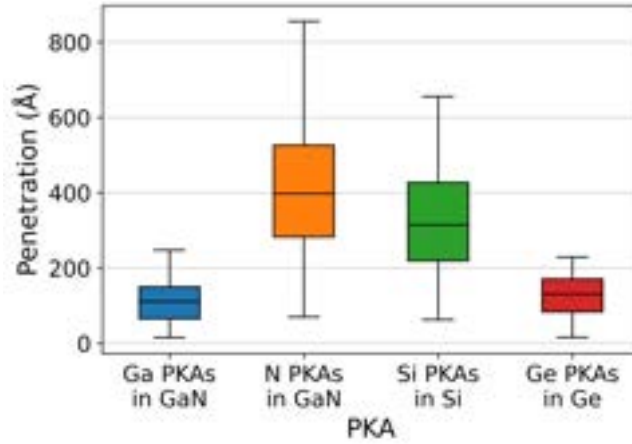


Figure A.2: Box plots of the maximum penetration depth of Ga PKAs in GaN (blue), N PKAs in GaN (orange), Si PKAs in Si (green) and Ge PKAs in Ge (red) for 10 keV collision cascades. From lowest to highest, the horizontal lines of a box plot represent the minimum value of the set, the first quartile value, the median, the third quartile, and the maximum value of the set.

Number of defects

Figures A.3 and A.4 show the distribution of the number of defects obtained at the end of simulations of 1 keV and 25 keV collision cascades initiated by Ga and N PKAs in GaN, Si PKAs in Si and Ge PKAs in Ge. Large differences between the three materials can be also observed here.

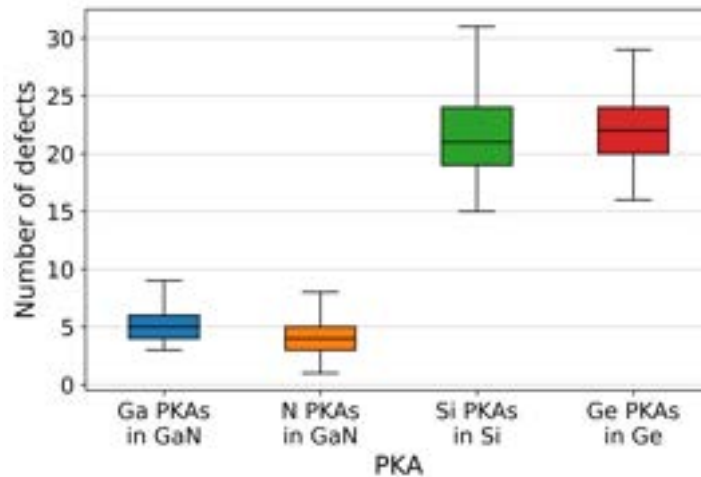


Figure A.3: Box plots of the number of defects after 1 keV collision cascades initiated by Ga PKAs in GAN (blue), N PKAs in GaN (orange), Si PKAs in Si (in green) and Ge PKAs in Ge (in red). From lowest to highest, the horizontal lines of a box plot represent the minimum value of the set, the first quartile value, the median, the third quartile, and the maximum value of the set.

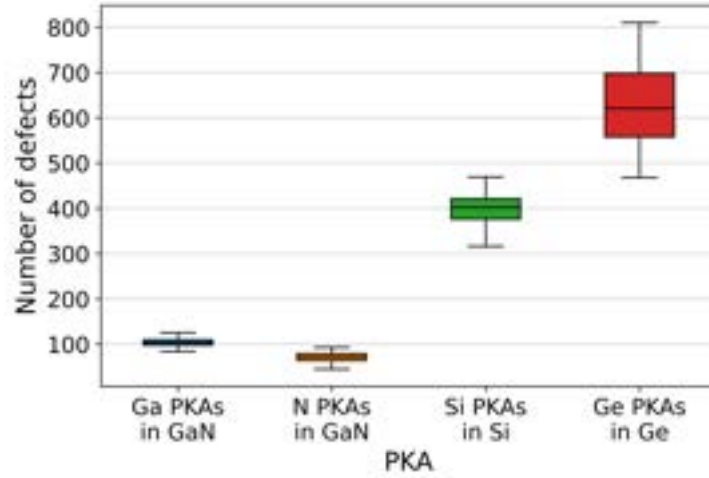


Figure A.4: Box plots of the number of defects after 25 keV collision cascades initiated by Ga PKAs in GaN (blue), N PKAs in GaN (orange), Si PKAs in Si (in green) and Ge PKAs in Ge (in red). From lowest to highest, the horizontal lines of a box plot represent the minimum value of the set, the first quartile value, the median, the third quartile, and the maximum value of the set. One hundred simulations are run for each type of PKA.

Defect number evolution profile

Figures A.5 and A.6 show the distribution of the number of clusters as a function of their size (number of defects) at the peak of 1 keV and 25 keV collision cascades and at the end of same collision cascade simulations in GaN (PKAs Ga and N), Si and Ge.

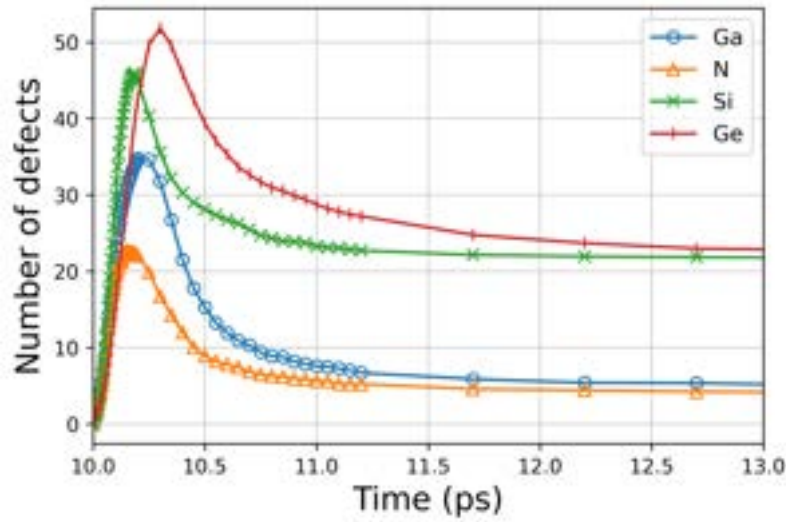


Figure A.5: Defect number evolution profiles during 22 ps for 1 keV collision cascades initiated by Ga PKAs in GaN (blue o), N PKAs in GaN (orange Δ), Si PKAs in Si (green x) and Ge PKAs in Ge (red |). Defect data are derived from averaging results across 100 simulations for each respective case.

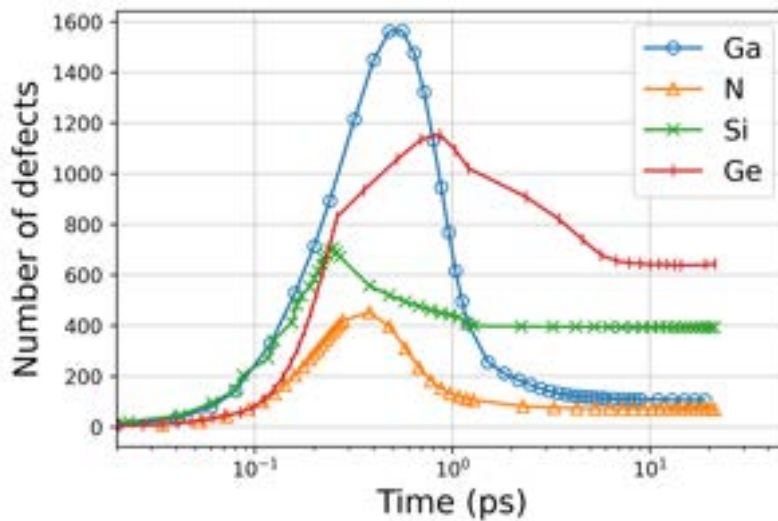


Figure A.6: Defect number evolution profiles during 30 ps for 25 keV collision cascades initiated by Ga PKAs in GaN (blue o), N PKAs in GaN (orange Δ), Si PKAs in Si (green x) and Ge PKAs in Ge (red |). Defect data are derived from averaging results across 100 simulations for Ga and Ge PKAs, 85 simulations for Si PKAs and 82 simulation for N PKAs.

Visual representation of defect clusters

Figures [A.7](#) and [A.8](#) exhibit a visual representation of defect clusters at the peak and at the end of a 1 keV and 25 keV collision cascade simulation, initiated by a Ga PKA in GaN, a N PKA in GaN, a Si PKA in Si and a Ge PKA in Ge. The selected cascades are representative of average cascades for each PKA. They have been chosen because their average penetration depth and average number of defects closely align with the data provided in Table I. Notably, all four cascades share the same direction.

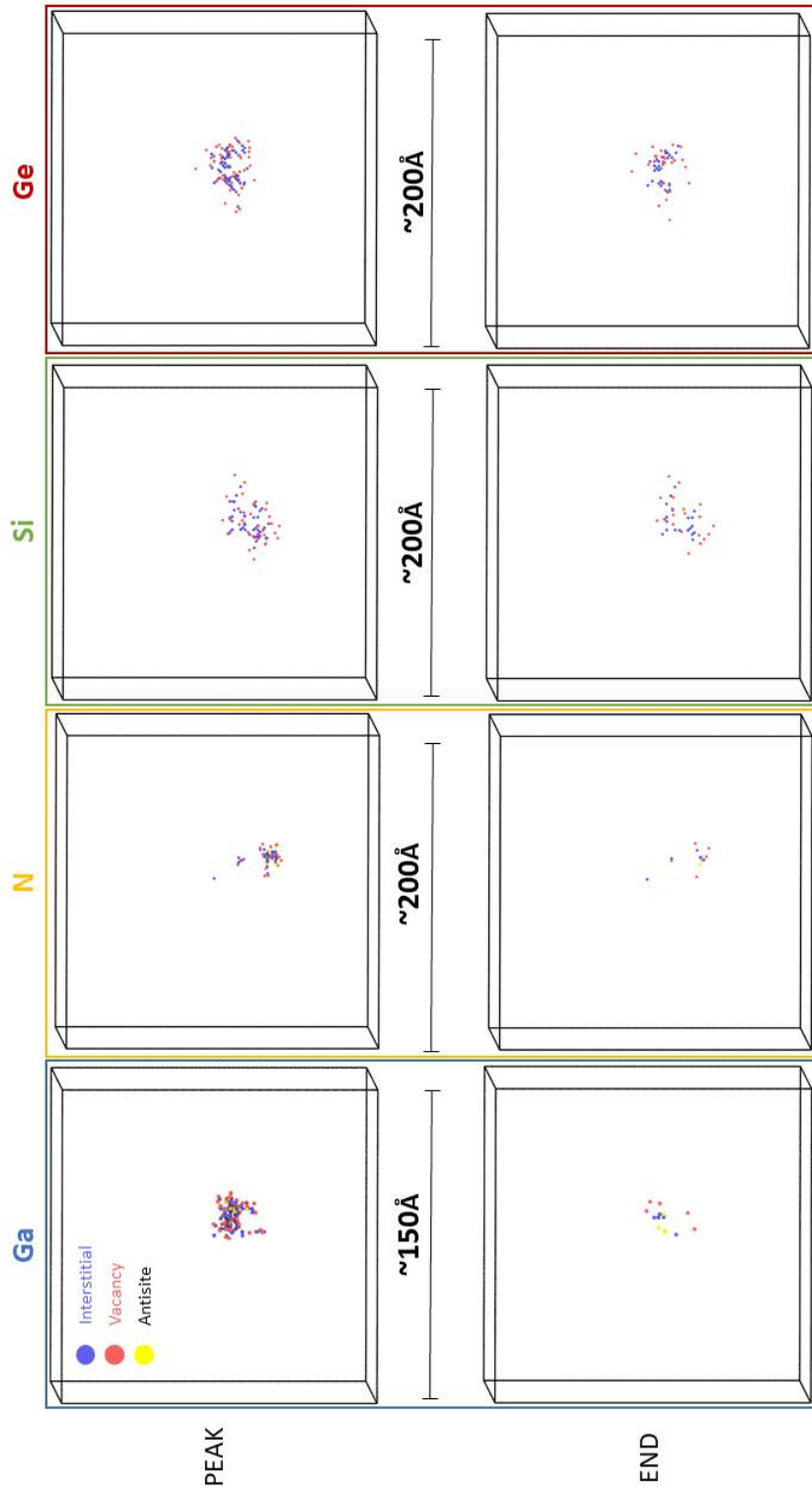


Figure A.7: Visual representation of defect clusters at the peak of a 1 keV collision cascade (top images) and at the end of the same 1 keV collision cascade simulation (bottom images) in GaN (PKAs Ga and N), Si and Ge. The blue spheres represent interstitial atoms, the red spheres represent vacancies and the yellow spheres represent antisites without specifying the type (Ga in an N site or N in a Ga site).

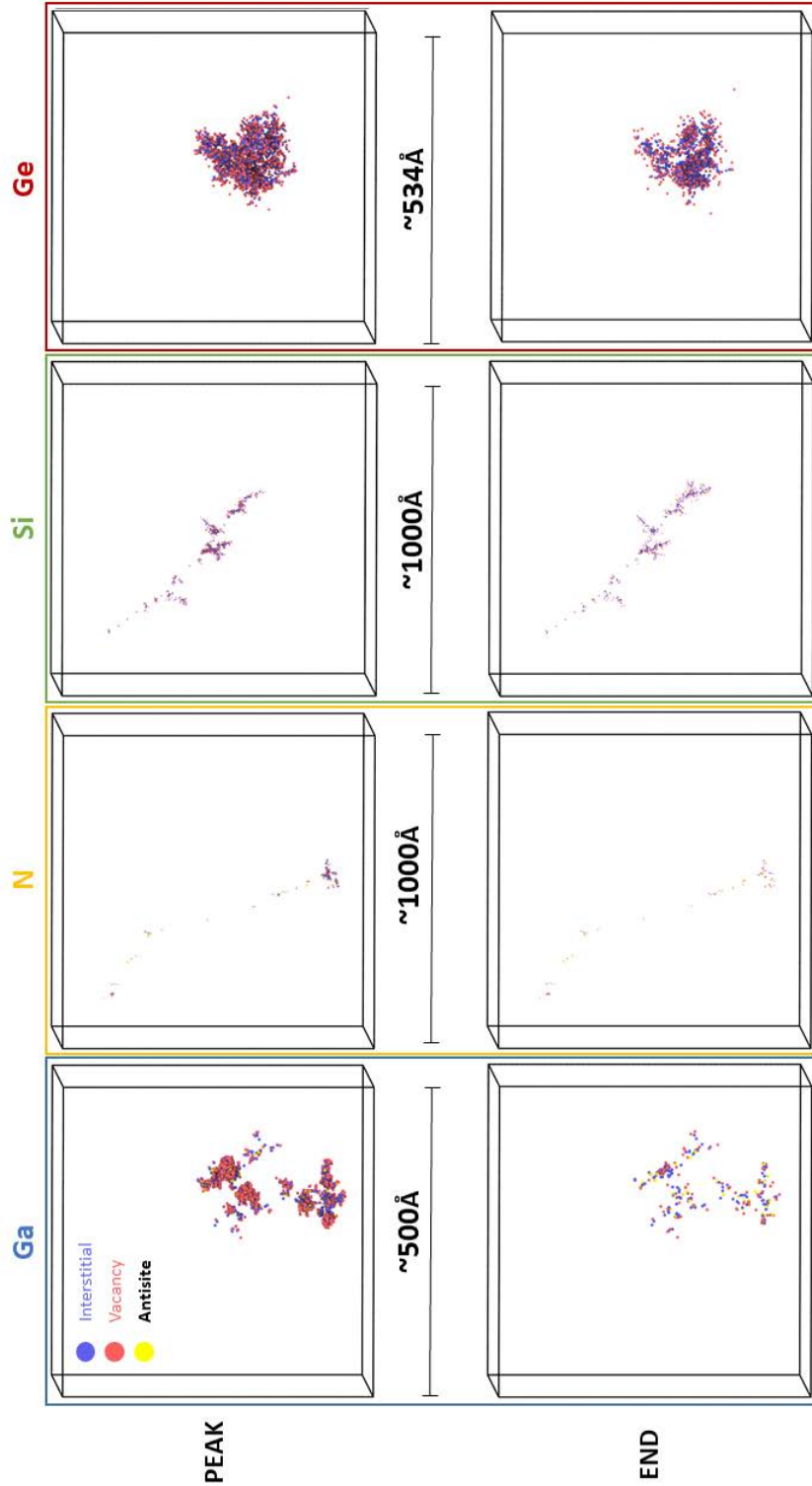


Figure A.8: Visual representation of defect clusters at the peak of a 25 keV collision cascade (top images) and at the end of the same 25 keV collision cascade simulation (bottom images) in GaN (PKAs Ga and N), Si and Ge. The blue spheres represent interstitial atoms, the red spheres represent vacancies and the yellow spheres represent antisites without specifying the type (Ga in an N site or N in a Ga site).

Distribution of the number of clusters as a function of their size

Figures A.9 and A.10 show the distribution of the number of clusters as a function of their size (number of defects) at the peak of 1 keV and 25 keV collision cascades and at the end of same collision cascade simulations in GaN (PKAs Ga and N), Si and Ge.

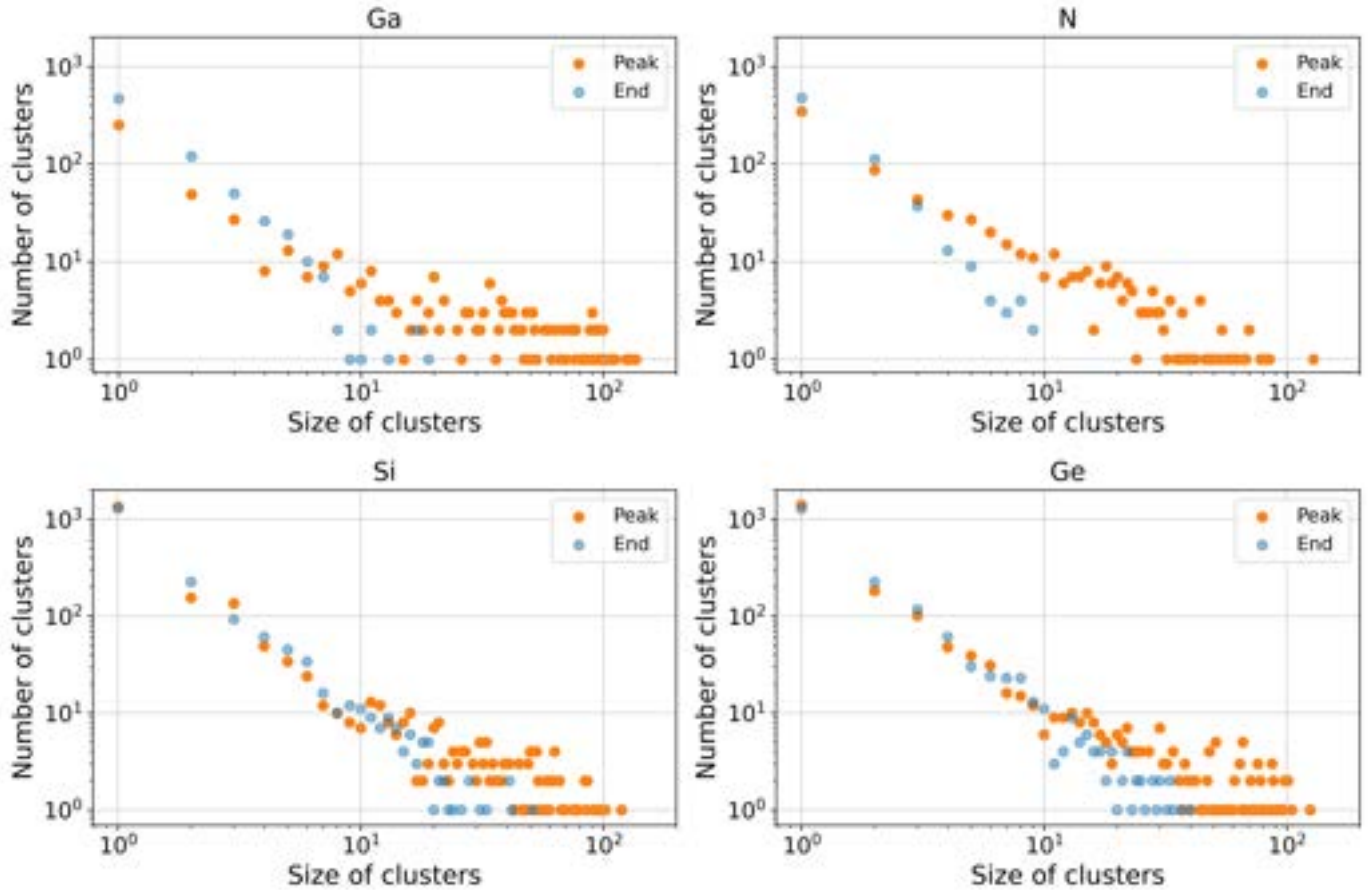


Figure A.9: Distribution of the number of clusters as a function of their size at the peak of the 1 keV collision cascade (orange dots) and at the end of the same collision cascade simulation (blue dots). Ga PKAs in GaN (top left), N PKAs in GaN (top right), Si PKAs in Si (bottom left) and Ge PKAs in Ge (bottom right). Data are obtained from 100 simulations in each case.

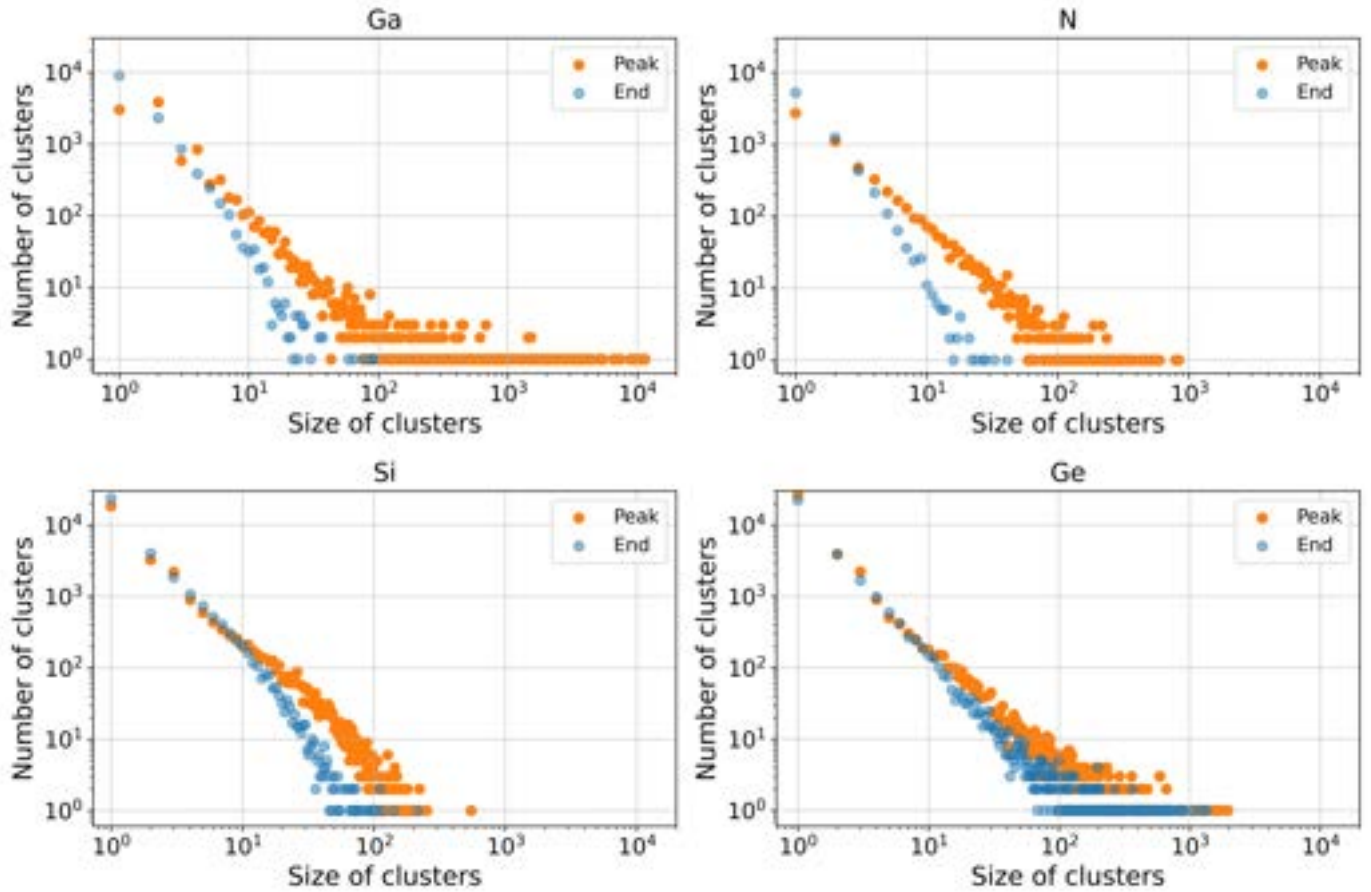


Figure A.10: Distribution of the number of clusters as a function of their size at the peak of the 25 keV collision cascade (orange dots) and at the end of the same collision cascade simulation (blue dots). Ga PKAs in GaN (top left), N PKAs in GaN (top right), Si PKAs in Si (bottom left) and Ge PKAs in Ge (bottom right). Data are obtained from 100 simulations in each case.

Distribution of interstitial displacement distances

Figures A.11 and A.12 display the distribution of the distance the interstitials identified at the peak of the cascade (1 keV and 25 keV) are displaced from their initial equilibrium position (called displacement), at the peak of the cascade and at the end of the simulation. Therefore, the displacements plotted at the end are not all coming from interstitial atoms as many of the atoms identified as interstitials at the peak of the cascade are back to their initial position at the end of the simulation.

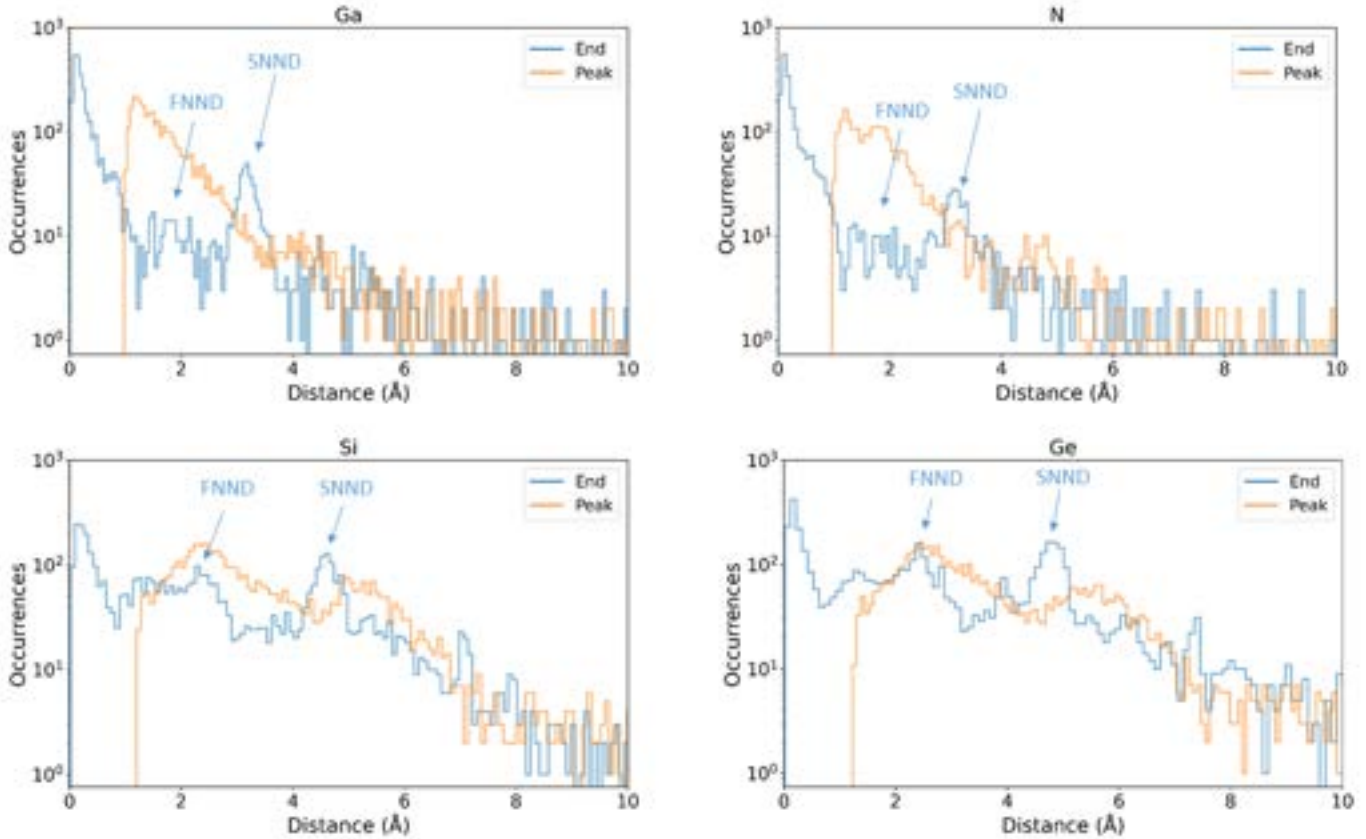


Figure A.11: Distributions of the distance the interstitials identified at the peak of the 1 keV cascades in GaN, Si and Ge are displaced from their initial equilibrium position (called displacement), at the peak of the cascades and at the end of the simulations. The first blue arrow represents the first nearest neighbour distance (FNND), the second represents the second nearest neighbour distance (SNND). Data are obtained from the average of 100 simulations in each case. At the peak of the cascades, the atoms selected to plot the displacements are all interstitials, whereas at the end, atoms identified as interstitials at the peak may have healed back to their initial position, and are thus not interstitials anymore.

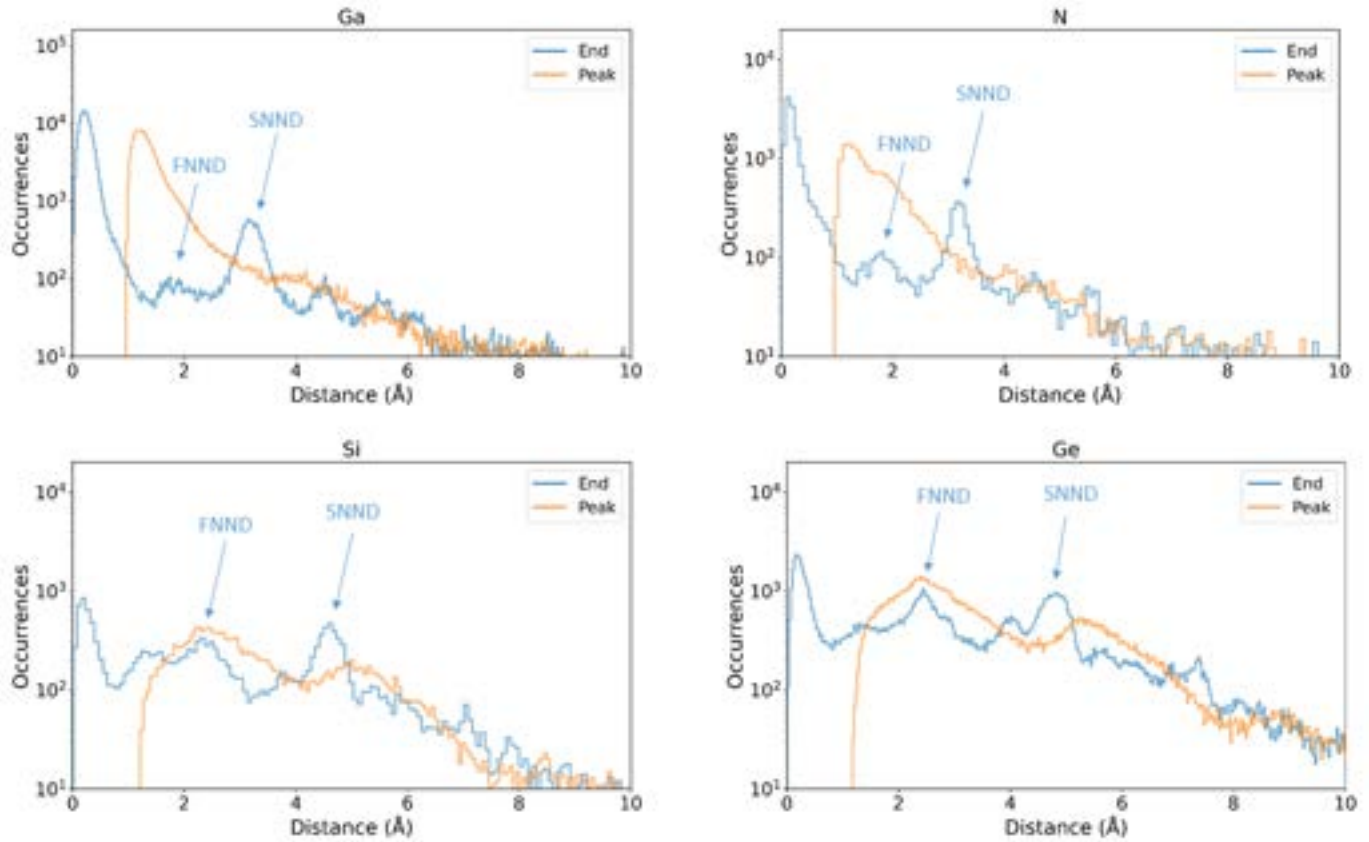


Figure A.12: Distributions of the distance the interstitials identified at the peak of the 25 keV cascades in GaN, Si and Ge are displaced from their initial equilibrium position (called displacement), at the peak of the cascades and at the end of the simulations. The first blue arrow represents the first nearest neighbour distance (FNND), the second represents the second nearest neighbour distance (SNND). Data are obtained from the average of 100 simulations in each case. At the peak of the cascades, the atoms selected to plot the displacements are all interstitials, whereas at the end, atoms identified as interstitials at the peak may have healed back to their initial position, and are thus not interstitials anymore.